ENSO SEASONAL SYNCHRONIZATION THEORY

A DISSERTATION SUBMITTED TO THE GRADUATE DIVISION OF
THE UNIVERSITY OF HAWAIʻI AT MĀNOA
IN PARTIAL FULFILLMENT OF THE REQUIREMENTS FOR THE
DEGREE OF

DOCTOR OF PHILOSOPHY

IN

OCEANOGRAPHY

MAY 2013

By

Karl J. Stein

Dissertation Committee:

Niklas Schneider, Chairperson
Axel Timmermann
Shang-Ping Xie
Fei-Fei Jin
Bo Qiu

Acknowledgements

I would like to thank my advisor, Niklas Schneider, and my dissertation committee members, Axel Timmermann, Fei-Fei Jin, Shang-Ping Xie, and Bo Qiu, for their guidance and motivation, my family for their support, my friends for their company, and Elke for her patience. This research was supported by the Office of Science (BER), U.S. Department of Energy, Grants No. DE-FG02-04ER63862 and DE- FG02-07ER64469, and through the sponsorship of research at the International Pacific Research Center (IPRC) by the Japan Agency for Marine-Earth Science and Technology (JAMSTEC), by NASA through grant No. NNX07AG53G, and by NOAA through grant No. NA17RJ1230.

Abstract

One of the key characteristics of the El Niño-Southern Oscillation (ENSO) phenomenon is its synchronization to the annual cycle. Current theories offer two possible mechanisms to account for this synchronization: frequency locking of ENSO to periodic forcing by the annual cycle, or the effect of the seasonally varying background state of the equatorial Pacific on the coupled stability of the ocean-atmosphere system. Using a parametric recharge oscillator model of ENSO, we test which of these scenarios provides a better explanation for the observational characteristics of ENSO/annual cycle interactions.

Analytical solutions obtained from the neutral case of the model show that the annual modulation of the growth rate parameter results directly in ENSO's seasonal variance, amplitude modulation, and 2:1 phase synchronization of ENSO to the annual cycle. The analytical solutions are shown to be applicable to numerical runs of the model in the neutral case, as well as the long-term behavior of the damped model excited by stochastic noise. The synchronization characteristics of the stochastically forced model agree with the observations, and are shown to account for the variety of ENSO synchronization in state of the art coupled general circulation model simulations. Additionally, the idealized model predicts spectral peaks at "combination tones" between ENSO and the annual cycle that exist in both the observations and many coupled models.

These results are then compared with the predictions of the nonlinear frequency entrainment model for ENSO/annual cycle interactions. The oscillator model is extended to include periodic forcing by the annual cycle and a nonlinear saturation term, and the resulting system is shown to be equivalent to the periodically forced van der Pol oscillator. Results from experiments with the van der Pol oscillator demonstrate that the frequency locking scenario predicts the existence of a spectral peak at the biennial frequency corresponding to the observed 2:1 phase synchronization. Such a peak does not exist in the observed ENSO spectrum. Hence, we conclude that the seasonal modulation of the coupled stability of the equatorial Pacific ocean-atmosphere system is the mechanism responsible for the synchronization of ENSO events to the annual cycle.

Contents

Acknowledgements i

Abstract ii

List of Figures xiii

1 Introduction 1

2 Features of ENSO synchronization: Nino3.4 index 7

3 Features of ENSO synchronization: CEOF analysis 21

4 Analytical solutions of the parametric recharge oscillator 33

5 Numerical confirmation of the analytical solutions 43

6 ENSO synchronization through frequency locking 51

7 Discussion 63

8 Summary and Conclusions 69

A Supplementary figures 71

Bibliography 87

List of Figures

2.1 (Top) The time series of the Nino3.4 SSTA index (black) and the Hilbert transform of the index (gray dashed), calculated from the ERSST.v3b data set. (Bottom left) The monthly deviations of Nino3.4 SST from the time mean. (Bottom center) The monthly variance of the Nino3.4 SSTA index and the monthly amplitude of the analytical signal of the index. (Bottom right) A PDF of the $\delta\phi_{2,1}$ phase difference of ENSO with the annual cycle, indicating the strength of the phase synchronization of ENSO to the annual cycle. See text for the definitions of the analytical signal, amplitude, and phase. 14

2.2 The spectrum of the ERSST.v3b Nino3.4 SSTA index, as calculated using the Yule-Walker (thick line) and Welch (dots) spectral estimation methods. The 95% confidence intervals of the Welch spectrum are indicated. The spectrum of a first order autoregressive model fit to the Nino3.4 SSTA index is shown for comparison (thin line). The grey bars are located at the frequency of the primary ENSO peak, the biennial frequency, and $\omega_a \pm \omega_e$ combination tone frequencies. 15

2.3 The annual cycles of the Nino3.4 SST indices calculated from historical runs of CGCMs participating in CMIP5. Models are organized according to the strength of the seasonal modulation of ENSO variance. 16

2.4 The seasonal variance of the Nino3.4 SSTA indices calculated from historical runs of CGCMs participating in CMIP5. Models are organized according to the strength of the seasonal modulation of ENSO variance. . 17

2.5 PDFs of the $\delta\phi_{2,1}$ phase difference between the annual cycles and the Nino3.4 SSTA indices calculating from historical runs of CGCMs participating in CMIP5. Models are organized according to the strength of the seasonal modulation of ENSO variance. 18

2.6 Scatter plots of the amplitude modulation index (Ψ,top) and the phase synchronization index (χ, bottom) versus the seasonal variance index (ν) based on the observations and CGCMs participating in CMIP5. See text for the definitions of the synchronization indices. 19

2.7 The spectrum of the Nino3.4 SSTA index index anomalies of CMIP5 CGCM historical runs, as calculated using the Yule-Walker (thick grey) and Welch (thin black) spectral estimation methods. The 95% confidence intervals of the Welch spectrum are indicated (dashed). The spectrum of a first order autoregressive model fit to the Nino3.4 SSTA index is shown for comparison (thin line). The grey bars are located at the frequency of the primary ENSO peak, the biennial frequency, and the $\omega_a \pm \omega_e$ combination tone frequencies. 20

3.1 The magnitudes $(\mathbf{q}_1, \alpha_1(t))$ and phases $(\mathbf{r}_1, \phi_1(t))$ associated with the first mode obtained from a CEOF analysis of ERSST.v3b data. The contour plots show the spatial maps of $\mathbf{q}_1, \mathbf{r}_1$, with contour intervals indicated on the top right. The corresponding time series $\alpha_1(t)$ (blue line, left ordinate) and $\phi_1(t)$ (green x's, right ordinate) are shown below. The first mode captures the annual cycle of the data set. 27

3.2 The magnitudes $(\mathbf{q}_2, \alpha_2(t))$ and phases $(\mathbf{r}_2, \phi_2(t))$ associated with the second mode obtained from a CEOF analysis of ERSST.v3b data. The contour plots show the spatial maps of $\mathbf{q}_2, \mathbf{r}_2$, with contour intervals indicated on the top right. The corresponding time series $\alpha_2(t)$ (blue line, left ordinate) and $\phi_2(t)$ (green x's, right ordinate) are shown below. The second mode captures the dominant ENSO mode in the data set. 28

3.3 (Top) The time series of the real part of the ERSST.v3b CEOF PC2 time series (Re[$p_2(t)$],black) and the Nino3.4 SSTA index (gray dashed), calculated from the ERSST.v3b data set. (Bottom left) The monthly variance (σ_m) of the real part of the PC2 time series and the monthly amplitude (α_m) of the complex PC2 time series. (Bottom right) A PDF of the $\delta\phi_{2,1}$ phase difference of ENSO (ϕ_2) with the annual cycle ϕ_1, indicating the strength of the phase synchronization of ENSO to the annual cycle. See text for the definitions of the analytical signal, amplitude, and phase. . . . 29

3.4 The spectrum of the real part of the ERSST.v3b CEOF PC2 time series, as calculated using the Yule-Walker (thick line) and Welch (dots) spectral estimation methods. The 95% confidence intervals of the Welch spectrum are indicated. The spectrum of a first order autoregressive model fit to the real part of PC2 is shown for comparison (thin line). The grey bars are located at the frequency of the primary ENSO peak, the biennial frequency, and $\omega_a \pm \omega_e$ combination tone frequencies. 30

3.5 The spectrum of the real part of the ERSST.v3b CEOF PC2 time series with monthly means removed, as calculated using the Yule-Walker (thick line) and Welch (dots) spectral estimation methods. The 95% confidence intervals of the Welch spectrum are indicated. The spectrum of a first order autoregressive model fit to the real part of PC2 is shown for comparison (thin line). The grey bars are located at the frequency of the primary ENSO peak, the biennial frequency, and $\omega_a \pm \omega_e$ combination tone frequencies. 31

3.6 Scatter plots of the amplitude modulation index (Ψ,top) and the phase synchronization index (χ, bottom) versus the seasonal variance index (ν) based on the CEOF decomposition of equatorial Pacific SST observations, reanalyses, and model output from CGCMs participating in CMIP5. See text for the definitions of the synchronization indices. 32

4.1 (Top) The growth rate of ENSO in OFES, estimated from a stastical fit of equation (4.1) (dash-dot), and from a statistical-dynamical fit (dashed) based on the Bjerknes index (Jin et al., 2006). (Bottom) The seasonal variance of eastern Pacific upper ocean temperature (T) in OFES (solid) compared to model runs of (4.1,4.2) utilizing the growth rate $\lambda(t)$ determined from a statistical (dash-dot) and a statistical-dynamical (dash) fit. Figure reproduced from Stein et al. (2010). 41

4.2 (Top) The T time series and the Hilbert transform of the time series, based on the analytical solution of the neutral PRO model (equation 4.5). (Bottom left) The monthly variance of the T time series and the monthly amplitude of the analytical signal of the time series. (Bottom right) A PDF of the $\delta\phi_{2,1}$ phase difference of ENSO with the annual cycle. The analytical solutions of the seasonal variance, seasonal amplitude, and phase difference are indicated by dashed lines. 42

5.1 (Top) The T time series and the Hilbert transform of the time series, based on a numerical integration of the a neutral PRO model. (Bottom left) The monthly variance of the T time series and the monthly amplitude of the analytical signal of the time series. (Bottom right) A PDF of the $\delta\phi_{2,1}$ phase difference of ENSO with the annual cycle. The analytical solutions of the seasonal variance, seasonal amplitude, and phase difference are indicated by dashed lines. 47

5.2 (Top) An example of the T time series and the Hilbert transform of the time series, from a single member of an ensemble of integrations of the a damped, stochastically forced PRO model. (Bottom left) The ensemble mean monthly variance of the T time series and the ensemble mean monthly amplitude of the analytical signal of the time series. (Bottom right) A PDF of the $\delta\phi_{2,1}$ phase difference of ENSO with the annual cycle. 90% confidence intervals for the seasonal variance, amplitude modulation, and PDF of the phase difference, based on the 100 member ensemble, are shown. The analytical solutions of the seasonal variance, seasonal amplitude, and phase difference are indicated by dashed lines. 48

5.3 Contours of the seasonal variance index (ν, top), the amplitude modulation index (Ψ, middle), and the phase synchronization index (χ, bottom) of the analytical solution of the PRO model (equation 4.5) within the model parameter space defined by the intrinsic ENSO period and the strength of the annual cycle modulation. See text for the definitions of the synchronization indices. 49

5.4 The strength of the 2:1 phase synchronization (χ) in the observations and CMIP5 coupled GCMs versus the amount predicted based on analytical solutions of the PRO model (figure 5.3). 50

6.1 Time series from numerical integrations of van der Pol oscillator (6.3) for various values of the forcing amplitude ($\widehat{\omega}\widehat{F}$) and nonlinear damping ($\widehat{\lambda}$). For all time series, the driving frequency of the oscillator was set to $\widehat{\omega} = 4.02$ and initialized at $T = 2, \frac{dT}{d\tau} = 0$. From top to bottom, the time series represent a limit cycle, a relaxation oscillator, a quasiperiodic oscillation, a frequency locked oscillation, and a chaotic oscillation. The bottom plot shows the divergence of a time series initialized at $T = 2.01, \frac{dT}{d\tau} = 0$ (dashed). At the right, Poincaré sections of each time series for values of the annual cycle phase $\phi_a = 2\pi N$. 56

6.2 Contours of the ratio of the T output frequency to the forcing frequency in the van der Pol oscillator for various values of the growth rate (λ) and neutral ENSO period(T_e). Multiple regions of frequency locking (Arnol'd tongues) are evident in the parameter space of the model, preferentially occurring at odd multiples of the driving frequency. The mean frequency of the output was measured as the mean gradient of the unwrapped phase time series. 57

6.3 The time series (top) and spectrum (bottom left) of a quasiperiodic oscillation obtained from a run of the van der Pol oscillator with parameter values $F = 1.2°C$, $\lambda = \frac{1}{2}°C$ year^{-1}, and $T_e = 2.76$ years. The strength of the phase synchronization of the T time series with the periodic forcing for various rational multiples of $k : l$ is shown in the bottom right. See text for the definition of the phase synchronization index. 58

6.4 The time series (top) and spectrum (bottom left) of a frequency locked oscillation obtained from a run of the van der Pol oscillator with parameter values $F = 1.2°C$, $\lambda = 2°C$ yr^{-1}, and $T_e = 2.76$ yrs. The strength of the phase synchronization of the T time series with the periodic forcing for various rational multiples of $k : l$ is shown in the bottom right. See text for the definition of the phase synchronization index. 59

6.5 The same as in Figure 6.4, but with the inclusion of Gaussian stochastic noise forcing in the model. 60

6.6 Indices measuring the strength of the observed $k : l$ phase synchronization ($\chi_{k,l}$) of ENSO to the annual cycle for values of $k, l \in [1, 10]$. See text for definition of the phase synchronization index. 61

6.7 Indices measuring the strength of the $k : l$ phase synchronization ($\chi_{k,l}$) of ENSO to the annual cycle for values of $k, l \in [1, 10]$, as simulated by CGCMs participating in CMIP5. See text for definition of the phase synchronization index. 62

7.1 (Top) An example of the T time series and the Hilbert transform of the time series, from a single member of an ensemble of integrations of the a first order autoregressive model of ENSO (7.3). (Bottom left) The ensemble mean monthly variance of the T time series and the ensemble mean monthly amplitude of the analytical signal of the time series. (Bottom right) A PDF of the $\delta\phi_{2,1}$ phase difference of ENSO with the annual cycle. 90% confidence intervals for the seasonal variance, amplitude modulation, and PDF of the phase difference, based on the 100 member ensemble, are shown. 67

A.1 Contours of the phase spatial pattern (r_n) of the first mode (annual cycle, top) and second mode (ENSO, bottom) of the CEOF decomposition of equatorial SST output from a historical run (1901-2000) of the Canadian Earth System Model. The shading indicates the value of the amplitude spatial pattern (q_n), where darker shading indicates larger amplitude. . . 72

A.2 Contours of the phase spatial pattern (r_n) of the first mode (annual cycle, top) and second mode (ENSO, bottom) of the CEOF decomposition of equatorial SST output from a historical run (1901-2000) of the Community Climate System Model. The shading indicates the value of the amplitude spatial pattern (q_n), where darker shading indicates larger amplitude. . . 73

A.3 Contours of the phase spatial pattern (r_n) of the first mode (annual cycle, top) and second mode (ENSO, bottom) of the CEOF decomposition of equatorial SST output from a historical run (1901-2000) of the National Centre for Meteorological Research Climate Model. The shading indicates the value of the amplitude spatial pattern (q_n), where darker shading indicates larger amplitude. 74

A.4 Contours of the phase spatial pattern (r_n) of the first mode (annual cycle, top) and second mode (ENSO, bottom) of the CEOF decomposition of equatorial SST output from a historical run (1901-2000) of the Commonwealth Scientific and Industrial Research Organisation Global Climate Model. The shading indicates the value of the amplitude spatial pattern (q_n), where darker shading indicates larger amplitude. 75
A.5 Contours of the phase spatial pattern (r_n) of the first mode (annual cycle, top) and second mode (ENSO, bottom) of the CEOF decomposition of equatorial SST output from a historical run (1901-2000) of the Flexible Global Ocean-Atmosphere-Land System Model. The shading indicates the value of the amplitude spatial pattern (q_n), where darker shading indicates larger amplitude. 76
A.6 Contours of the phase spatial pattern (r_n) of the first mode (annual cycle, top) and second mode (ENSO, bottom) of the CEOF decomposition of equatorial SST output from a historical run (1901-2000) of two configurations of the Geophysical Fluid Dynamics Laboratory Earth System Model. The shading indicates the value of the amplitude spatial pattern (q_n), where darker shading indicates larger amplitude. 77
A.7 Contours of the phase spatial pattern (r_n) of the first mode (annual cycle, top) and second mode (ENSO, bottom) of the CEOF decomposition of equatorial SST output from a historical run (1901-2000) of the NASA Goddard Institute for Space Studies Model E. The shading indicates the value of the amplitude spatial pattern (q_n), where darker shading indicates larger amplitude. 78
A.8 Contours of the phase spatial pattern (r_n) of the first mode (annual cycle, top) and second mode (ENSO, bottom) of the CEOF decomposition of equatorial SST output from a historical run (1901-2000) of the Met Office Hadley Centre Climate prediction Model. The shading indicates the value of the amplitude spatial pattern (q_n), where darker shading indicates larger amplitude. 79

A.9 Contours of the phase spatial pattern (r_n) of the first mode (annual cycle, top) and second mode (ENSO, bottom) of the CEOF decomposition of equatorial SST output from a historical run (1901-2000) of the Met Office Hadley Centre Global Environmental Model. The shading indicates the value of the amplitude spatial pattern (q_n), where darker shading indicates larger amplitude. 80

A.10 Contours of the phase spatial pattern (r_n) of the first mode (annual cycle, top) and second mode (ENSO, bottom) of the CEOF decomposition of equatorial SST output from a historical run (1901-2000) of the Institut Pierre Simon Laplace Climate Model. The shading indicates the value of the amplitude spatial pattern (q_n), where darker shading indicates larger amplitude. 81

A.11 Contours of the phase spatial pattern (r_n) of the first mode (annual cycle, top) and second mode (ENSO, bottom) of the CEOF decomposition of equatorial SST output from a historical run (1901-2000) of the Institut Pierre Simon Laplace Climate Model. The shading indicates the value of the amplitude spatial pattern (q_n), where darker shading indicates larger amplitude. 82

A.12 Contours of the phase spatial pattern (r_n) of the first mode (annual cycle, top) and second mode (ENSO, bottom) of the CEOF decomposition of equatorial SST output from a historical run (1901-2000) of two configurations of the The Japan Agency for Marine-Earth Science and Technology Earth System Model. The shading indicates the value of the amplitude spatial pattern (q_n), where darker shading indicates larger amplitude. . . 83

A.13 Contours of the phase spatial pattern (r_n) of the first mode (annual cycle, top) and second mode (ENSO, bottom) of the CEOF decomposition of equatorial SST output from a historical run (1901-2000) of two configurations of the The Japan Agency for Marine-Earth Science and Technology Model for Interdisciplinary Research On Climate. The shading indicates the value of the amplitude spatial pattern (q_n), where darker shading indicates larger amplitude. 84

A.14 Contours of the phase spatial pattern (r_n) of the first mode (annual cycle, top) and second mode (ENSO, bottom) of the CEOF decomposition of equatorial SST output from a historical run (1901-2000) of the Meteorological Research Institute Coupled Global Climate Model. The shading indicates the value of the amplitude spatial pattern (q_n), where darker shading indicates larger amplitude. 85

A.15 Contours of the phase spatial pattern (r_n) of the first mode (annual cycle, top) and second mode (ENSO, bottom) of the CEOF decomposition of equatorial SST output from a historical run (1901-2000) of two configurations of the Norwegian Earth System Model. The shading indicates the value of the amplitude spatial pattern (q_n), where darker shading indicates larger amplitude. 86

Chapter 1

Introduction

The El Niño-Southern Oscillation (ENSO) is the largest global climate signal on interannual timescales (Neelin et al., 1998); strong ENSO events cause changes in the tropical Pacific climate that are large enough to influence the global atmospheric circulation (Trenberth et al., 1998), leading to significant environmental and socioeconomic impacts that occur in areas throughout the world (McPhaden et al., 2006). ENSO events occur irregularly, with 2-7 year spans between them, but they each follow a similar pattern of developing during boreal summer and peaking during boreal winter (Rasmusson and Carpenter, 1982; Larkin and Harrison, 2002). Such seasonal synchronization is a defining characteristic of ENSO, and understanding the cause is of central importance to ENSO predictions (Balmaseda et al., 1995; Torrence and Webster, 1998). The exact mechanism responsible for the synchronization of ENSO to the annual cycle has not yet been determined, though current ENSO theory offers two possible candidates: frequency locking of ENSO to periodic forcing by the annual cycle (Jin et al., 1994; Tziperman et al., 1994), or the modulation of ENSO's coupled stability due to the seasonal variation of the background state of the equatorial Pacific (Philander et al., 1984; Hirst, 1986). The goal of this study is to determine which of these two synchronization mechanism best explains the observed seasonal characteristics of ENSO.

Evidence supporting frequency locking of ENSO to the annual cycle as a synchronization mechanism comes from investigating the behaviour of ENSO models under the variation of relevant model parameters, in particular the simple delay oscillator model (Suarez and Schopf, 1988) and the intermediate complexity Zebiak-Cane model (hereafter ZC model, Zebiak and Cane (1987)). Generally, a parameter related to the amplitude/growth rate of the model's ENSO is varied along with a parameter related to the strength of the seasonal forcing (e.g. Tziperman et al. (1995)) or the intrinsic frequency of the ENSO mode (e.g. Jin et al. (1996)). Within the resultant model parameter space, frequency locked solutions are a common feature. This is due to the fact that the various ENSO models used in such studies, though differing in details, each follow the quasiperiodic route to chaos and thus admit the same suite of possible model solutions: quasiperiodic solutions that include both the annual cycle and ENSO frequencies, frequency-locked solutions where the ENSO frequency is a rational multiple of the annual cycle, and chaotic solutions that result from the overlapping of multiple frequency locked solutions within the model parameter space (Tziperman et al., 1995; Jin et al., 1996). This behavior has been demonstrated within the periodically forced delay oscillator (Tziperman et al., 1994; Liu, 2001), a two equation dynamic system model of ENSO (Wang and Fang, 1996), the ZC model (Tziperman et al., 1995; Pan et al., 2005), and variations of the ZC model that include coupling the atmosphere to total SST (Chang et al., 1994) and reducing the ocean component to zonal equatorial strip with fixed meridional structure (Jin et al., 1994, 1996).

As the various ENSO models each follow the quasiperiodic route to chaos, one can investigate the model results simultaneously by examining the relevance of each type of model solution to the observed ENSO synchronization. Quasiperiodic solutions do not reproduce the observed ENSO seasonal synchronization, and frequency locked solutions do not reproduce the observed ENSO irregularity, so realistic solutions must either be chaotic or frequency locked solutions that are perturbed by high frequency atmospheric forcing. Chaotic solutions are relatively rare compared to quasiperiodic and frequency locked solutions (Jin et al., 1996), so the most likely realistic solution is a frequency locked solution perturbed by stochastic noise. Additionally, both chaotic and stochastically forced solutions retain the *subharmonic* peaks in the ENSO spectra that are characteristic of the frequency-locked solutions (Jin et al., 1996). Thus, the results from the various studies can be fairly said to support the theory that ENSO synchronization results from frequency locking of ENSO to the annual cycle.

Alternatively, several physical processes have been proposed whereby the annual cycle could affect the growth rate of ENSO anomalies, beginning with the idea that the seasonal movement of the Intertropical Convergence Zone (ITCZ) should have a strong effect on the coupled instability of the equatorial Pacific ocean-atmosphere system because of its influence on atmospheric heating (Philander, 1983). Analytical results based on a suite of four linear coupled models showed that the unstable modes allowed by the models were highly dependent on the parametrization of SST anomalies and large scale latent heating, and that the observed climatological background state did not permit the growth of ENSO-like instabilities (Hirst, 1986). However, ENSO events could be initialized during more favorable conditions, including high SST, a shallow thermocline, a large zonal SST gradient, and strong surface winds (Hirst, 1986). Isolating the effect of individual variables within the ZC model indicated that the seasonality in the wind divergence (Tziperman et al., 1997) and SST (Yan and Wu, 2007) fields are most critical to the synchronization of ENSO events. Sensitivity analysis of a hybrid coupled model, used to capture the structure of the mixed layer and thermocline, found that the seasonal outcropping of the thermocline increased the coupled instability of the model by linking thermocline anomalies to the surface (Galanti et al., 2002). Lastly, at the end of the calendar year the location of ENSO-associated western Pacific wind anomalies shift from along the equator to the southern hemisphere , which forces oceanic equatorial Kelvin waves that act to reduce or reverse the eastern equatorial Pacific SST anomalies (Harrison and Vecchi, 1999). The shift in wind anomalies has been linked to the southward displacement of highest SST in boreal winter (Lengaigne et al., 2006), which is associated with increased convection and minimal surface momentum damping of wind anomalies (McGregor et al., 2012). The wind shifts have also been associated with a recently identified climate mode with energy at *combination tone* frequencies that emerges through an atmospheric nonlinear interaction between ENSO and the annual cycle (Stuecker et al., 2013).

The effect of the seasonal cycle on ENSO variance has been confirmed statistically by studies that examine the optimal perturbation growth around a seasonally varying background state within both ENSO model output and observations. For example, singular vector decomposition of a linearized version of the ZC model (Thompson and Battisti, 2000), as well as the ZC forward tangent model along a trajectory in reduced EOF space (Xue et al., 1997), result in singular values that have a strong seasonal dependence, with growth of the singular vectors peaking in boreal winter. Similary, cyclic Markov models derived from the ZC model (Pasmanter and Timmermann, 2003), an anomaly coupled GCM (Kallummal and Kirtman, 2008), and observations (Johnson et al., 2000), reveal a stong seasonality in the internal dynamics of the equatorial Pacific coupled ocean-atmosphere system. It has been suggested that this internal seasonality is sufficient to produce the observed the ENSO seasonal variance, without the need for nonlinear dynamics or seasonality in the noise forcing (Thompson and Battisti, 2000; Kallummal and Kirtman, 2008; Stein et al., 2010). Moreoever, the Markov models can be explicitly related to Floquet analysis (Pasmanter and Timmermann, 2003), which can be used to show that the dynamics of most unstable mode of the ZC model with a seasonally varying background are the same as in the annual average case (Jin et al., 1996; Thompson and Battisti, 2000), which forms the basis of our dynamical understanding of ENSO (Philander et al., 1984; Hirst, 1986; Neelin and Jin, 1993a,b).

In this study, a parametric recharge oscillator (PRO) model of ENSO is employed to determine the effects of the seasonally varying background instability on a variety of ENSO synchronization metrics. Analytical solutions for the model's seasonal variance, amplitude modulation, and phase synchronization are obtained, and are shown to match well with observations and the variety of ENSO behavior identified in state of the art coupled general circulation models (CGCMs). The parametric model is also shown to explain spectral peaks at combination tone frequencies that are present in both the observed and modelled ENSO spectra. Additionally, the ENSO recharge oscillator model is extended to include external periodic forcing by the annual cycle and a cubic damping term, in order to produce frequency locked model solutions. The extended model corresponds to the well-known van der Pol oscillator (van der Pol, 1927), which exhibits frequency locking through so-called Arnol'd tongues (Arnold et al., 1983), with global behavior similar to the ENSO models used in previous studies. The van der Pol oscillator is used to examine the relevance of the frequency locking scenario to ENSO seasonal synchronization, ultimately demonstrating that the observed ENSO lacks the characteristics of a frequency locked oscillation.

The remainder of this dissertation is organized as follows: Chapter 2 discusses features of ENSO synchronization based upon the Nino3.4 index. ENSO synchronization is described using a variety of metrics, including seasonal variance, amplitude modulation, phase synchronization, and secondary peaks in the ENSO spectrum. These features are examined both for the observations and within a range of state of the art coupled general circulation models. Chapter 3 repeats the analysis of ENSO metrics using complex empirical orthogonal function (CEOF) analysis, comparing the results to the metrics calculated with the Nino3.4 index. Results from the two methods are very similar, demonstrating that including the modulation of the annual cycle and the additional spatial information from the CEOFs is not necessary for a description of ENSO synchronization that is sufficient to distinguish the two leading theories of ENSO synchronization. This allows for the analysis of ENSO synchronization to be based on the Nino3.4 index, which is dynamically consistent with the recharge oscillator framework. Chapter 4 discusses the analytical solution of a simplified neutrally-stable version of the parametric recharge oscillator (PRO) following the perturbation expansion of An and Jin (2011). The solutions demonstrate that the observed features of ENSO-annual cycle interaction arise directly from the modulation of the growth rate parameter within the model. Numerical experiments with the parametric recharge oscillator are presented in Chapter 5, demonstrating that the analytical solutions presented in Chapter 4 apply both to the neutrally stable unforced version of the PRO model as well as the damped version forced by Gaussian stochastic noise. Solutions within the subset of the model's parameter space relevant to ENSO are discussed. A derivation of the van der Pol oscillator from the extended oscillator model is shown in Chapter 6, which is used to examine the likelihood that ENSO synchronization is due to subharmonic frequency locking. The observed ENSO is shown to be lacking the characteristics of a frequency locked oscillation. A discussion of the implications and caveats concerning the work herein is presented in Chapter 7, and the paper concludes with a summary of major results in Chapter 7.

Chapter 2

Features of ENSO synchronization: Nino3.4 index

In order to test the two leading theories of ENSO synchronization, it is necessary to construct a detailed picture of ENSO synchronization using a variety of different metrics. This study examines the synchronization theories within the recharge oscillator model framework; to allow for direct comparison with model results, the synchronization metrics are calculated from the Nino3.4 index time series, defined as the area average of SSTA between 5°N-5°S and $120° - 170°$ W. The metrics were also calculated using time series of ENSO derived from complex emirical orthogonal functions (CEOFs, Chapter 3), and the results are very similar due to the fact that ENSO anomalies are large scale and occur in phase across the central Pacific (Stein et al., 2011).

Figure 2.1 (top, black) shows the monthly Nino3.4 SSTA index based on data from the National Oceanic and Atmospheric Administration's Extended Reconstructed Sea Surface Temperature version 3b data set (ERSST.v3b, Smith et al. (2008)) from the year 1950 to 2011, with the monthly mean climatology (bottom left) and long-term trend removed. The Nino3.4 SSTA index $T(t)$, can be expressed as a cyclostationary process $T(y, m)$, where y is the year, m the month, and $T(y, m + 12) = T(y + 1, m)$. The monthly variance is then determined as $\sigma_m^2 = E[T(y, m)^2]$, where E indicates the expected value and we have made use of the fact that the monthly means have been removed from the time series. Figure 2.1 (bottom center) shows the monthly variance of the Nino3.4 SSTA index, which has a minimum in variance in March-April and highest variance in December, reflecting the tendency for ENSO events to peak in boreal winter.

The seasonally modulated variance is an expression of either a phase synchronization of ENSO with the annual cycle (Stein et al., 2011), the seasonal modulation of ENSO's amplitude, or a combination of the two. To separate the processes, it is necessary to construct a state space that allows for the definition of ENSO magnitude and phase. A well-known method for defining amplitude and phase from a data set, and the one most naturally applied to climate data, is to construct the analytical signal (Gabor, 1946) of the data using the Hilbert transform (Pikovksy et al., 2000). The analytical signal $\widehat{T(t)}$ of the Nino3.4 SSTA index is defined as

$$\widehat{T(t)} = T(t) + i\mathcal{H}[T(t)], \tag{2.1}$$

where $\mathcal{H}[T(t)]$ is the Hilbert transform of T, and $i = \sqrt{-1}$. The top panel of Figure 2.1 shows the time series of the Hilbert transform of the Nino3.4 SSTA index (grey dashed). The amplitude and phase of the index can be calculated from the complex analytical signal $\widehat{T(t)}$, based on a Cartesian to polar coordinate transform

$$\begin{aligned} \alpha(t) &= \sqrt{\mathrm{Re}[\widehat{T}]^2 + \mathrm{Im}[\widehat{T}]^2}, & (2.2) \\ \phi_e(t) &= \mathrm{Arg}\frac{\mathrm{Im}[\widehat{T}]}{\mathrm{Re}[\widehat{T}]}, & (2.3) \end{aligned}$$

where Arg is the principal value of the arg function of complex numbers, defined such that $\widehat{T} = \alpha e^{i\phi_e}$. For consistency, all phase values considered here will be calculated modulo 2π, and therefore on the interval $[0, 2\pi)$.

The monthly mean amplitude of the analytical signal of the Nino3.4 SSTA index, $\alpha_m = E[\alpha(y, m)]$, is compared to the monthly variance of $T(t)$ in Figure 2.1 (bottom center). There is an indication of amplitude modulation of the complex signal by the seasonal cycle, with maximum mean ENSO amplitude occurring in boreal winter, but with a minimum in September, which does not correspond to the minimum in monthly variance of the direct Nino3.4 SSTA index. The overall strength of the seasonal amplitude modulation of analytical signal $\widehat{T}(t)$ is insufficient to reproduce the observed seasonal variance of $T(t)$, indicating phase synchronization must also play a role.

To investigate the phase synchronization of ENSO with the annual cycle, we define the generalized phase difference

$$\delta\phi_{k,l}(t) = k\phi_e(t) - l\phi_a(t), \tag{2.4}$$

where ϕ_e is the ENSO phase[1] (2.3), ϕ_a is the annual cycle phase, and $k, l \in \mathbb{Z}^+$. If the phase difference were constant the annual cycle and ENSO would be perfectly synchronized, and if the values of $\delta\phi_{k,l}(t)$ were equally distributed throughout the 2π range then the two modes would have no phase relationship. Phase locking is defined as a bounded $\delta\phi_{k,l}$ difference, i.e. if $|\delta\phi_{k,l}(t) - s| < c$, where $c < 2\pi$ is a constant and s is the average phase shift between the two time series (Pikovksy et al., 2000). Because the monthly mean climatology was removed from the Nino3.4 SSTA index, the annual cycle is fixed, and we will define the phase of the annual cycle to be $\phi_a(t) = (\omega_a t) \mod 2\pi$, where $\omega_a = \frac{2\pi}{12}$ month^{-1} is the annual cycle angular frequency.

Figure 2.1 (bottom right) shows a histogram of $\delta\phi_{2,1}$, indicating the strength of the 2:1 phase synchronization of ENSO to the annual cycle, the only ratio that was found to show significant phase synchronization (Stein et al. (2011), see Section 6). The phase difference between the two signals is not bounded, indicating that ENSO is not strictly phase locked to the annual cycle throughout the observable record. However, certain phase differences are three times more likely than others, which is evidence of partial 2:1 phase synchronization of ENSO to the annual cycle.

---

[1] The $\phi(t)$ time series as calculated from the analytical signal are in fact the proto-phase of the time series, which may differ from the true phase (Kralemann et al., 2008). However, the differences between the proto-phases and phases calculated in this study are negligible and the transformation to true phase has no effects on the results, so a discussion of this complexity is omitted.

In terms of existing ENSO theory, such behavior could be explained by intermittent periods of frequency locking of ENSO to the annual cycle. However, the 2:1 phase synchronization of ENSO to the annual cycle is not associated with a distinct peak in the Nino3.4 spectrum at 0.5 years^{-1} (Fig. 2.2), as would be expected if the phase synchronization behaviour was due to frequency locking.[2] (See Chapter 6). Instead, the primary ENSO spectral peak occurs at 0.23 years^{-1}, along with a second secondary peaks at 0.77 and 1.23 years^{-1}, though the higher frequency peak is not statistically significant based on the spectrum from a first order autoregressive fit of the Nino3.4 time series (Fig. 2.2). The secondary peaks occur at combination tones frequencies $\omega_a \pm \omega_e$, which indicative of nonlinear interaction between ENSO the annual cycle (McGregor et al., 2012; Stuecker et al., 2013) and arise directly form the modulation of ENSO growth rate within the parametric recharge oscillator model (An and Jin (2011), see Section 4).

To demonstrate that the above features of ENSO's seasonal synchronization are robust, we examine the synchronization of a variety of different model-based representations of ENSO and the annual cycle, as simulated by state of the art coupled general circulation models participating in the Coupled Model Intercomparison Project Phase 5 (CMIP5, Taylor et al. (2012)). The detrended Nino3.4 SST index was calculated from CMIP5 historical run output for each model, covering model years 1901-2000. The annual cycles of the Nino3.4 SST index for each model are compared in Figure 2.3, the monthly variance of the Nino3.4 SSTA indices are compared in Figure 2.4, and the $\delta\phi_{2,1}$ phase differences with the annual cycle are compared in Figure 2.5. The models have been ordered according to the strength of the seasonal synchronization of ENSO to the annual cycle (as measured by the ν index, defined below).

As can be seen in Figure 2.3, the CMIP5 CGCMs show a variety of differing amplitudes for the annual cycle of the Nino3.4 SSTA index. The annual cycles for all the models are more symmetric than the observations (Figure 2.1, bottom left), showing a warming for six months out of the year rather than four, but the timing of the warm to cold phase transitions for the models is in agreement with the observations. In particular, there are no semiannual seasonal cycles, allowing for the use of a single sinusoidal function at the annual frequency as the proxy for the annual cycle in the models, as with the observations. The models also display a variety of behavior in terms of overall ENSO variance and the strength of the seasonal modulation of ENSO variance (Figure 2.4). For most models, total ENSO variance and the magnitude of the seasonal modulation of ENSO variance are both weaker than observations, which is reflected in the flatter distributions of phase differences between ENSO and the annual cycle (Figure 2.5). The seasonal variance of each model ENSO (Figure 2.4) shows a peak in December/January, and so the most likely $\delta\phi_{2,1}$ phase differences for each model are all near the same value (Figure 2.5).

---

[2] Note that the definition of frequency locking ($\frac{k\omega_e}{l\omega_a} = 1$, where $\omega_a = \frac{d\phi_a}{dt}$ is the annual cycle frequency, $\omega_e = \frac{d\phi_e}{dt}$ is the ENSO frequency, and $k, l \in \mathbb{Z}^+$) is stronger than that for phase locking.

To examine any systematic relationship between synchronization characteristics across all the CMIP5 CGCMs, we define three indices relating to ENSO's seasonal variance, 2:1 phase synchronization, and amplitude modulation of the corresponding complex analytical signal. The first index simply captures the range of the monthly ENSO variance,

$$\nu = \frac{max[\sigma_m^2] - min[\sigma_m^2]}{max[\sigma_m^2]}, \tag{2.5}$$

and will be referred to as the "seasonal variance index." The index ranges from 0 to 1, where 0 indicates that each month has exactly the same variance throughout the year and 1 indicates that the variance of a particular month drops to zero.

An index for the strength of the $2:1$ phase synchronization between ENSO and the annual cycle can be defined as

$$\chi = \left| \left\langle e^{i(2\phi_e - \phi_a)} \right\rangle_t \right|, \tag{2.6}$$

where ϕ_a is the annual cycle phase, ϕ_e is the ENSO phase, and $\langle ... \rangle_t$ indicates temporal averaging (Kralemann et al., 2008). The index is a measure of the length of the vector in the complex plane that results from the temporal averaging of unit vectors with angles equal to the phase difference $\delta\phi_{2,1}$. The index varies from zero to one, with zero indicating that the phase of the two time series are completely independent and one indicating perfect phase synchronization. Similarly, one can define an index that captures the strength of the complex amplitude modulation of ENSO by the annual cycle as

$$\Psi = \frac{\left|\left\langle \alpha e^{i(\phi_a)} \right\rangle_t\right|}{\langle \alpha \rangle_t}, \tag{2.7}$$

where α is the ENSO amplitude time series (2.2). The index is the temporal average of the vectors in the complex plane defined by the ENSO amplitude and annual cycle phase, which is then normalized by the mean ENSO amplitude. The index varies from zero to one, with zero indicating that the complex ENSO amplitude is equal across all phases of the annual cycle, and one indicating that ENSO's analytical signal only has a finite amplitude at a single time of the year, and has zero amplitude at all other times. As such, the values of the Ψ index would be expected to be much smaller than the the values of the other two indices, and these indices should not be directly compared, such that a value of χ that is larger than Ψ is interpreted as stronger phase synchronization than amplitude modulation. Rather, the indices measure the changing strength of these processes across the CMIP5 models.

Figure 2.6 shows scatter plots of the seasonal variance index (ν) versus the complex amplitude modulation index (Ψ, top) and the 2:1 phase synchronization index (χ, bottom) for each of the CMIP5 models and the observations. Most models simulate ENSOs that are more weakly synchronized with the annual cycle than the observed ENSO. The seasonal variance of ENSO (ν) is linearly related to the strength of the phase synchronization of ENSO to the annual cycle (χ), while the strength of the amplitude modulation (Ψ) is not as closely related, though the Ψ index does tend to be larger for models with a larger range of seasonal ENSO variance. The models that display the strongest synchronization of ENSO to the annual cycle also display peaks at one or both of the $\omega_a \pm \omega_e$ combination tone frequencies, as seen in Figure 2.7. Five of the first six models

(CNRM-CM5, FGOALS-g2, CanESM2, bcc-csm1-1, Giss-E2-R) show a significant peak at the $\omega_a - \omega_e$ combination tone, and all but three of the models show a spectral peak at at least one combination tone, though the peaks are statistically significant in only nine of the sixteen models (CNRM-CM5, FGOALS-g2, CanESM2, bcc-csm1-1, Giss-E2-R, NorESM1-ME, Giss-E2-H, GFDL-ESM2M, CCSM4). Four of the sixteen models (CNRM-CM5, FGOALS-g2, CanESM2, Giss-E2-R) also display a spectral peak at the two year period, but each of these models also shows a peak at a combination tone frequency. It is unclear at this point whether the spectral peak at periods of two years in these models is due to frequency locking, parametric resonance, or another mechanism. However, it is apparent that overall ENSO seasonal synchronization is more often associated with peaks in the ENSO spectrum at combination tone frequencies, as opposed to a peak at $\frac{1}{2}$ years^{-1}. In Chapter 4, we will show how the $\omega_a \pm \omega_e$ spectral peaks, along with ENSO's seasonal variance, amplitude modulation, and partial 2:1 phase synchronization, all arise directly from the modulation of ENSO's growth rate by the annual cycle within the parametric recharge oscillatory model of ENSO. Before doing so, the results presented in this chapter are compared to the results of the same analysis utilizing complex empirical orthogonal function analysis, which was the technique used to first identify the partial 2:1 phase synchronization of ENSO to the annual cycle (Stein et al., 2011).

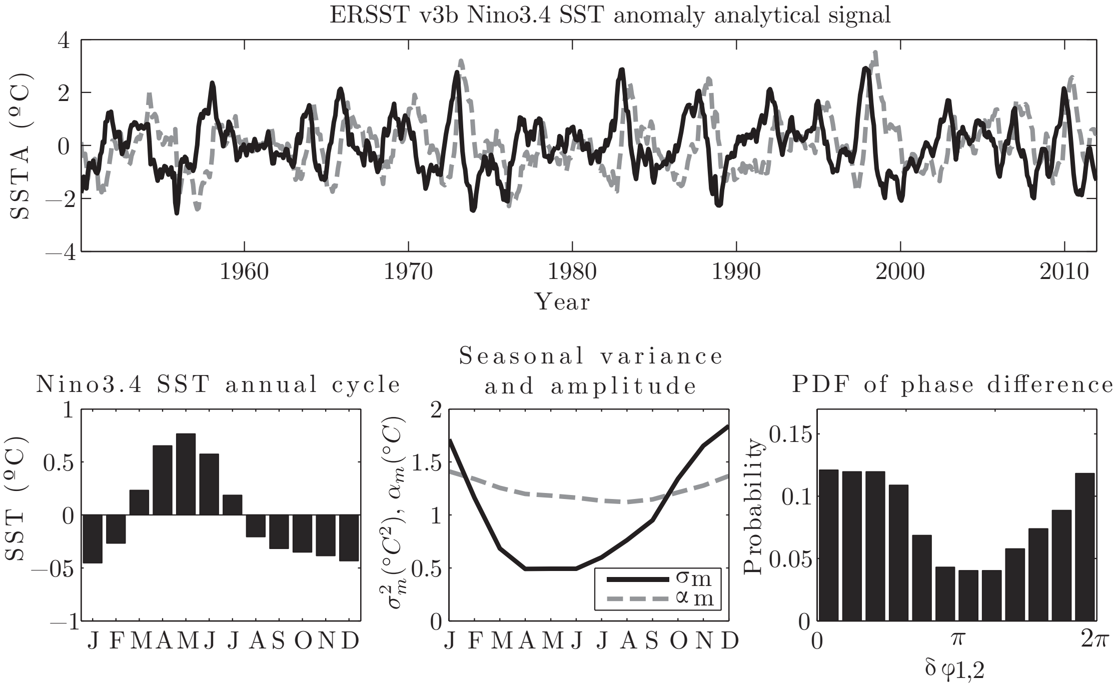

Figure 2.1: (Top) The time series of the Nino3.4 SSTA index (black) and the Hilbert transform of the index (gray dashed), calculated from the ERSST.v3b data set. (Bottom left) The monthly deviations of Nino3.4 SST from the time mean. (Bottom center) The monthly variance of the Nino3.4 SSTA index and the monthly amplitude of the analytical signal of the index. (Bottom right) A PDF of the $\delta\phi_{2,1}$ phase difference of ENSO with the annual cycle, indicating the strength of the phase synchronization of ENSO to the annual cycle. See text for the definitions of the analytical signal, amplitude, and phase.

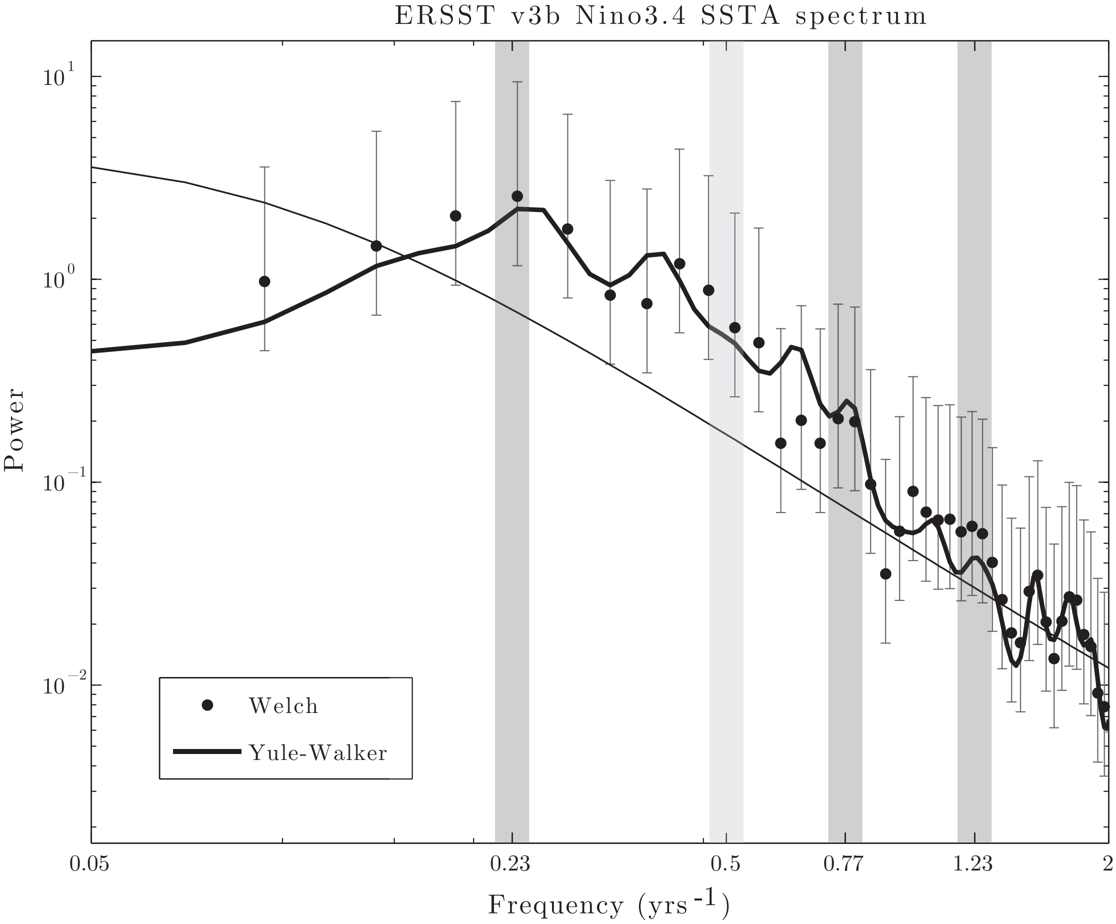

Figure 2.2: The spectrum of the ERSST.v3b Nino3.4 SSTA index, as calculated using the Yule-Walker (thick line) and Welch (dots) spectral estimation methods. The 95% confidence intervals of the Welch spectrum are indicated. The spectrum of a first order autoregressive model fit to the Nino3.4 SSTA index is shown for comparison (thin line). The grey bars are located at the frequency of the primary ENSO peak, the biennial frequency, and $\omega_a \pm \omega_e$ combination tone frequencies.

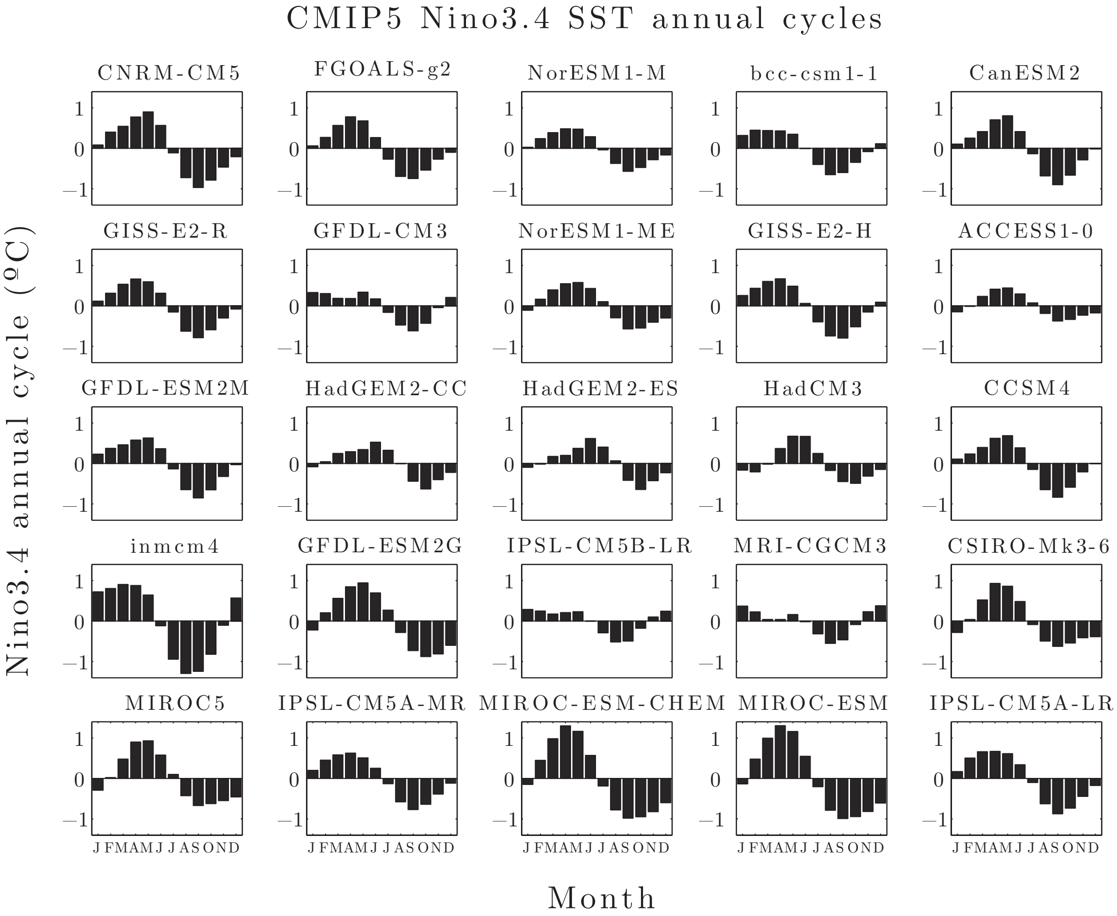

Figure 2.3: The annual cycles of the Nino3.4 SST indices calculated from historical runs of CGCMs participating in CMIP5. Models are organized according to the strength of the seasonal modulation of ENSO variance.

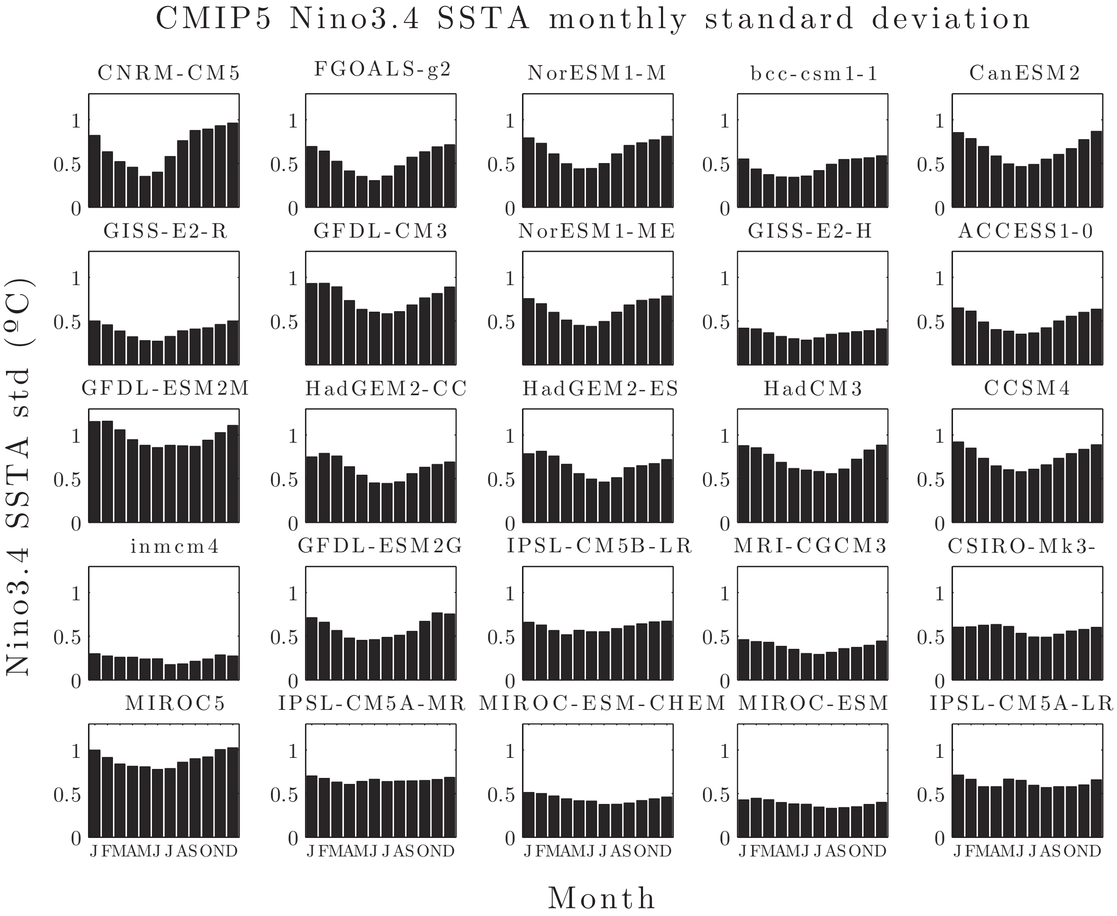

Figure 2.4: The seasonal variance of the Nino3.4 SSTA indices calculated from historical runs of CGCMs participating in CMIP5. Models are organized according to the strength of the seasonal modulation of ENSO variance.

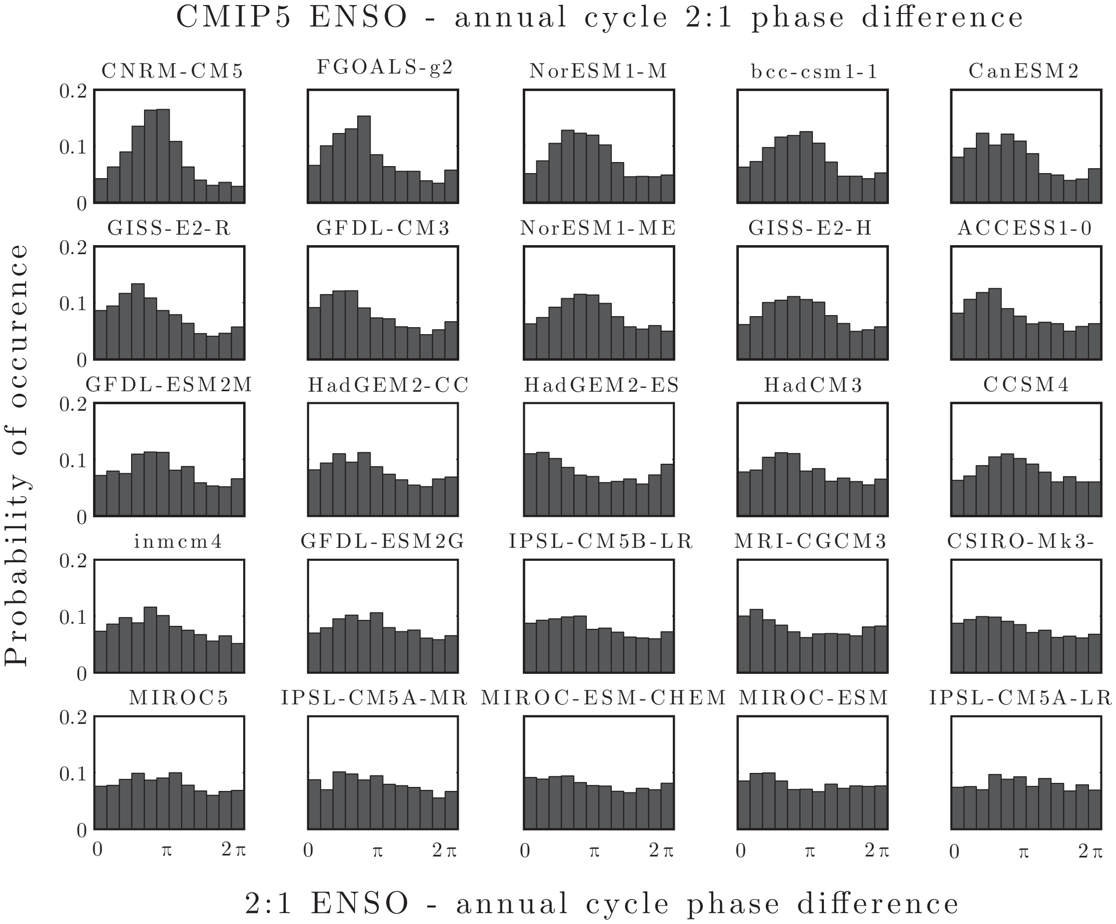

Figure 2.5: PDFs of the $\delta\phi_{2,1}$ phase difference between the annual cycles and the Nino3.4 SSTA indices calculating from historical runs of CGCMs participating in CMIP5. Models are organized according to the strength of the seasonal modulation of ENSO variance.

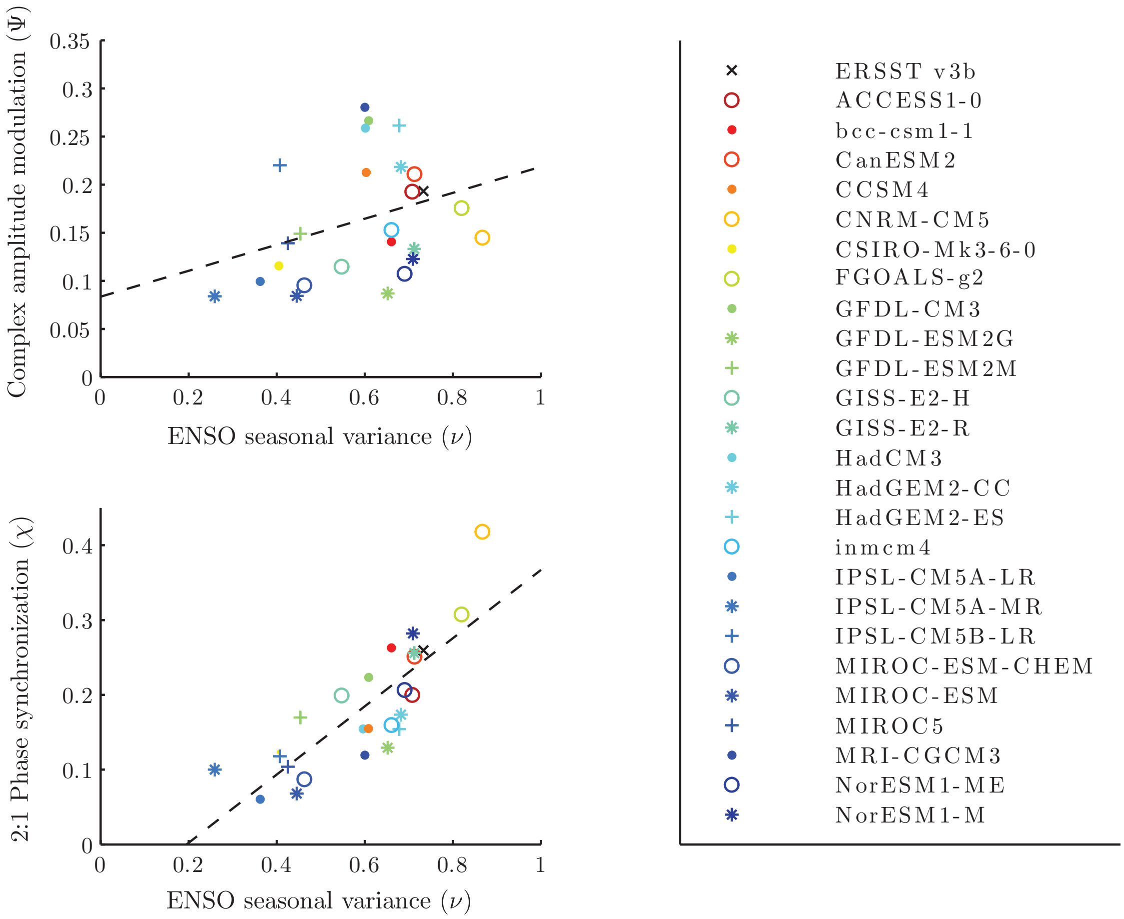

Figure 2.6: Scatter plots of the amplitude modulation index (Ψ,top) and the phase synchronization index (χ, bottom) versus the seasonal variance index (ν) based on the observations and CGCMs participating in CMIP5. See text for the definitions of the synchronization indices.

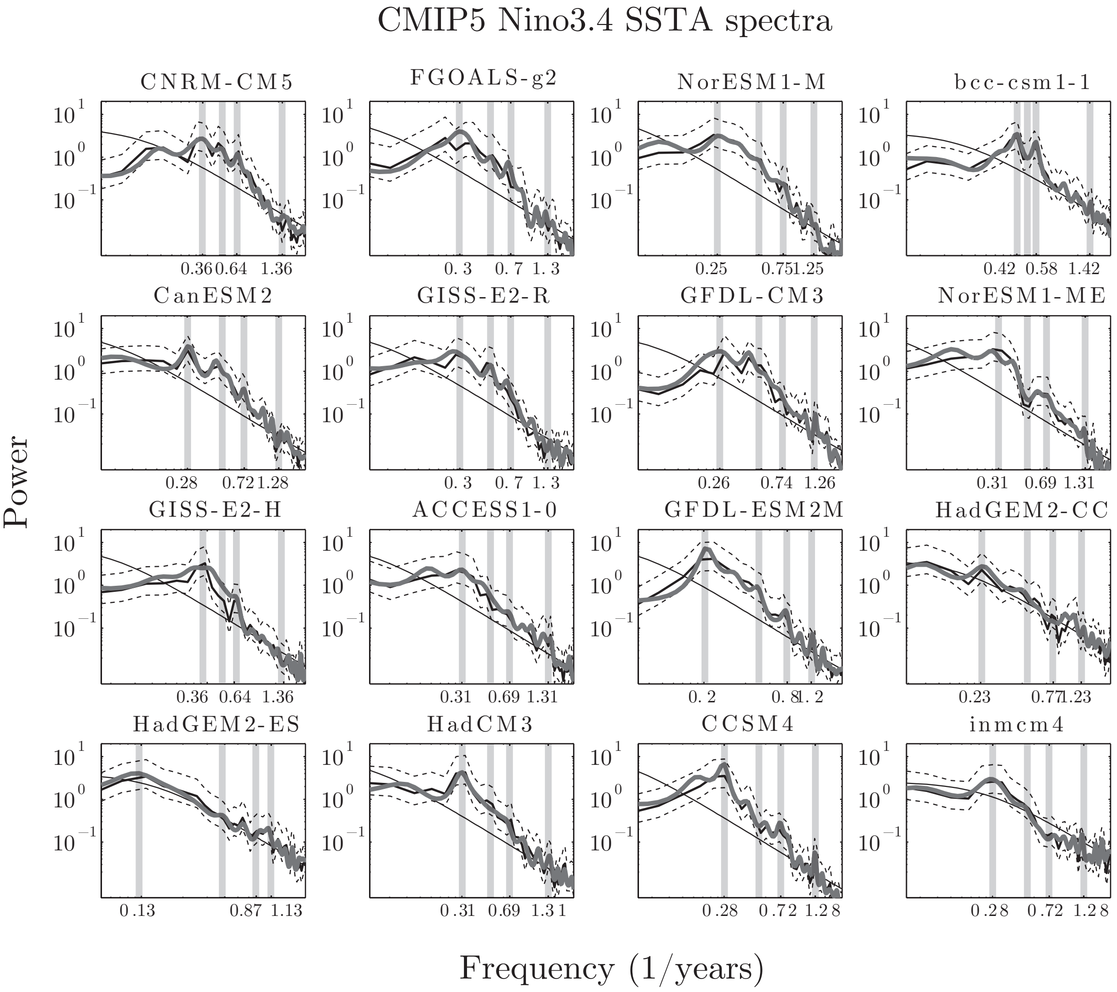

Figure 2.7: The spectrum of the Nino3.4 SSTA index index anomalies of CMIP5 CGCM historical runs, as calculated using the Yule-Walker (thick grey) and Welch (thin black) spectral estimation methods. The 95% confidence intervals of the Welch spectrum are indicated (dashed). The spectrum of a first order autoregressive model fit to the Nino3.4 SSTA index is shown for comparison (thin line). The grey bars are located at the frequency of the primary ENSO peak, the biennial frequency, and the $\omega_a \pm \omega_e$ combination tone frequencies.

Chapter 3

Features of ENSO synchronization: CEOF analysis

Complex emipircal orthogonal function (CEOF) analysis (Barnett, 1983) potentially offers a more complete description of ENSO synchronization than the one based on the analytical signal of the Nino3.4 index for two main reasons. First, CEOF analysis incorporates more spatial information than the Nino3.4 analytical signal because the time series associated with each CEOF mode represents a propagating spatial pattern within the larger domain of the equatorial Pacific. Second, the CEOF analysis produces a modulated annual cycle time series, thereby describing ENSO-annual cycle synchronization in terms of two coupled modes, as opposed to the single ENSO mode being periodically modulated by the annual cycle. In this chapter, ENSO synchronization metrics are recalculated utilizing time series based on a CEOF analysis of ERSST.v3b observations and compared to the results based on the analytical signal of the Nino3.4 index. The two sets of results are very similar, indicating that for the purpose of this study, namely differentiating the two leading theories of ENSO synchronization, the analytical signal of the Nino3.4 index is sufficient.

Again, the ERSST.v3b data set is used, in the spatial domain 20°S to 20°N, 110°E to 290°E, and the temporal domain 1950-2011. Both the long term mean and the linear trend of the data set are removed. This spatio-temporal data set is denoted $\mathbf{s}(t)$, where the vector components represent the individual spatial grid points and t is time.

Complex EOFs are calculated in exactly the same way as real-valued EOFs, with the single additional step of calculating the analytical signal of each spatial point in $\mathbf{s}(t)$ before performing the EOF decomposition (Preisendorfer, 1988). In vector notation, one obtains

$$\mathbf{a}(t) \quad = \quad \mathbf{s}(t) + i\,\mathcal{H}[\mathbf{s}(t)]. \tag{3.1}$$

The spatial covariance matrix $\mathbf{C}$ of the complex analytical signal vector $\mathbf{a}(t)$ is then given by

$$\mathbf{C} = \langle \mathbf{a}^*(t) \otimes \mathbf{a}(t) \rangle_t, \tag{3.2}$$

where $\otimes$ is the outer (tensor) product and the asterisk denotes complex conjugation. Because $\mathbf{C}$ is self-adjoint, it possess real eigenvalues λ_n and complex eigenvectors $\mathbf{e}_n = (e_{n,j})$ with $j = 1, ...N$, representing the N spatial data points. The complex eigenvectors of $\mathbf{C}$ correspond to the spatial fields in the CEOF representation of $\mathbf{a}(t)$, which is written as

$$\mathbf{a}(t) = \sum_n p_n(t) \mathbf{e}_n^*, \tag{3.3}$$

where the complex principal component time series $p_n(t)$ are computed via the projection $p_n(t) = \sum_x \mathbf{a}(t) \cdot \mathbf{e}_n$. The vectors can be normalized such that

$$\langle p_n p_m^* \rangle_t \quad = \quad \delta_{nm} \tag{3.4}$$

$$\mathbf{e}_n \cdot \mathbf{e}_m^* \quad = \quad \lambda_n \delta_{nm}, \tag{3.5}$$

where δ_{nm} is Kronecker's delta. The combination of the principal component time series $p_n(t)$ and the spatial vectors $\mathbf{e}_n$ is referred to as the n-th mode of the CEOF representation. The fraction of the total data set variance associated with the n-th mode is given by $\lambda_n / \sum \lambda_m$ (Preisendorfer, 1988). By convention, the first mode accounts for the largest amount of variance in $\mathbf{a}(t)$, the second mode the second largest amount of variance, and so on.

The magnitude and phase for both the spatial fields and time series of each mode can be computed in the same manner as for the analytical signal of the Nino3.4 index. For each spatial component j of the vector field we obtain:

$$q_{n,j} = \sqrt{\mathrm{Re}[e_{n,j}]^2 + \mathrm{Im}[e_{n,j}]^2}, \qquad r_{n,j} = \mathrm{Arg}\frac{\mathrm{Im}[e_{n,j}]}{\mathrm{Re}[e_{n,j}]} \tag{3.6}$$

$$\alpha_n(t) = \sqrt{\mathrm{Re}[\alpha_n]^2 + \mathrm{Im}[p_n]^2}, \qquad \phi_n(t) = \mathrm{Arg}\frac{\mathrm{Im}[p_n]}{\mathrm{Re}[p_n]}, \tag{3.7}$$

where $\alpha_n(t), \phi_n(t)$ are the amplitude and phase of the nth principal component time series and $\mathbf{q_n}, \mathbf{r_n}$ are the associated amplitude and phase spatial patterns.

Figure 3.1 shows the magnitudes $(\mathbf{q}_1, \alpha_1)$ and phases $(\mathbf{r}_1, \phi_1)$ of the spatial patterns and the time series of the first mode obtained from the CEOF analysis, accounting for the 77.3% of variance in $\mathbf{a}(t)$. The mode captures the annual cycle of the ERSST.v3b data set, displaying a very regular phase progression in time and westward propagation along the equator in the phase spatial structure. The node line of the phase spatial structure located north of the equator in the central to eastern tropical Pacific is due to the influence of the Intertropical Convergence Zone (ITCZ) (Horel, 1982; Xie, 1994), which acts as the "climatological equator." The areas of smallest annual cycle magnitude lie under the ITCZ and the South Pacific convergence zone (SPCZ), while the largest magnitudes are associated with areas of strong upwelling along the equator and the coast of South America and in the eastern Pacific cold tongue.

The second mode (Figure 3.2) accounts for 11.3% of the variance in $\mathbf{a}(t)$, and the largest amount of variance on interannual timescales, thus capturing the dominant mode of ENSO in the time series. The mode displays areas of largest amplitude in the central to eastern Pacific, confined to within approximate 5° of the equator. The SST variation occurs in phase across the central to eastern Pacific, encompasing the area of largest amplitude. El Niño events are represented in the time series by large amplitude values and phase values near zero or 2π, whereas La Niña events are represented by large amplitude values and phase values near π.

The phase time series $\phi_2(t)$ is equivalent to the $\phi_e(t)$ time series obtained from the analytical signal of the Nino3.4 SSTA analytical signal. Similarly, $\alpha_2(t)$ is equivalent to $\alpha(t)$, and $\phi_1(t)$ is equivalent to $\phi_a(t)$, although the progression of the phase time series ($\phi_1(t)$) of the first principal component ($p_1(t)$, PC1) can vary from year to year, as opposed to the fixed progression of $\phi_a(t)$. The ENSO synchronization metrics based on the CEOF analysis are thus calculated as

$$\sigma_m^2 = E\{\mathrm{Re}[p_2(y,m)]^2\} \tag{3.8}$$

$$\delta\phi_{2,1}(t) = 2\phi_2(t) - \phi_1(t) \tag{3.9}$$

$$\alpha_m = E[\alpha_2(y,m)], \tag{3.10}$$

and the indices measuring the strength of each of theses processes (ν,χ,Ψ) are calculated as before (2.5,2.6,2.7).

Figure 3.3 shows ENSO synchronization metrics based on the CEOF decomposition. At the top, the real part of the PC2 time series ($\mathrm{Re}[p_2(t)]$) is compared to the Nino3.4 time series, showing the two time series are highly correlated. This is because the Nino3.4 index is the area average of SST over 5°N-5°S, $190° - 240°$E, lying directly over the area of largest amplitude of the second mode of the CEOF. In turn, the synchronization metrics calculated from the PC2 time series (Figure 3.3, bottom) are very similar to those calculated from the Nino3.4 analytical signal (Figure 2.1). The PC2 time series indicates slightly stronger amplitude modulation that the analytical signal of the Nino3.4 index, and vice versa for the phase synchronization, but overall the two methods produce very similar time series for ENSO and metrics of ENSO synchronization.

The spectrum of the real part of the PC2 time series also displays peaks at the $\omega_a - \omega_e$ sideband, but the peak is not significant based upon comparison to a first order autoregressive fit of the time series (Figure 3.4). This is because the PC2 time series retains significant energy at the annual and semi-annual frequencies, which mask the relatively weaker peak at the combination tone frequency. Removing the monthly averages of the real part of the PC2 time series eliminates the annual and semi-annual peaks (Figure 3.5), producing a spectrum similar to that of the Nino3.4 index (Figure 2.2). The spectrum displays significant energy across interannual frequencies, with a peak at 0.22 years^{-1}, and a associated peak at the combination tone 0.78 years^{-1}. As with the the spectrum of the Nino3.4 index, there is no evidence of a significant peak at the higher $\omega_a + \omega_e$ frequency.

Additionally, CEOF analysis of SST output from the CMIP5 models reveals the same relationship between ENSO seasonal variance, amplitude modulation, and 2:1 phase synchronization with the annual cycle as seen with the analytical signals of the Nino3.4 indices from the models. CEOF analysis was performed on model output of equatorial SST from historical runs, covering model years 1901-2000 and over the same spatial domain as the observations, 20°S - 20°N, 110°E - 290°E. The spatial patterns of the first two modes of each CMIP5 model produced from the CEOF decomposition are included as supplementary figures (Appendix A). Figure 3.6 (top) shows the relationship between the range of the seasonal variance (ν) of the real part of the PC2 time series and the strength of the amplitude modulation (Ψ) of the complex PC2 time series. Below, the relationship between the seasonal variance (ν) and the strength of the 2:1 phase synchronization (χ) between mode 2 (ENSO) and mode 1 (annual cycle) of each model is shown. Two additional SST reanalysis data sets were also included for comparison: the European Centre for Medium-Range Weather Forecasts operational Ocean Re-Analysis System 3 (ECMWF ORA-S3, Balmaseda et al. (2008)) and the UK Met Office Hadley Centre's 1° gridded SST analyses (HadISST Rayner et al. (2003)), with the same spatio-temporal domain as the ERSST.v3b data set.

The CEOF analysis shows the same overall relationships between the synchronization metrics as the analytical signals of the Nino3.4 indices. There is a strong relationship between the range of the seasonal variance (ν) of the PC2 time series and the 2:1 phase synchronization between the ENSO and annual cycle CEOF modes (χ). The strength of the seasonal amplitude modulation (Ψ) of PC2 for each model, on the other hand, has little to no relationship with the range of ENSO variance across CMIP5 models. The linear regression between the ν and χ as calculated from the CEOFs does have the offset seen with the indices based on the Nino3.4 analytical signals, though the exact reason for this is unknown.

The similarity between the ENSO synchronization metrics calculated from CEOFs and the analytical signals of the Nino3.4 indices indicates that the Nino3.4 indices are sufficient to describe ENSO synchronization, based on the metrics used in this study. This result has two interesting repercussions. First, it suggests the including the modulation of the annual cycle, and in particular the feedback of ENSO back onto the annual cycle, is not a necessary component of a theory of ENSO synchronization. This allows for ENSO synchronization to be treated as the single ENSO mode modulated and/or forced by the fixed annual cycle, as opposed to two coupled oscillatory modes, significantly simplifying the problem. Second, use of the Nino3.4 index to describe ENSO synchronization is dynamically consistent with the recharge oscillator framework (Jin, 1997), which will be used to examine the theories of ENSO synchronization in the following chapters.

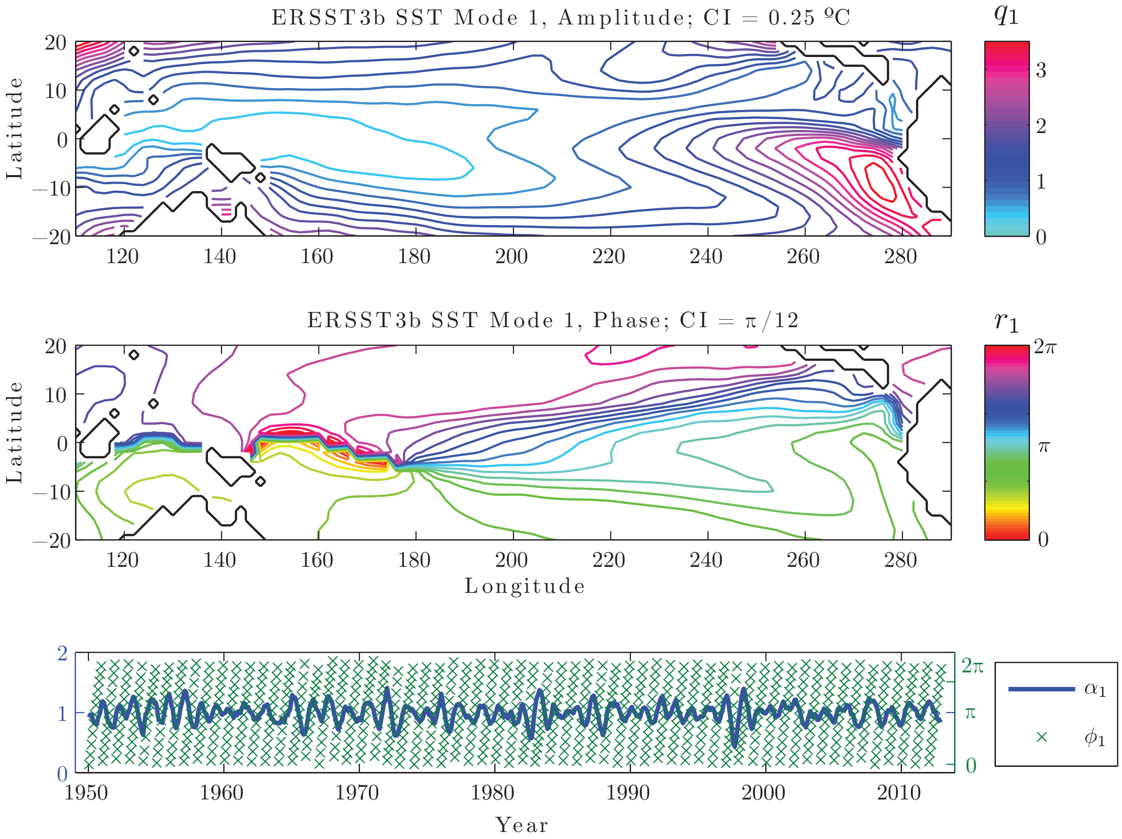

Figure 3.1: The magnitudes $(\mathbf{q}_1, \alpha_1(t))$ and phases $(\mathbf{r}_1, \phi_1(t))$ associated with the first mode obtained from a CEOF analysis of ERSST.v3b data. The contour plots show the spatial maps of $\mathbf{q}_1, \mathbf{r}_1$, with contour intervals indicated on the top right. The corresponding time series $\alpha_1(t)$ (blue line, left ordinate) and $\phi_1(t)$ (green x's, right ordinate) are shown below. The first mode captures the annual cycle of the data set.

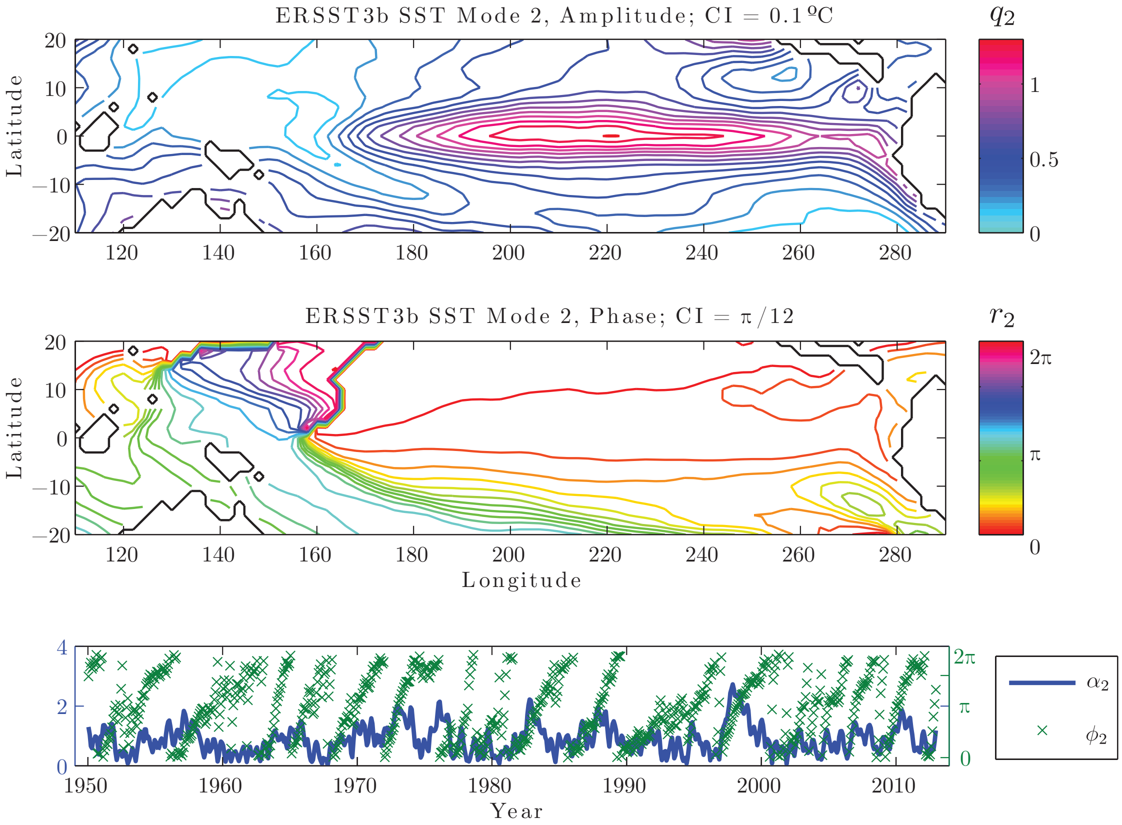

Figure 3.2: The magnitudes $(\mathbf{q}_2, \alpha_2(t))$ and phases $(\mathbf{r}_2, \phi_2(t))$ associated with the second mode obtained from a CEOF analysis of ERSST.v3b data. The contour plots show the spatial maps of $\mathbf{q}_2, \mathbf{r}_2$, with contour intervals indicated on the top right. The corresponding time series $\alpha_2(t)$ (blue line, left ordinate) and $\phi_2(t)$ (green x's, right ordinate) are shown below. The second mode captures the dominant ENSO mode in the data set.

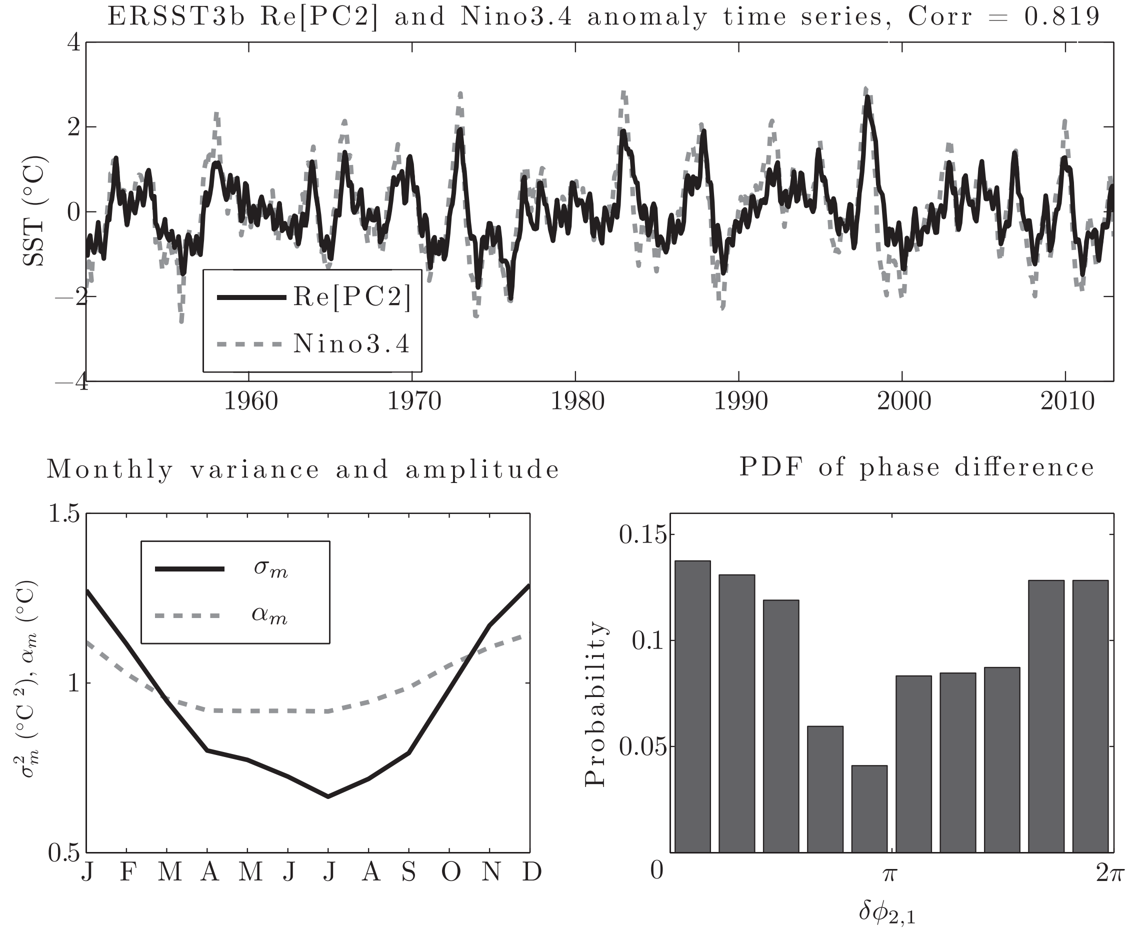

Figure 3.3: (Top) The time series of the real part of the ERSST.v3b CEOF PC2 time series (Re[$p_2(t)$],black) and the Nino3.4 SSTA index (gray dashed), calculated from the ERSST.v3b data set. (Bottom left) The monthly variance (σ_m) of the real part of the PC2 time series and the monthly amplitude (α_m) of the complex PC2 time series. (Bottom right) A PDF of the $\delta\phi_{2,1}$ phase difference of ENSO (ϕ_2) with the annual cycle ϕ_1, indicating the strength of the phase synchronization of ENSO to the annual cycle. See text for the definitions of the analytical signal, amplitude, and phase.

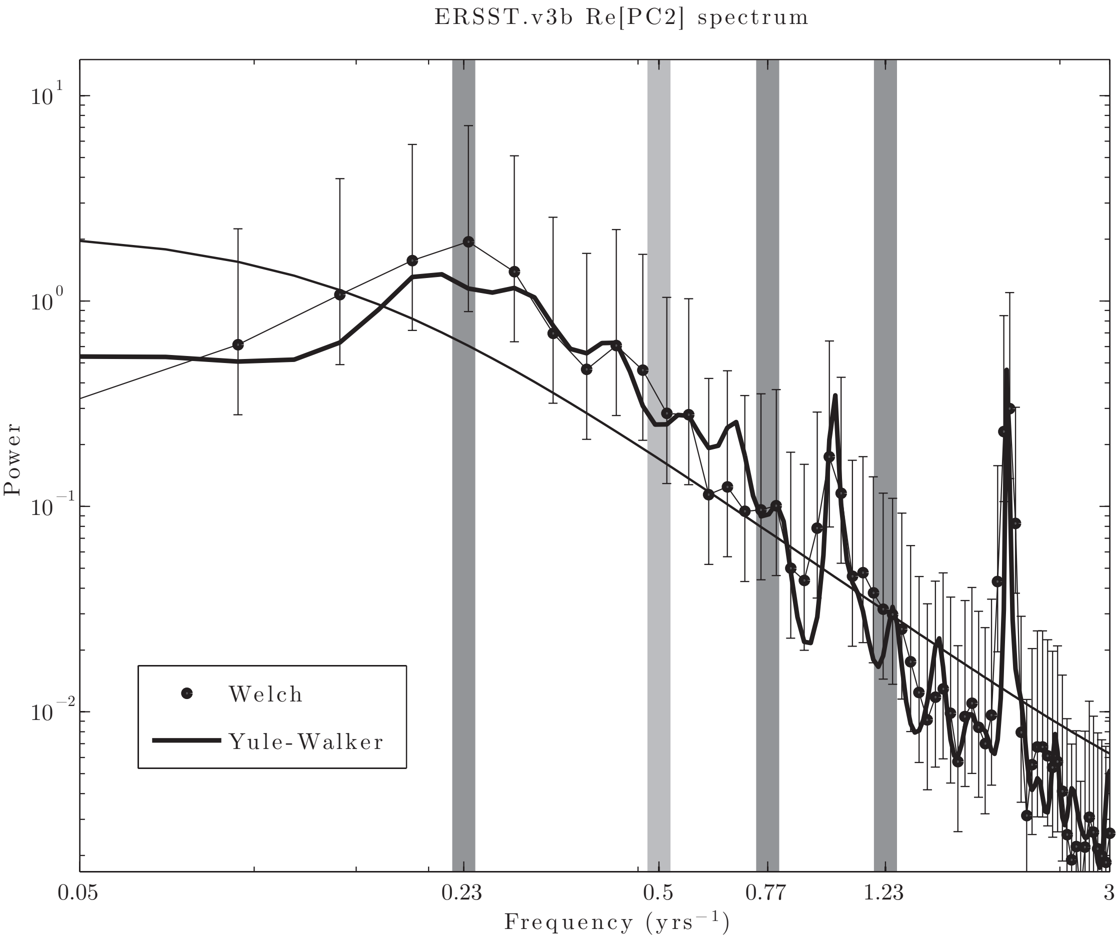

Figure 3.4: The spectrum of the real part of the ERSST.v3b CEOF PC2 time series, as calculated using the Yule-Walker (thick line) and Welch (dots) spectral estimation methods. The 95% confidence intervals of the Welch spectrum are indicated. The spectrum of a first order autoregressive model fit to the real part of PC2 is shown for comparison (thin line). The grey bars are located at the frequency of the primary ENSO peak, the biennial frequency, and $\omega_a \pm \omega_e$ combination tone frequencies.

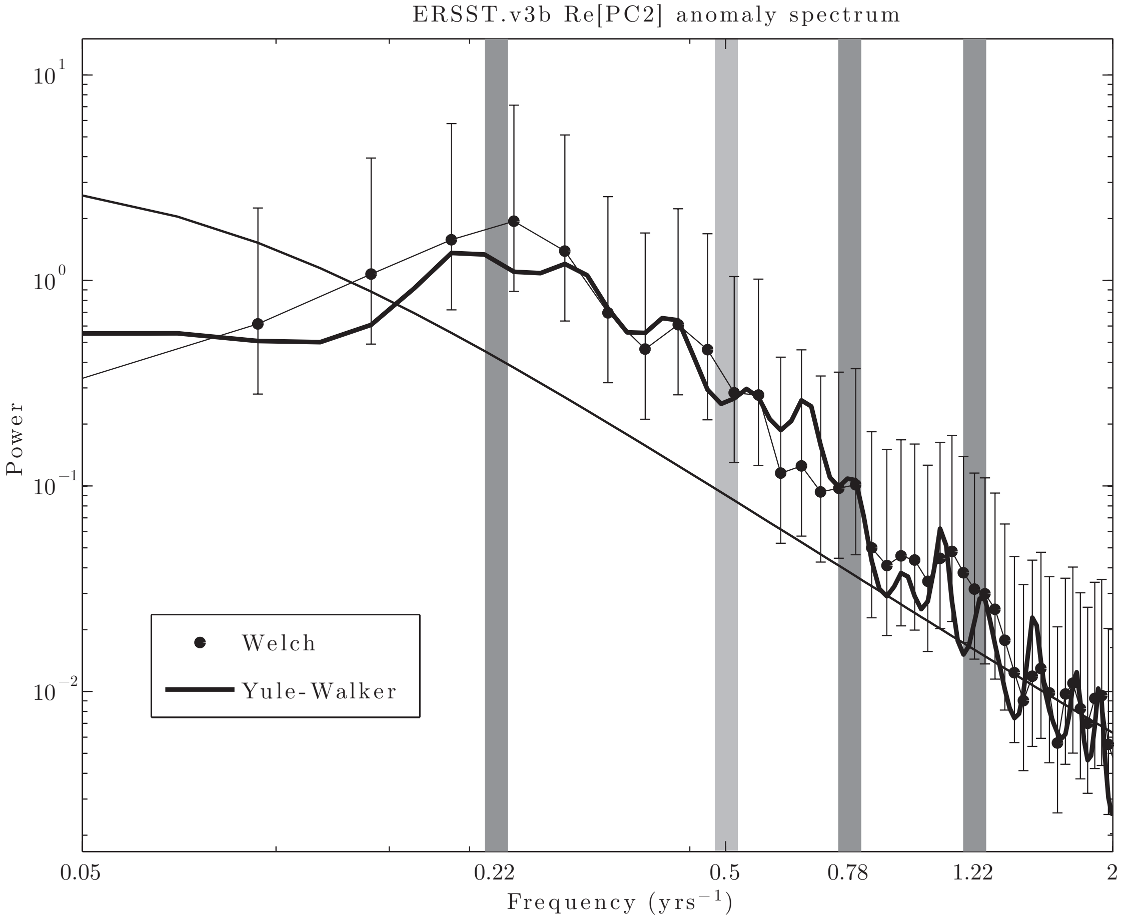

Figure 3.5: The spectrum of the real part of the ERSST.v3b CEOF PC2 time series with monthly means removed, as calculated using the Yule-Walker (thick line) and Welch (dots) spectral estimation methods. The 95% confidence intervals of the Welch spectrum are indicated. The spectrum of a first order autoregressive model fit to the real part of PC2 is shown for comparison (thin line). The grey bars are located at the frequency of the primary ENSO peak, the biennial frequency, and $\omega_a \pm \omega_e$ combination tone frequencies.

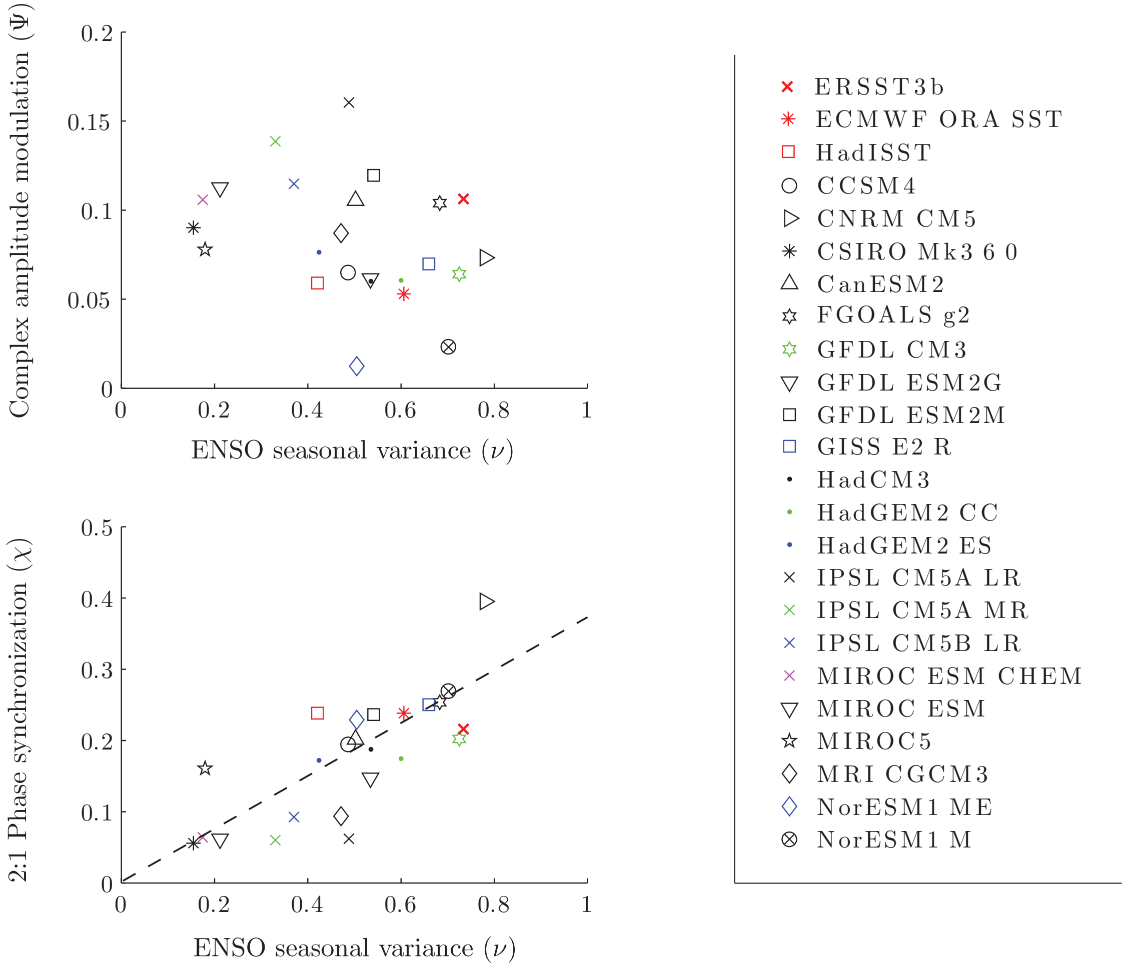

Figure 3.6: Scatter plots of the amplitude modulation index (Ψ,top) and the phase synchronization index (χ, bottom) versus the seasonal variance index (ν) based on the CEOF decomposition of equatorial Pacific SST observations, reanalyses, and model output from CGCMs participating in CMIP5. See text for the definitions of the synchronization indices.

Chapter 4

Analytical solutions of the parametric recharge oscillator

This chapter presents analytical solutions of the neutral, unforced version of the parametric recharge oscillator (PRO) model of ENSO, which is used as a framework to test the theory that ENSO synchronization arises due to the seasonal modulation of the coupled stability of the equatorial Pacific ocean-atmosphere system, or equivalently, the seasonal modulation of ENSO's growth rate. The PRO model is based upon the recharge oscillator model of ENSO (Jin, 1997) derived with seasonal varying coefficients (Stein et al., 2010), taking the form of a stochastic parametric oscillator

$$\frac{dT}{dt} = -\lambda(t)T + \omega(t)H + \xi(t) \tag{4.1}$$

$$\frac{dH}{dt} = -RT, \tag{4.2}$$

where T represents eastern equatorial Pacific sea surface temperature (SST) anomalies, H represents the zonal mean equatorial Pacific thermocline depth anomalies, $\lambda(t)$ and $\omega(t)$ are the seasonally varying growth rate and angular frequency parameters of the oscillator, the constant R relates to the time scale of the geostrophic adjustment of the thermocline to wind stress anomalies, and $\xi(t)$ is Gaussian white noise representing forcing by the atmosphere (Hasselmann, 1976). The parameters λ, ω can be derived from a statistical-dynamical estimation of the linearized upper ocean heat budget based on the Bjerknes index (Jin et al., 2006).

The model has been shown to reproduce the observed seasonal cycle of ENSO variance (Figure 4.1), based on fits of equations (4.1,4.2) to a hindcast performed with the Ocean GCM for the Earth Simulator (OFES), developed at the Japan Agency for Marine-Earth Science and Technology (JAMSTEC) (Masumoto et al., 2004). Time series for the eastern Pacific upper ocean temperature (T) and zonally averaged subsurface temperature (H) were calculated from the hindcast output, and the parameters in (4.1,4.2) were determined using a direct statistical of the equations ($\lambda(t)$) and from a statistical-dynamical fit ($I_{BJ}(t)$) based on the Bjerknes index (Jin et al., 2006). Models runs utilizing both the estimated growth parameters ($\lambda(t)$,$I_{BJ}(t)$) reproduced the seasonal cycle of ENSO variance in the hindcast (Figure 4.1). Modulation of the frequency parameter was shown to have little effect on the seasonal variance of ENSO (Stein et al., 2010), so the model can be further reduced to

$$\frac{dT}{dt} = -\lambda(t)T + \omega_e H + \xi(t) \tag{4.3}$$

$$\frac{dH}{dt} = -\omega_e T, \tag{4.4}$$

where where $\omega_e = \sqrt{\omega R}$. Equations (4.3,4.4) consitute the PRO model of ENSO.

An approximate analytical solution was obtained for the neutrally stable, unforced case of the PRO model, where $\xi(t) = 0$, $\lambda(t) = \lambda_0 \cos(\omega_a t)$, and ω_a is the annual frequency in (4.3). Setting $\lambda_0 = \epsilon, 0 < \epsilon << \omega_a$, and using the perturbation method, the first-order approximation to the solution for T can be obtained (An and Jin, 2011) as

$$T = C\left[\cos(\omega_e t) + \epsilon A \cos(\omega_a t)\sin(\omega_e t) - \epsilon B \sin(\omega_a t)\cos(\omega_e t)\right] + \mathcal{O}(\epsilon^2), \tag{4.5}$$

---

where C is a constant dependent on the initial conditions, $A = \frac{\omega_e}{\omega_a^2 - 4\omega_e^2}$, and $B = \frac{\omega_a^2 - 2\omega_e^2}{\omega_a^3 - 4\omega_e^2\omega_a}$. Without loss of generality, we can set $C = 1$. Note that due to the denominators of A and B, $T \to \infty$ as $\frac{\omega_a}{\omega_e} \to 2$, which reflects parametric resonance in the system. For all values of $\frac{\omega_a}{\omega_e} > 2$, the parameter B is larger than A, with the ratio of $\frac{B}{A} \approx 1.12 \times \frac{\omega_a}{\omega_e} - 1$ for realistic ENSO periods.

An example of the T and $\mathcal{H}[T]$ time series, seasonal variance, and amplitude and phase for equation (4.5) is show in Figure 4.2. For this example, the ENSO period was set to 3.75 years and the amplitude of the seasonal modulation was set to $\epsilon = 2$ years^{-1} in order to match the range of the observed monthly Nino3.4 SSTA index variance. Although there is an arbitrary phase shift in terms of the time of year that the modulation occurs, the equation can reproduce the salient aspects of ENSO seasonal synchronization. The ranges of the seasonal variance, amplitude modulation, and the PDF of the phase difference with the annual cycle agree well with the observations (Figure 2.1), especially considering the equation's simplicity. Utilizing equation (4.5), analytical solutions can be obtained for the Hilbert transform of T, as well as the seasonal variance and amplitude modulation of the T time series. Additionally, it can be shown that the ENSO signal expressed in equation (4.5) will have a preferred phase difference with the annual cycle. This analysis will demonstrate that the various aspects of ENSO synchronization results directly from the modulation of ENSO's growth rate by the annual cycle.

First, to calculate the seasonal variance of T, write the time series as the the cyclostationary process $T(y, m)$, with a monthly time series chosen for consistency with the observational data and coupled model output used in this study. The seasonal variance is then

$$
\begin{aligned}
\sigma_T^2(m) &= E\{T^2(y,m)\} \\
&= E\{\cos^2[\omega_e(y,m)] + \epsilon A\cos[\omega_a(y,m)]\sin[2\omega_e(y,m)] \\
&\quad -2\epsilon B\sin[\omega_a(y,m)]\cos^2[\omega_e(y,m)] \\
&\quad +\epsilon^2 A^2 cos^2[\omega_a(y,m)] sin^2[\omega_e(y,m)] + \epsilon^2 B^2 sin^2[\omega_a(y,m)] cos^2[\omega_e(y,m)] \\
&\quad -\epsilon^2\frac{AB}{2} sin[2\omega_a(y,m)] sin[2\omega_e(y,m)]\} + \mathcal{O}(\epsilon^3), \qquad (4.6)
\end{aligned}
$$

where E indicates the expected value and we have made use of the fact that $E\{T\} = 0$. For the relevant ENSO timescale, the A^2 term in (4.6) is negligible. With a long enough sampling time, the expected value of ω_e terms will be constant with respect to the annual cycle and we can set $E\left\{\cos^2[\omega_e(y,m)]\right\} = E\left\{\sin^2[\omega_e(y,m)]\right\} = \frac{1}{2}$ and $E\left\{\cos[2\omega_e(y,m)]\right\} = E\left\{\sin[2\omega_e(y,m)]\right\} = 0$, resulting in

$$
\sigma_T^2(m) \approx \frac{1 - 2\epsilon B\sin(\omega_a m) + \epsilon^2 B^2 sin^2(\omega_a m)}{2}. \qquad (4.7)
$$

Thus, the variance of ENSO will be periodic with respect to the annual cycle, with this periodicity arising from the second cross term between the annual cycle and ENSO in (4.5). The third term in equation (4.7) represents a semi-annual contribution to the seasonally modulated variance.

In order to calculate the Hilbert transform of the T time series, first note that equation (4.5) is equivalent to

$$
T = \cos(\omega_e t) - \epsilon\frac{B-A}{2}\sin[(\omega_a+\omega_e)t] - \epsilon\frac{A+B}{2}\sin[(\omega_a-\omega_e)t] + \mathcal{O}(\epsilon^2). \qquad (4.8)
$$

This form of the analytical solution shows explicitly that modulation of ENSO by the annual cycle will result in energy at the combination tone frequencies $\omega_a \pm \omega_e$ which account for the secondary peaks in the observed and modelled ENSO spectra. In particular, the approximate solution (4.8) explains the dependence of the frequencies of the secondary peaks on the mean ENSO frequency, and shows that $\omega_a - \omega_e$ component of the time series will be more larger than the $\omega_a + \omega_e$ component. Both of these characteristics are apparent in the observed Nino3.4 SSTA spectrum (Fig. 2.2).

We then utilize the fact that the Hilbert transform is a linear operator, and that the Hilbert transform of the cosine and sine functions are known, namely $\mathcal{H}[\cos(x)] = \sin(x)$ and $\mathcal{H}[\sin(x)] = -\cos(x)$. The Hilbert transform of T is then

$$\begin{aligned} \mathcal{H}[T] &= \sin(\omega_e t) + \epsilon\frac{B-A}{2}\cos[(\omega_a+\omega_e)t] + \epsilon\frac{A+B}{2}\cos[(\omega_a-\omega_e)t] + \mathcal{O}(\epsilon^2) \\ &= \sin(\omega_e t) + \epsilon A\sin(\omega_a t)\sin(\omega_e t) + \epsilon B\cos(\omega_a t)\cos(\omega_e t) + \mathcal{O}(\epsilon^2). \end{aligned} \tag{4.9}$$

The seasonal variance of the Hilbert transform of T can also be calculated as it was for the T time series itself,

$$\sigma^2_{\mathcal{H}}(m) \approx \frac{1 + 2\epsilon A\sin(\omega_a m) + \epsilon^2 B^2 cos^2(\omega_a m)}{2}. \tag{4.10}$$

This periodic variance of the T and $\mathcal{H}[T]$ time series are related to the seasonal amplitude modulation. The amplitude of the analytical signal of T is defined as

$$\alpha(t) = \sqrt{T^2 + \mathcal{H}[T]^2}, \tag{4.11}$$

and the seasonal amplitude modulation is defined by taking the cyclostationary mean of the amplitude, namely

$$\begin{aligned} E\{\alpha(y,m)\} &= E\{\sqrt{T^2(y,m) + \mathcal{H}[T]^2(y,m)}\} \\ &\approx \sqrt{1 + \epsilon[A-B]\sin(\omega_a m)}. \end{aligned} \tag{4.12}$$

which can be solved readily to first order using equations (4.5) and (4.9). Because the complex amplitude modulation is proportional to the difference of the A and B parameters, the effect is relatively small.

Additionally, the modulation of the growth parameter in (4.3) results in a preferred phase difference between ENSO and the annual cycle. The result may seem counter-intuitive, but the reason that modulation of the growth rate parameter in the PRO model can lead to phase synchronization is that the modulation of the growth parameter occurs on a shorter timescale than the intrinsic ENSO period. This is in contrast to a standard amplitude modulated (AM) signal, in which the modulation occurs at a much lower frequency than the carrier signal, and therefore no phase synchronization can result.

The phase of ENSO is defined as

$$\begin{aligned} \phi_e(t) &= \operatorname{Arg}\left\{\frac{\mathcal{H}[T]}{T}\right\} && (4.13)\\ &= 2\arctan\left\{\frac{\mathcal{H}[T]}{\sqrt{T^2+\mathcal{H}[T]^2}+T}\right\}, && (4.14)\end{aligned}$$

where the tangent half-angle formula is used to calculated the principle value of the argument in a uniform matter. Neglecting the A terms yields

$$\phi_e(t) \approx 2\arctan\left\{\frac{\sin(\omega_e t)+\epsilon B\cos(\omega_a t)\cos(\omega_e t)}{\alpha(t)+\cos(\omega_e t)-\epsilon B\sin(\omega_a t)\cos(\omega_e t)}\right\}, \tag{4.15}$$

which is form of the solution that was used for calculating the analytical phase difference $\delta\phi_{2,1}$ in Figures 4.2, 5.1, & 5.2. However, a simplified version of the equation is more helpful in demonstrating conceptually the relationship between ENSO seasonal variance and phase synchronization with the annual cycle. As shown before, the seasonal amplitude modulation is small, so the value of $\alpha(t)$ can be fixed at 1. Neglecting the ϵ term in the numerator then yields

$$\phi_e(t) \approx 2\arctan\left\{\frac{\sin(\omega_e(t)}{1+\cos(\omega_e t) - \epsilon B \sin(\omega_a t)\cos(\omega_e(t)}\right\}. \tag{4.16}$$

Solving equation (4.7) for ϵB and inserting the solution into equation (4.16) results in a solution for ENSO phase modulation in terms of the seasonal variance:

$$\phi_e(t) \quad \approx \quad \arctan\left\{\frac{\sin(\omega_e(t)}{1+\sqrt{2}\sigma_T \cos(\omega_e t)}\right\}, \tag{4.17}$$

where we have made use of the fact that $\sin(\omega_a t) = \sin(\omega_a m)$ by definition.

With no modulation, the phase of ENSO would proceed monotonically as expected, $\phi_e(t) = \omega_e t$. The stronger the modulation of the growth rate parameter (ϵ), the stronger the seasonal modulation of ENSO variance (4.7), and therefore the stronger the modulation of the ENSO phase progression (4.17) which leads to the phase synchronization with the annual cycle. Equation (4.17) thus explains linear relationship between ENSO seasonal variance and the strength of the phase synchronization with the annual cycle that occurs across CMIP5 models and observations (Figure 2.6). The annual cycle modulation has the largest effect when $\cos(\omega_e t)$, and therefore the value of T, is near an extrema. In other words, the phase synchronization of ENSO to the annual cycle occurs in the PRO model through the modulation of the ENSO progression near the peak of El Niño and La Niña events.

The analysis of the PRO model shows that the annual modulation of the growth rate parameter can account for all the observed features of ENSO synchronization: seasonal variance, amplitude modulation, phase synchronization, and combination tones in the ENSO spectrum. The secondary spectral peaks at combination tones between ENSO and the annual cycle result directly from the modulation of ENSO's growth rate by the annual cycle, and are seen explicitly in the first order solution to the system (4.8). Analytical solutions for the seasonal variance (4.7) , amplitude modulation (4.12), and phase synchronization (4.15) of ENSO are also obtainable, with low-order forms of the solutions agreeing well with the statistical analysis (Figure 4.2). Simplified equations (4.16,4.17) for ENSO phase capture the essential mechanism that produces the preferred 2:1 phase difference with the annual cycle, and explicitly relates ENSO's phase synchronization to its seasonal variance. The counter-intuitive result that modulation of the growth parameter can result in a preferred phase difference is due to the fact that the modulation of ENSO occurs at a higher frequency than ENSO itself. In such a system, amplitude modulation and phase synchronization are not independent, but result directly from the annual cycle modulation, and are dependent on the two free parameters of the system: the strength of the modulation (ϵ), and ENSO's intrinsic frequency (ω_e). In the next section, the simplified analytical equations are shown to apply to more realistic numerical runs of the PRO model, supporting the proposition that the equations capture the salient features of ENSO synchronization in the natural system.

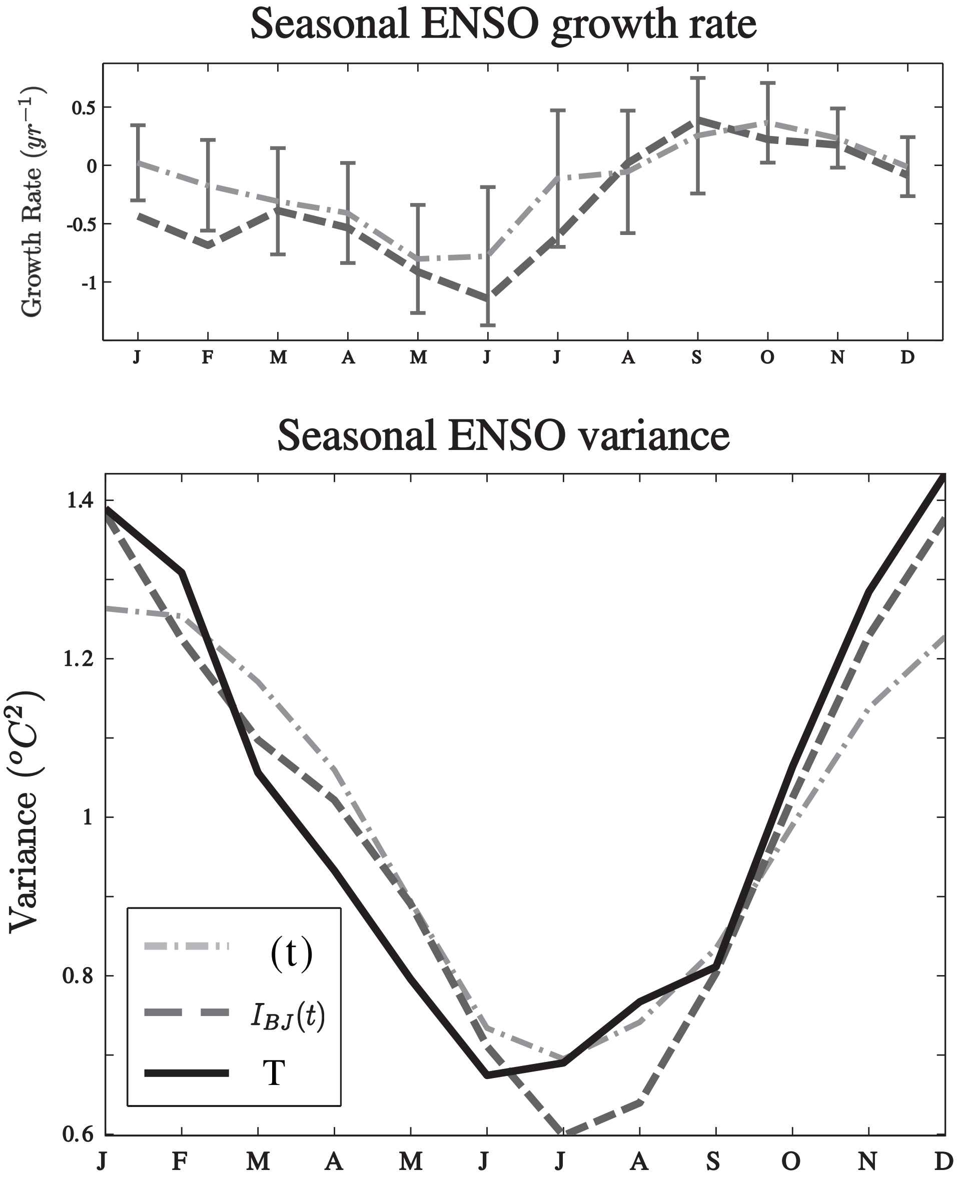

Figure 4.1: (Top) The growth rate of ENSO in OFES, estimated from a stastical fit of equation (4.1) (dash-dot), and from a statistical-dynamical fit (dashed) based on the Bjerknes index (Jin et al., 2006). (Bottom) The seasonal variance of eastern Pacific upper ocean temperature (T) in OFES (solid) compared to model runs of (4.1,4.2) utilizing the growth rate $\lambda(t)$ determined from a statistical (dash-dot) and a statistical-dynamical (dash) fit. Figure reproduced from Stein et al. (2010).

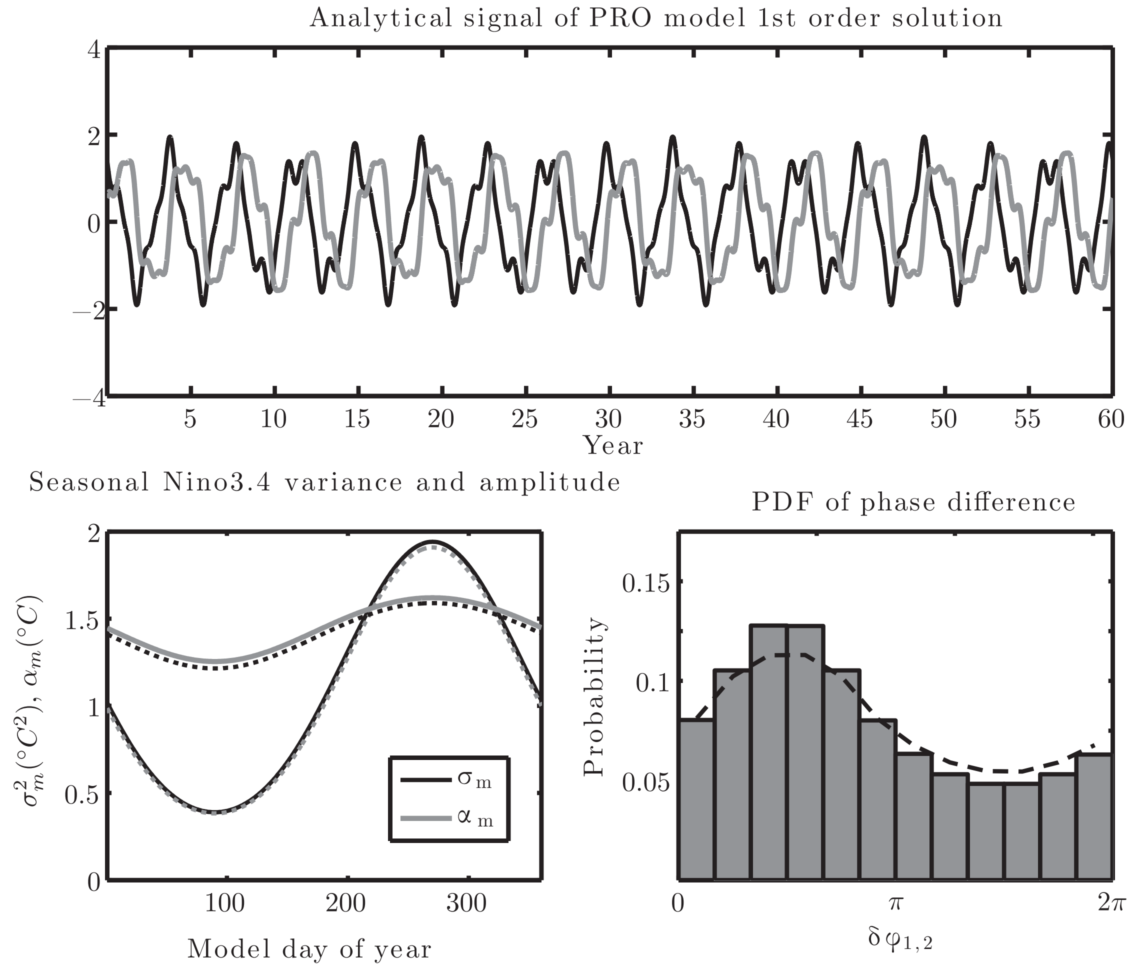

Figure 4.2: (Top) The T time series and the Hilbert transform of the time series, based on the analytical solution of the neutral PRO model (equation 4.5). (Bottom left) The monthly variance of the T time series and the monthly amplitude of the analytical signal of the time series. (Bottom right) A PDF of the $\delta\phi_{2,1}$ phase difference of ENSO with the annual cycle. The analytical solutions of the seasonal variance, seasonal amplitude, and phase difference are indicated by dashed lines.

Chapter 5

Numerical confirmation of the analytical solutions

The analytical results presented in the preceding section were based on a solution (4.5) obtained via a first-order perturbation expansion to a particular case of the PRO model, namely the neutrally stable system with no stochastic forcing. Three assumptions were made to obtain this solution: 1) no forcing of the system, 2) neutral stability, i.e. zero mean growth rate, 3) relatively small modulation of the growth/damping rate, specifically $0 < \epsilon << \omega_a$. However, it is not possible to obtain realistic model oscillations given these assumptions. Moreover, the approximate solutions obtained for ENSO seasonal variance (4.7), amplitude modulation (4.12), and phase (4.15), were obtained by neglecting some higher order terms. It is therefore uncertain whether the approximate solutions have any relevance to the observations. To test the validity of the solutions, they were compared to output from numerical runs of the full PRO model (4.3,4.4). For both experiments, the ENSO period was set to 3.75 years, a daily timestep was used, and monthly averages of the T time series were saved as output. For simplicity, the model year consists of 360 days, 12 months of 30 days each.

In order to reproduce the observed range of ENSO seasonal variance, the amplitude of the modulation of the growth rate (λ) for the numerical runs was set to $\epsilon = 2$ years^{-1}. This value is much large than was assumed by the perturbation method, so it is necessary to test whether the analytical solutions are still applicable to the case of the neutral, undamped PRO model. To do so, the analytical solutions were compared to output from a 60 year integration of equations (4.3,4.4) with $\xi(t) = 0$, $\lambda(t) = \epsilon \cos(\omega_a t)$, $\epsilon = 2$ years^{-1}. The neutral PRO model was initialized with values of $T = 0$, $H = 1.35$, resulting in a variance for the T time series of $1.029°C$. Figure 5.1, shows the T and $\mathcal{H}[T]$ time series, the seasonal variance of the T time series, the amplitude modulation of the analytical signal, and a histogram of the $\delta\phi_{2,1}$ phase difference between the complex analytical signal $\widehat{T}$ and the annual cycle from the neutral PRO model run. Analytical solutions for the seasonal variance, amplitude modulation, and phase difference are shown with dashed lines for comparison. The numerical and analytical solutions for the T time series agree well, and the analytical solutions of the amplitude modulation, seasonal variance, and phase difference are very good approximations to the values computed statistically from the T time series from the numerical integration. The analytical solutions (4.5,4.7,4.12,4.15) therefore apply to the neutral PRO model, despite the violation of the assumption of a small modulation (ϵ) of the damping rate (λ) used in the perturbation expansion and the further simplifications made in obtaining the approximate synchronization solutions.

Next, the analytical solutions were compared to the more realistic case of the damped, stochastically forced PRO model. For these model runs, the damping parameter was set to $\lambda(t) = \overline{\lambda} + \epsilon \cos(\omega_a t)$, with the mean damping rate set to $\overline{\lambda} = 0.4$ years^{-1} based upon the fit of the PRO model to output from the OFES hindcast (Stein et al. (2010), see Chapter 4). Gaussian stochastic noise with a variance of $0.04°C$ was applied at each time step of one model day. Figure 5.2 shows the synchronization statistics from an 100 member ensemble of 150 year runs of the stochastically forced model, with an example of the time series output above. For each ensemble member, the model was run for 200 years, with the last 150 years of output used for analysis. The ensemble mean monthly variance, monthly amplitude, and $\delta\phi_{2,1}$ phase differences are shown, along with the 90% confidence intervals for each statistic. Though the time series of model output for the two cases are quite different, the ensemble mean statistics of the stochastic case are very similar to the damped, unforced case and agree with the analytical estimates. Thus, the analytical solutions obtained for the neutral, unforced case of the PRO model are valid for the long-term behavior of the damped, stochastically forced case. However, the stochastic forcing adds a large degree of uncertainty about the statistics of a particular ensemble member. Notably, the seasonal variance and preferred phase difference that result from the annual cycle modulation will be apparent for each ensemble member, while the same cannot be said for the amplitude modulation, which is characterized by a very small signal-to-noise ratio for the stochastically forced case. For time series of ≤ 150 years, the stochastic forcing may mask the underlying amplitude modulation, but the seasonal variance and preferred phase difference that result from the annual modulation of ENSO will still be apparent. These results explain the weak correspondence between seasonal variance and amplitude modulation across the CMIP5 models (Figure 2.6), as reflected in equation 4.12.

The analytical solutions presented in the previous section thus capture the essential aspects of ENSO synchronization in the PRO model for both the neutral case and for the forced, damped case with realistic mean damping rate. We can therefore examine the dependence of ENSO synchronization statistics on the degree of annual cycle modulation and intrinsic ENSO frequency using equation (4.5). Figure 5.3 shows contours of the three synchronization indices across a section of the PRO model parameter space. For ENSO modes with periods longer than three years, the index contours are nearly horizontal, indicating that the strength of all the synchronization indices is determined almost entirely by the strength of the annual cycle modulation. In this regime, ENSO seasonal variance, amplitude modulation, and phase synchronization increase nearly monotonically with increasing modulation of the growth rate parameter. Model ENSOs with a period less than three years move toward a regime where increased modulation of the growth rate parameter results in increased seasonal ENSO variance and phase synchronization, but not an increase in amplitude modulation of the complex analytical signal. In this regime, the model becomes parametrically destabilized, and nonlinear saturation is necessary to limit overall ENSO variance.

Using Figure 5.3, one can predict the strength of phase synchronization of ENSO to the annual cycle, given the mean ENSO period and seasonal variance, which provide an estimate of the strength of the annual cycle modulation, i.e. the range of $\lambda(t)$.

This calculation was done for the observations and the CMIP5 model ENSOs, using the ν index to derive the strength of the seasonal variance and defining the mean ENSO frequency using the unwrapped phase times series:

$$\omega_e = \left\langle \frac{d\phi_e}{dt} \right\rangle_t .$$

An estimate of the strength of the modulation by the annual cycle based on the analytical solution to the PRO model can be obtained using ν and ω_e (Figure 5.3, top), and the values of ω_e and ν then correspond to a predicted phase synchronization strength χ (Figure 5.3, center). The predicted and measured strengths of the 2:1 phase synchronization are compared in Figure 5.4. The two values agree well, with the value predicted by the analytical PRO model accounting for 75% of the variance in the strength of the phase synchronization in the CMIP5 models. The agreement indicates that the measured 2:1 phase synchronization arises from the modulation of ENSO's growth rate by the annual cycle, and provides further evidence that the analytical solutions of the PRO model capture the essential features of ENSO synchronization in the observations and CMIP5 models.

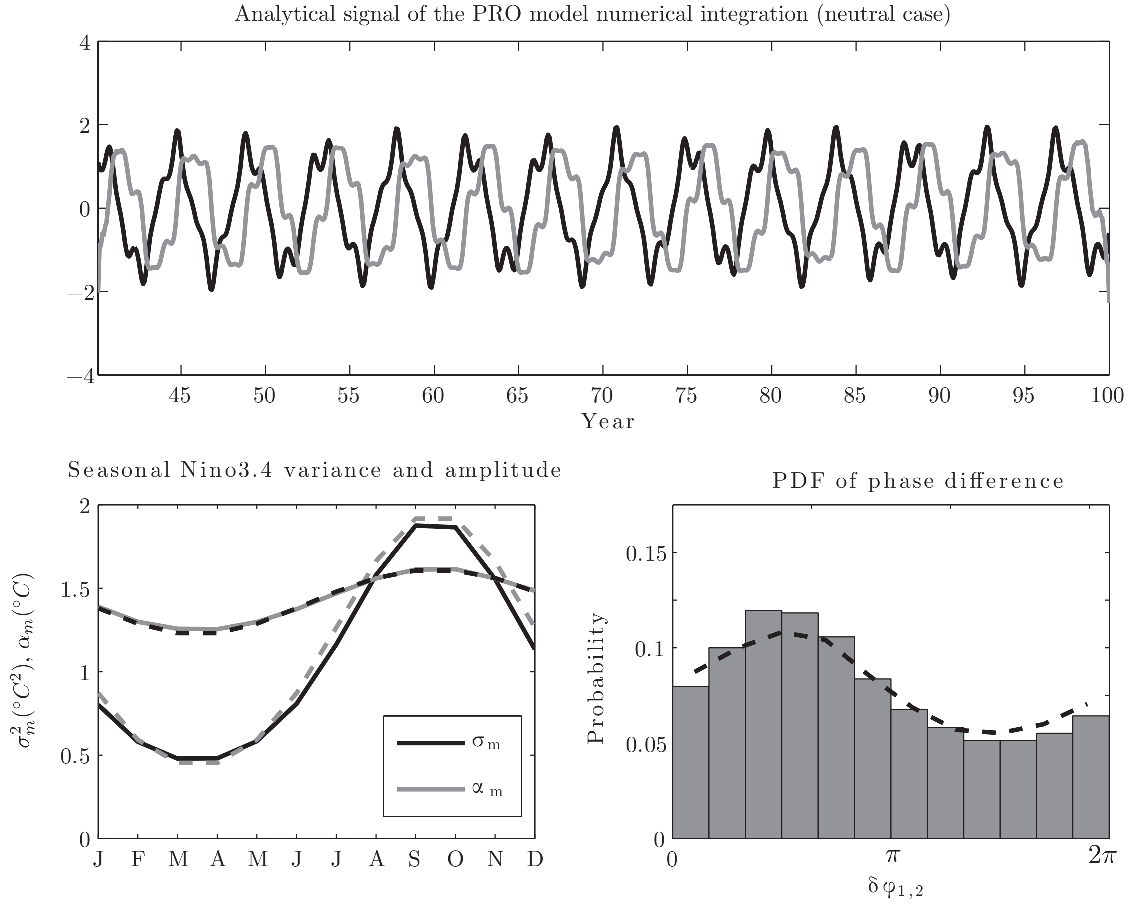

Figure 5.1: (Top) The T time series and the Hilbert transform of the time series, based on a numerical integration of the a neutral PRO model. (Bottom left) The monthly variance of the T time series and the monthly amplitude of the analytical signal of the time series. (Bottom right) A PDF of the $\delta\phi_{2,1}$ phase difference of ENSO with the annual cycle. The analytical solutions of the seasonal variance, seasonal amplitude, and phase difference are indicated by dashed lines.

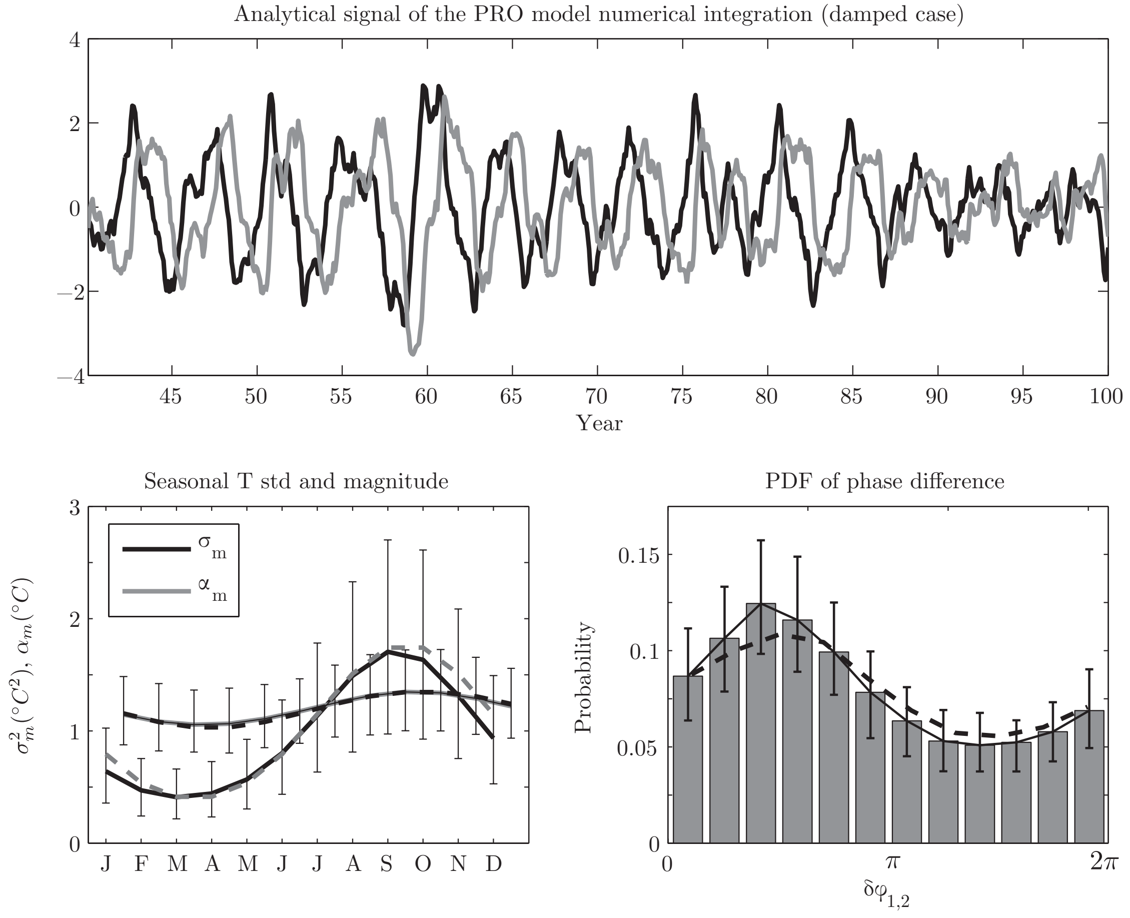

Figure 5.2: (Top) An example of the T time series and the Hilbert transform of the time series, from a single member of an ensemble of integrations of the a damped, stochastically forced PRO model. (Bottom left) The ensemble mean monthly variance of the T time series and the ensemble mean monthly amplitude of the analytical signal of the time series. (Bottom right) A PDF of the $\delta\phi_{2,1}$ phase difference of ENSO with the annual cycle. 90% confidence intervals for the seasonal variance, amplitude modulation, and PDF of the phase difference, based on the 100 member ensemble, are shown. The analytical solutions of the seasonal variance, seasonal amplitude, and phase difference are indicated by dashed lines.

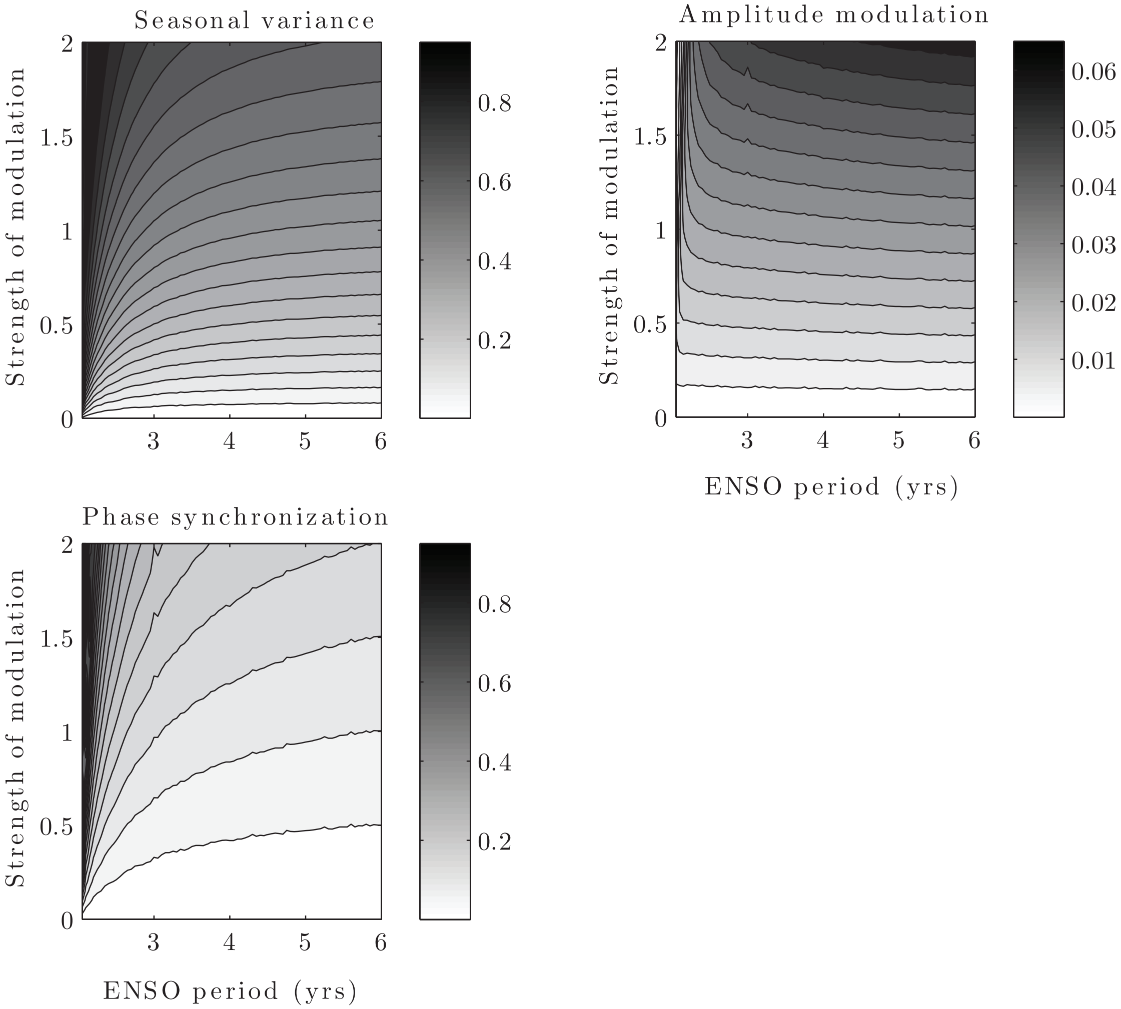

Figure 5.3: Contours of the seasonal variance index (ν, top), the amplitude modulation index (Ψ, middle), and the phase synchronization index (χ, bottom) of the analytical solution of the PRO model (equation 4.5) within the model parameter space defined by the intrinsic ENSO period and the strength of the annual cycle modulation. See text for the definitions of the synchronization indices.

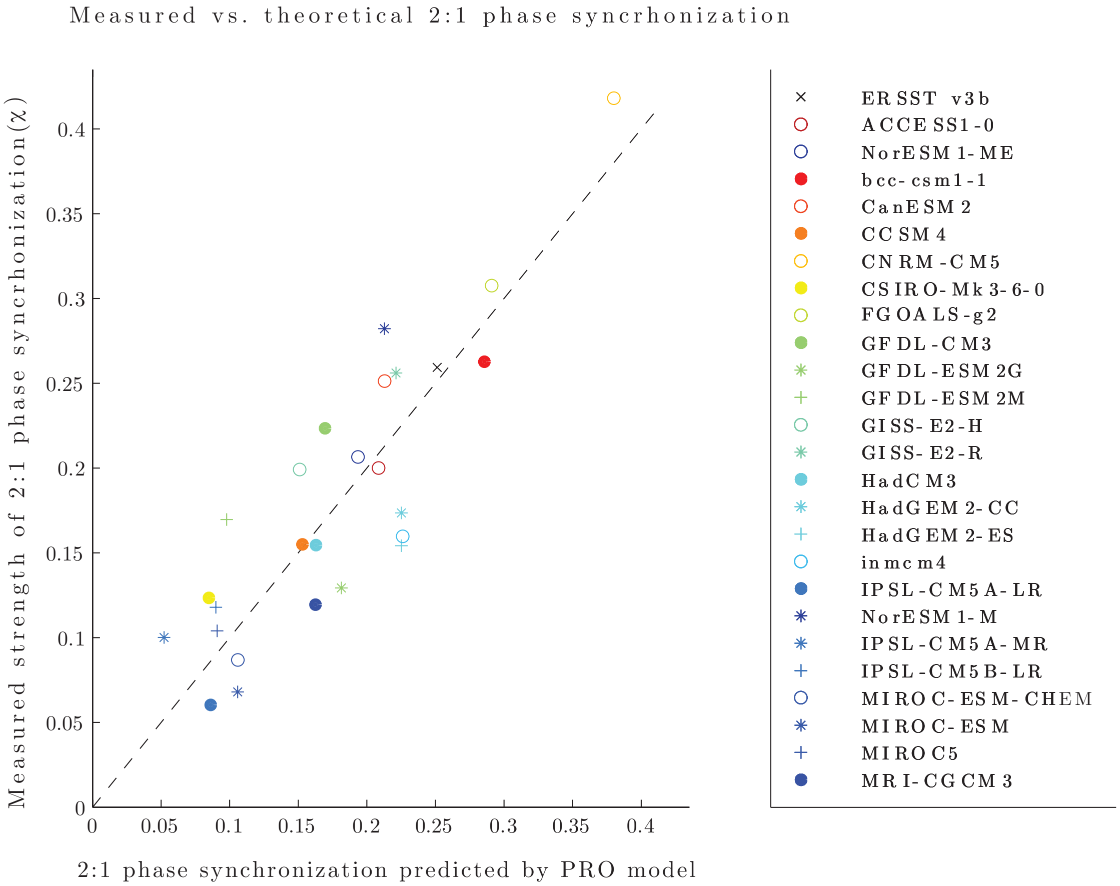

Figure 5.4: The strength of the 2:1 phase synchronization (χ) in the observations and CMIP5 coupled GCMs versus the amount predicted based on analytical solutions of the PRO model (figure 5.3).

Chapter 6

ENSO synchronization through frequency locking

In order to compare the above results to the frequency locking scenario for ENSO, equations (4.1,4.2) are extended to include periodic forcing and a nonlinear damping term. The damping rate λ is held constant with respect to the annual cycle, and the behavior of the model is examined in the unstable regime above the Hopf bifurcation at $\lambda = 0$. The extended model is not offered as a particularly realistic representation of ENSO, but rather as a system that has similar global behavior to the simple (Tziperman et al., 1994; Wang and Fang, 1996; Liu, 2001) and intermediate (Chang et al., 1994; Tziperman et al., 1995; Jin et al., 1996) models of ENSO on which the frequency locking scenario is based, and which admits the same suite of possible model solutions.

The extended model reads:

$$\begin{aligned} \frac{dT}{dt} &= \lambda T + \omega_e H - cT^3 + F \sin(\omega_a t) && (6.1) \\ \frac{dH}{dt} &= -\omega_e T, && (6.2) \end{aligned}$$

where the sinusoidal forcing term represents external forcing by the annual cycle that is independent of eastern Pacific SST anomalies (Liu, 2001) and the cubic damping term represents nonlinear saturation of SST anomalies due to e.g. the nonlinear dependence of subsurface temperature on thermocline depth (Jin, 1997).

Equations (6.1,6.2) can be reduced to the well-known forced van der Pol oscillator (van der Pol, 1927) with two simplifications. First, rescale the equations by $\tau = \omega_e t$, and second, fix the strength of the cubic damping to $c = \frac{\lambda}{3}$, resulting in:

$$\frac{d^2T}{d\tau^2} - \widehat{\lambda}(1 - T^2)\frac{dT}{d\tau} + T = \widehat{\omega}\widehat{F}\cos(\widehat{\omega}\tau), \tag{6.3}$$

where $\widehat{\omega} = \frac{\omega_a}{\omega_e}$, $\widehat{c} = \frac{c}{\omega_e}$, $\widehat{F} = \frac{F}{\omega_e}$, and $\widehat{\lambda} = \frac{\lambda}{\omega_e}$. By setting $\widehat{c} = \frac{\widehat{\lambda}}{3}$, the growth rate and cubic damping terms have been combined into the nonlinear damping term $\widehat{\lambda}$, which also controls the intrinsic frequency of the unforced oscillation. The periodically forced van der Pol oscillator (6.3) has been thoroughly studied (see Mettin et al. (1993) for a complete description of the bifurcation structure), so we will limit our discussion here to the types of solutions that are allowed by the system and their applicability to the seasonal synchronization of ENSO. We begin by providing examples of each type of model solution, using a value of $\widehat{\omega} = 4.02$ years^{-1} because of the known chaotic solutions at that driving frequency (Mettin et al., 1993), and then proceed to examine the solutions that occur within the parameter space relevant to ENSO.

In the absence of external forcing, the solution of the self-sustained oscillator ($\widehat{\lambda} > 0$) follows a stable limit cycle with an amplitude of 2°C (Figure 6.1, A), which is comparable to the amplitude of the Nino3.4 index (Figure 2.1, top), so the choice to fix the value of the cubic damping parameter is reasonable. As the nonlinear damping parameter ($\widehat{\lambda}$) becomes larger, the period of oscillation increases and the system moves toward a relaxation oscillation (Figure 6.1, B). With the inclusion of periodic forcing, quasiperiodic solutions exist for relatively small values of the nonlinear damping (Figure 6.1, C). Further increasing the nonlinearity results in the oscillator becoming frequency locked to a rational multiple of the driving frequency (Figure 6.1, D). With strong enough nonlinear damping and forcing, chaotic oscillations can occur when several frequency locked solutions overlap, and the oscillation jumps irregularly between the possible resonant frequencies (Figure 6.1, E). The chaotic solutions observed in the driven van der Pol oscillator result from period doubling bifurcations (Mettin et al., 1993), a subcase of the quasiperiodic route to chaos (Jin et al., 1996) followed by ENSO models used in previous studies.

To examine the model solutions within a realistic parameter range, we fix the value of the forcing F in (6.1), and then examine model solutions with various values of the growth rate λ and neutral ENSO period $T_e = \frac{2\pi}{\omega_e}$. The range of the annual cycle of the Niño3.4 index provides reasonable upper limit of $1.2°C$ for the annual cycle forcing F in (6.1) (Liu, 2001). The neutral ENSO period T_e is varied from 2 to 5 years, and the λ parameter is varied from 0 to 6, corresponding to a maximum growth rate of $3°C$ per year. The annual cycle frequency is fixed at $\omega_a = 2\pi$, hence the driving frequency $\widehat{\omega} = \frac{\omega_a}{\omega_e}$ is equal to the mean ENSO period T_e.

Figure 6.2 displays contours of the ratio of the frequency of the T time series output from (6.3) to the driving frequency $\widehat{\omega}$, based on runs with rescaled parameters $\widehat{F}$, $\widehat{\omega}$, and $\widehat{\lambda}$ calculated from F, λ, and ω_e. Regions of quasiperiodic solutions are separated by frequency locked solutions that occur within "Arnol'd tongues" (Arnold et al., 1983), which become larger with increasing growth rate, and hence nonlinear damping $\widehat{\lambda}$. The Arnol'd tongues slope up and to the left because the shorter the neutral ENSO period T_e, the weaker the effective forcing $\widehat{\omega}\widehat{F}$ for a fixed F and ω_a. As can be seen, the driven van der Pol oscillator favors frequency locked solutions at odd multiples of the driving frequency; frequency locked solutions at even multiples of the driving frequency are very unstable (Mettin et al., 1993). No chaotic solutions were found in the neighborhood of realistic parameter ranges, reflecting the rarity of chaotic solutions within more complex ENSO models (Jin et al., 1996). We will therefore only compare the observed ENSO synchronization characteristics to the probable model solutions: quasiperiodic oscillations, frequency locked oscillations, and frequency locked oscillations with added stochastic forcing. However, chaotic solutions were shown to retain the subharmonic peaks associate with frequency locked solutions, so the analysis of the frequency locked solutions applies to the chaotic solutions as well.

Figure 6.3 shows an example of a quasiperiodic oscillation (top) obtained by setting $T_e = 2.76$ and $\lambda = 0.5$, along with the corresponding spectrum (bottom left). The strength of the $k : l$ phase synchronization between the T time series and the periodic forcing for $k, l \in [1, 10]$ is shown at the bottom right, defined as

$$\chi_{k,l} = \left| \left\langle e^{i(k\phi_e - l\phi_e)} \right\rangle_t \right| . \tag{6.4}$$

For a quasiperiodic solution, the ENSO frequency is still largely determined by the nonlinear damping rate ($\widehat{\lambda}$), independent of the forcing frequency, so the oscillation will not have a seasonal cycle of variance or display any phase synchronization with the periodic forcing (Figure 6.3, bottom right). Quasiperiodic solutions therefore produce no synchronization between ENSO and the annual cycle.

Increasing the growth rate to $\lambda = 2$ moves the system into the 3:1 Arnol'd tongue (Figure 6.2), resulting in a regular 3 year ENSO as shown in the spectrum (Figure 6.4, bottom left). Such subharmonic frequency locking will by definition produce phase synchronization as well, which can be seen most strongly at $3 : 1$, but also at the other $3n : n$ ratios (Figure 6.4, bottom right). The weaker phase synchronization at other ratios result from the fact that the oscillation is not perfectly sinusoidal. The frequency locked oscillation is far more regular than the observed ENSO, so stochastic forcing is necessary to make the solution more realistic (Figure 6.5). The inclusion of the stochastic forcing broadens the spectrum of the T output, and weakens the phase synchronization between the T time series and the periodic forcing, particular for larger values of k, l. The only remaining phase synchronization occurs at the ratio $3 : 1$, associated with the peak in the spectrum at the 3 year period.

To examine the possibility that the observed ENSO results from a stochastically perturbed frequency locked oscillation, we compared the above synchronization characteristics to those of the observations. Figure 6.6 shows the phase synchronization indices for $k, l \in [1, 10]$ as calculated from the observed Niño3.4 index. As mentioned before, the 2:1 phase synchronization is by far the strongest in the observations, and there is no indication of particularly strong synchronization at any other ratio. However, the 2 : 1 phase synchronization is not accompanied by a peak at the biennial frequency in the observed Nino3.4 SSTA spectrum (Figure 2.2), as would be the case if the phase synchronization was due to frequency locking. Similarly, the annual cycle and ENSO as simulated by the CMIP5 GCMs only display phase synchronization at the 2:1 ratio (Fig. 6.7). Though some CMIP5 models (CNRM-CM5, FGOALS-g2, CanESM2, Giss-E2-R) show a significant spectral peak at the biennial frequency, each of those models, and a majority of the others, have significant spectral peaks at combination tones in agreement with the analytical PRO model solution (4.8). This observation, combined with the ability of the PRO model to reproduce seasonal ENSO variance, amplitude modulation, and phase synchronization, suggests that the seasonal synchronization of ENSO is far more likely due to the periodic modulation of ENSO's growth rate by the annual cycle, rather than frequency locking of ENSO to periodic forcing by the annual cycle.

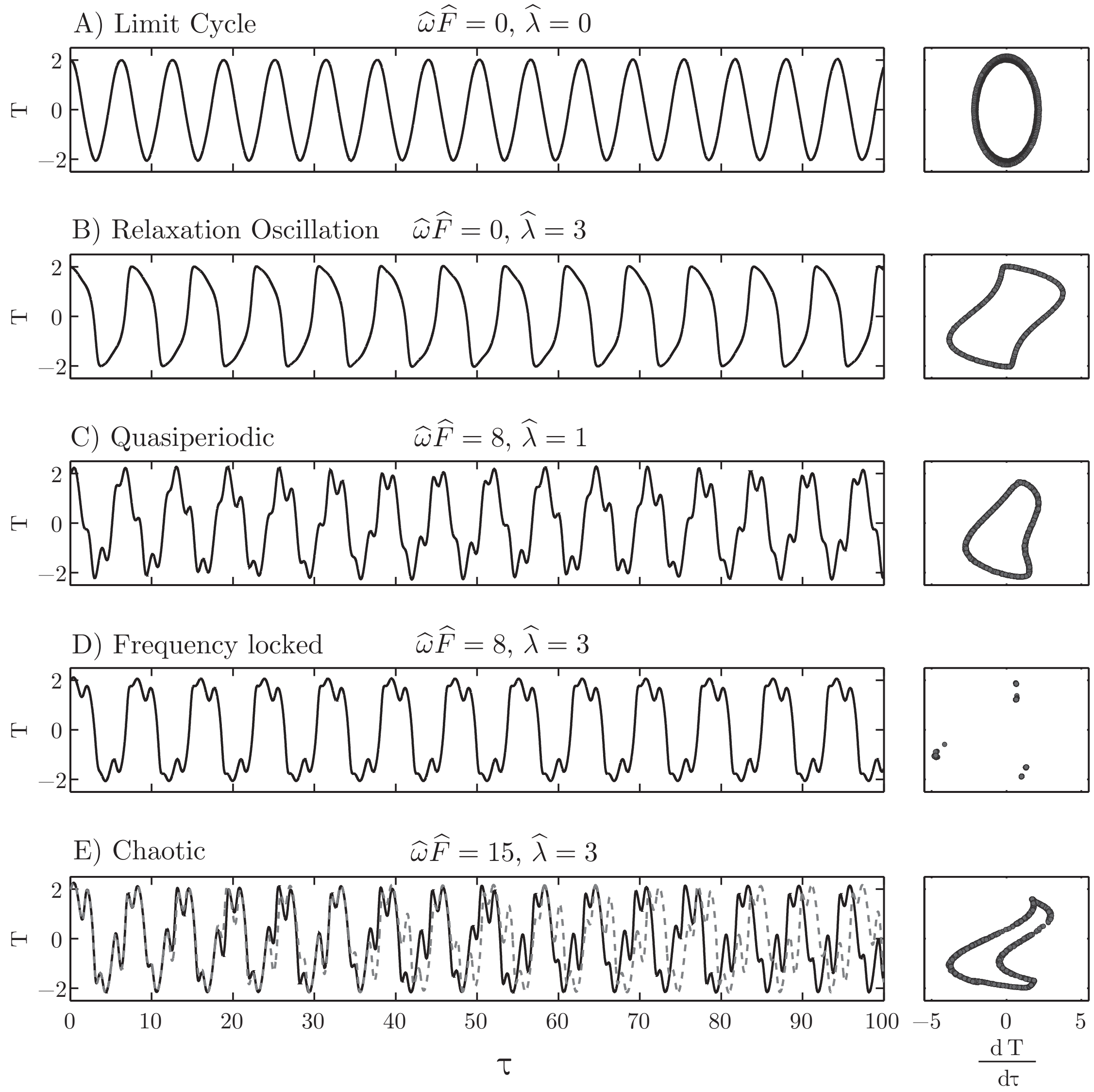

Figure 6.1: Time series from numerical integrations of van der Pol oscillator (6.3) for various values of the forcing amplitude ($\widehat{\omega}\widehat{F}$) and nonlinear damping ($\widehat{\lambda}$). For all time series, the driving frequency of the oscillator was set to $\widehat{\omega} = 4.02$ and initialized at $T = 2, \frac{dT}{d\tau} = 0$. From top to bottom, the time series represent a limit cycle, a relaxation oscillator, a quasiperiodic oscillation, a frequency locked oscillation, and a chaotic oscillation. The bottom plot shows the divergence of a time series initialized at $T = 2.01, \frac{dT}{d\tau} = 0$ (dashed). At the right, Poincaré sections of each time series for values of the annual cycle phase $\phi_a = 2\pi N$.

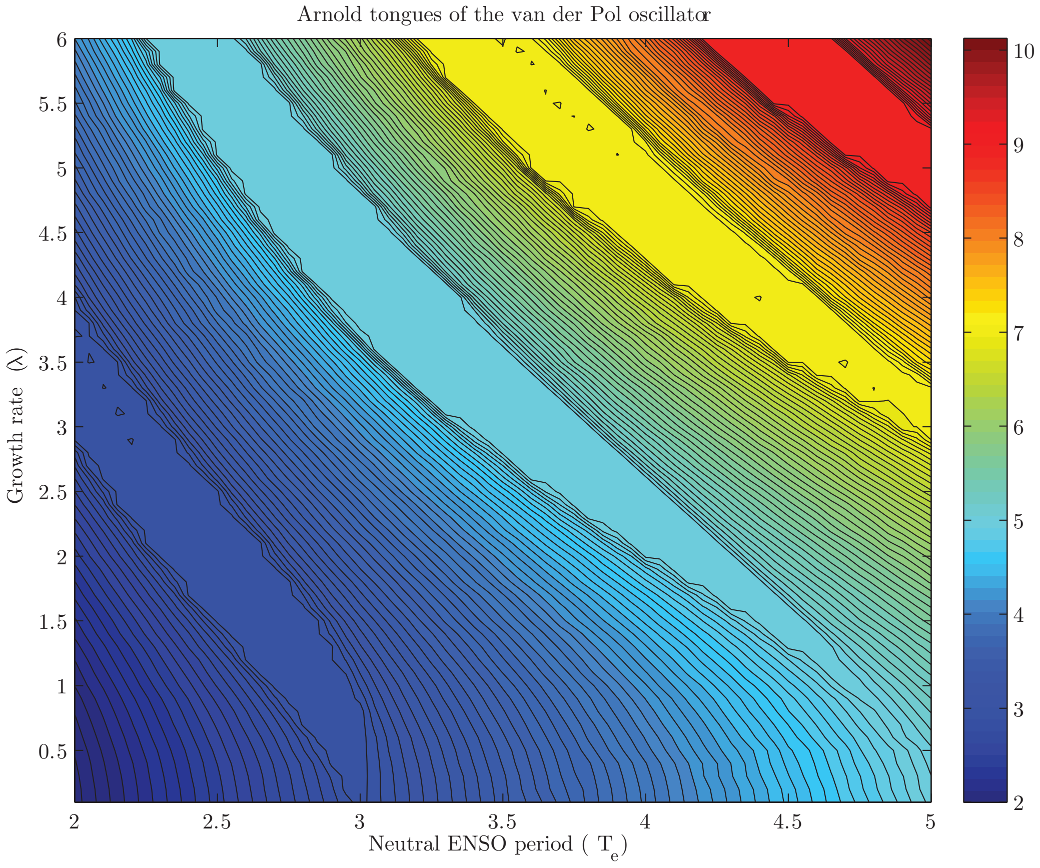

Figure 6.2: Contours of the ratio of the T output frequency to the forcing frequency in the van der Pol oscillator for various values of the growth rate (λ) and neutral ENSO period(T_e). Multiple regions of frequency locking (Arnol'd tongues) are evident in the parameter space of the model, preferentially occurring at odd multiples of the driving frequency. The mean frequency of the output was measured as the mean gradient of the unwrapped phase time series.

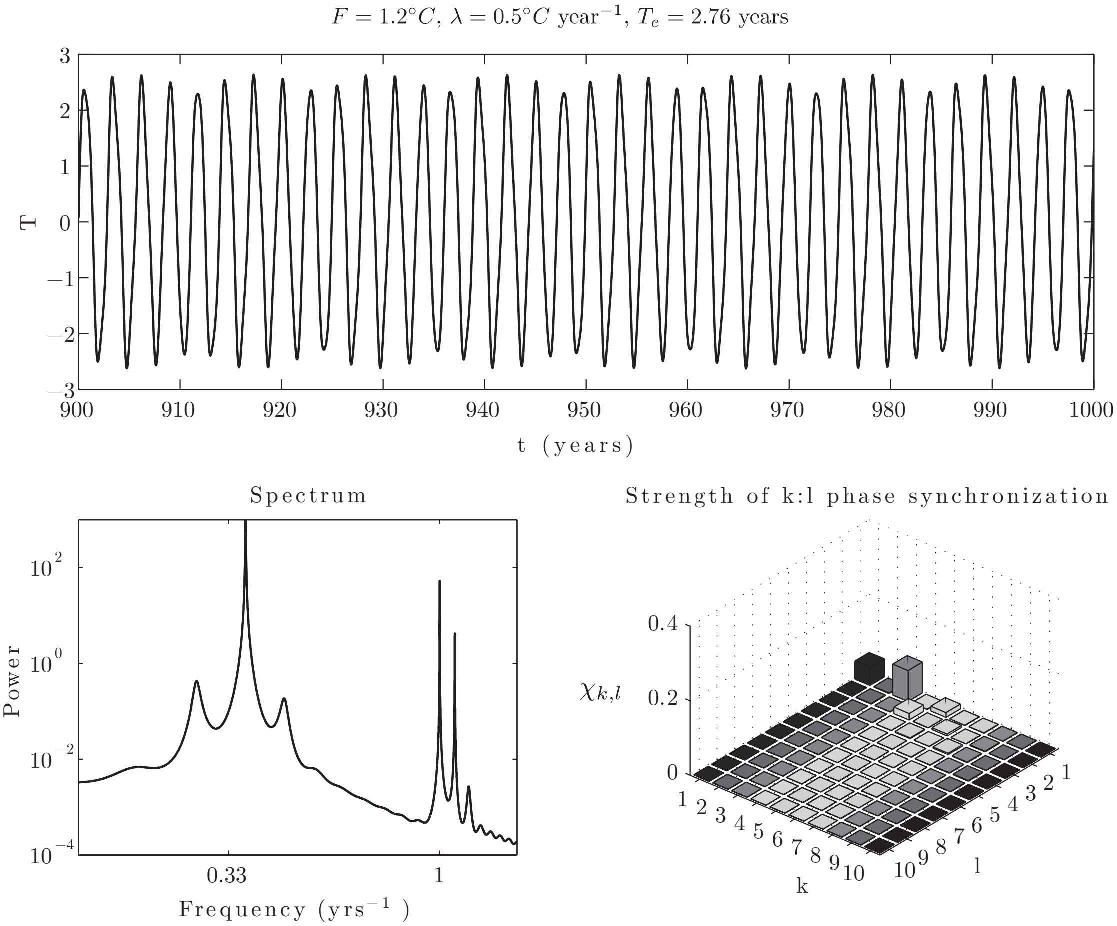
$F = 1.2°C$, $\lambda = 0.5°C$ year^{-1}, $T_e = 2.76$ years

Spectrum

Strength of k:l phase synchronization

Figure 6.3: The time series (top) and spectrum (bottom left) of a quasiperiodic oscillation obtained from a run of the van der Pol oscillator with parameter values $F = 1.2°C$, $\lambda = \frac{1}{2}°C$ year^{-1}, and $T_e = 2.76$ years. The strength of the phase synchronization of the T time series with the periodic forcing for various rational multiples of $k : l$ is shown in the bottom right. See text for the definition of the phase synchronization index.

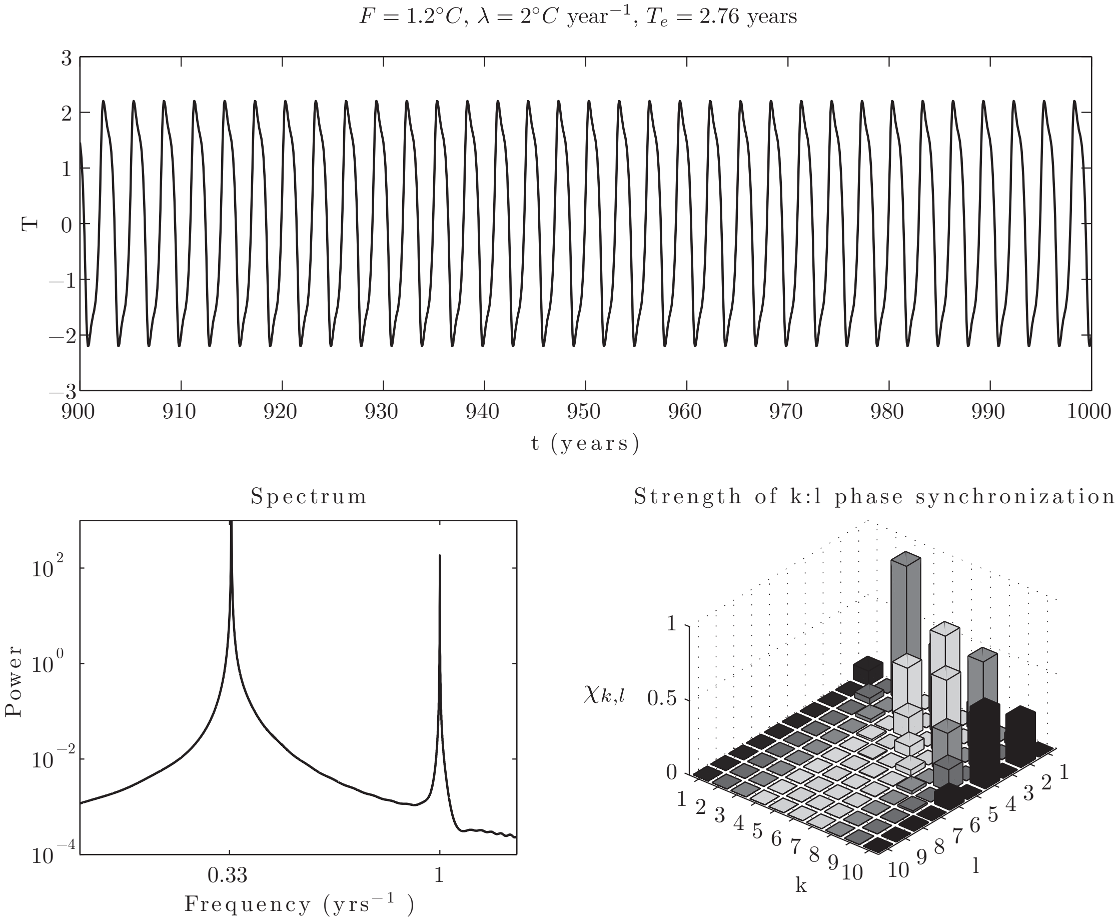

Figure 6.4: The time series (top) and spectrum (bottom left) of a frequency locked oscillation obtained from a run of the van der Pol oscillator with parameter values $F = 1.2°C$, $\lambda = 2°C$ yr^{-1}, and $T_e = 2.76$ yrs. The strength of the phase synchronization of the T time series with the periodic forcing for various rational multiples of $k : l$ is shown in the bottom right. See text for the definition of the phase synchronization index.

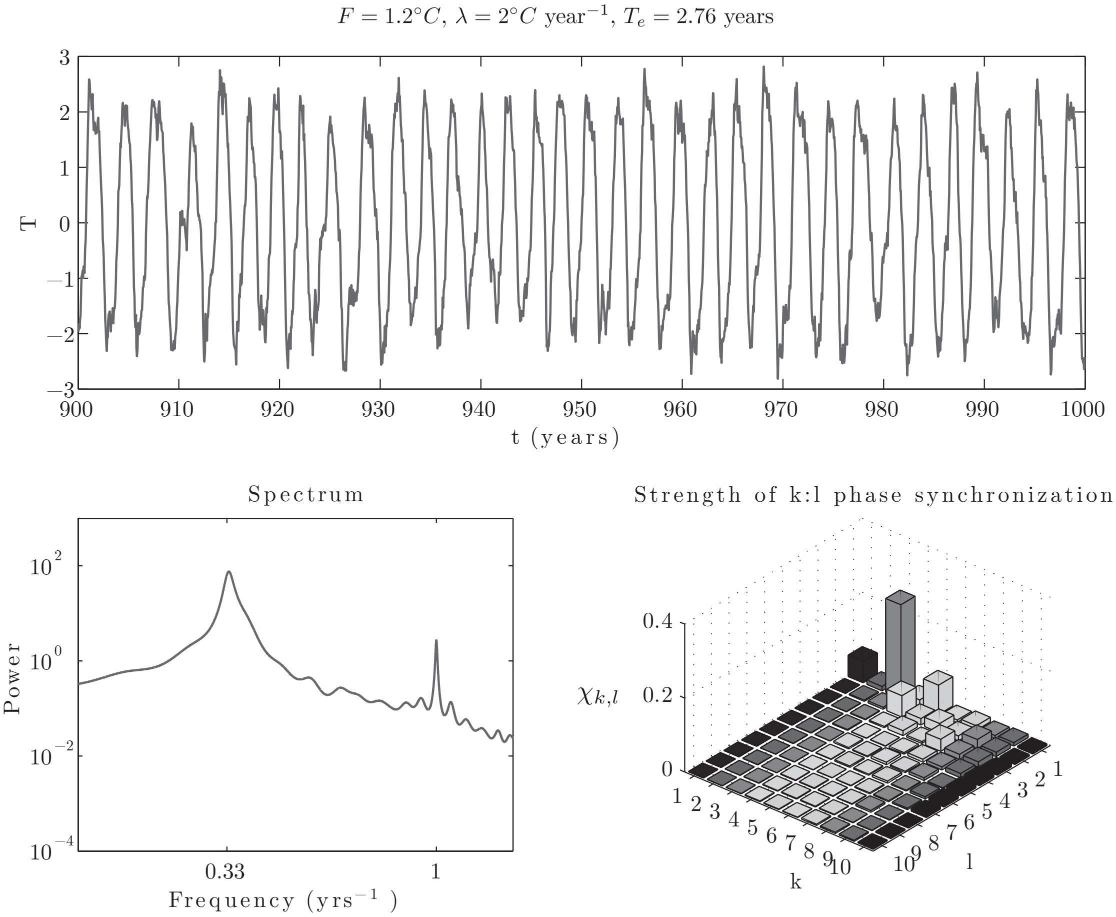

Figure 6.5: The same as in Figure 6.4, but with the inclusion of Gaussian stochastic noise forcing in the model.

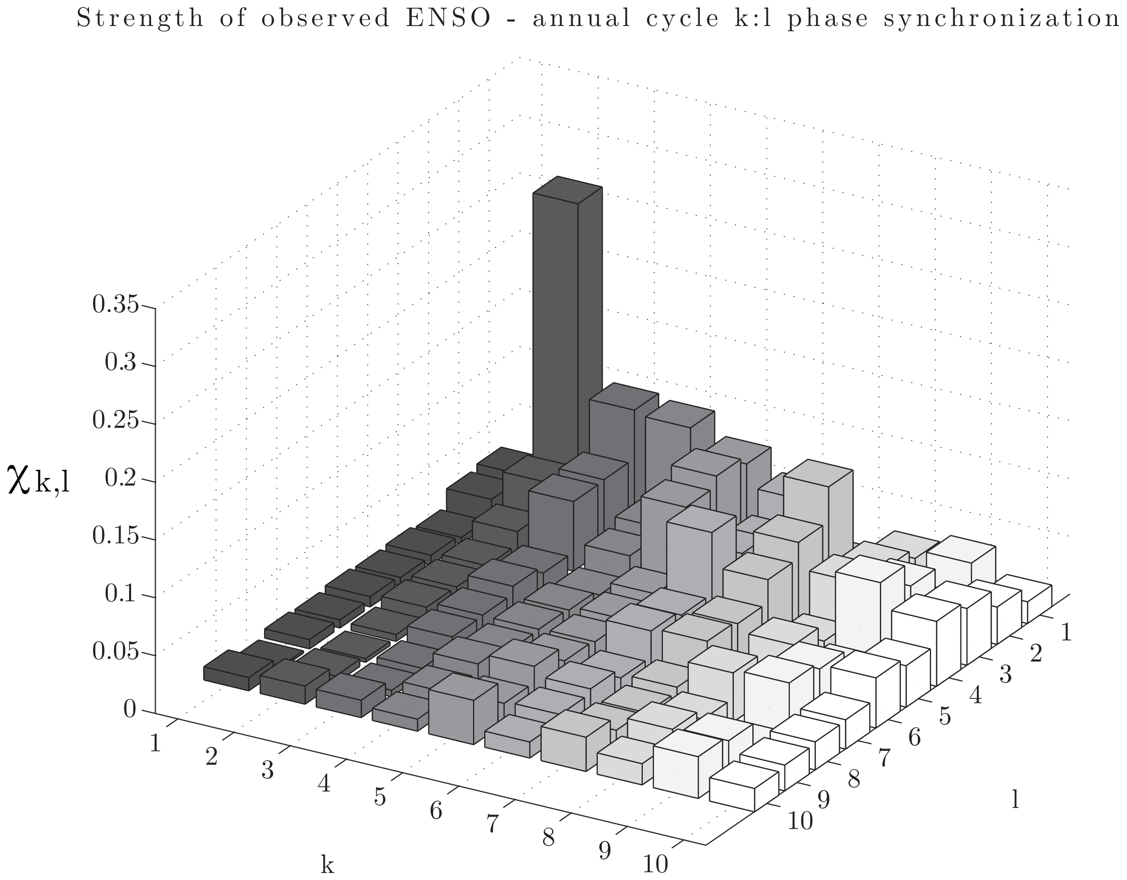

Figure 6.6: Indices measuring the strength of the observed $k : l$ phase synchronization ($\chi_{k,l}$) of ENSO to the annual cycle for values of $k, l \in [1, 10]$. See text for definition of the phase synchronization index.

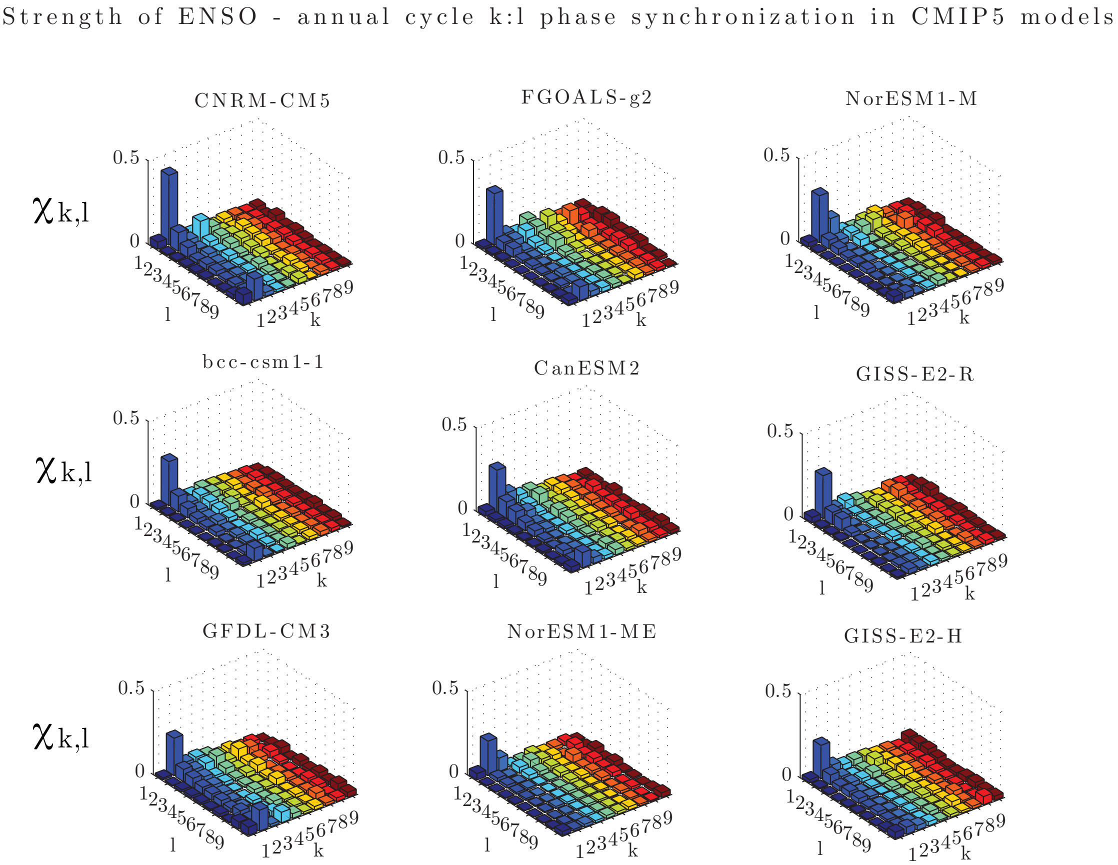

Figure 6.7: Indices measuring the strength of the $k : l$ phase synchronization ($\chi_{k,l}$) of ENSO to the annual cycle for values of $k, l \in [1, 10]$, as simulated by CGCMs participating in CMIP5. See text for definition of the phase synchronization index.

Chapter 7

Discussion

In addition to the PRO model's ability to capture the various features of ENSO synchronization, the results presented here very nicely complement other recent observational studies on annual cycle - ENSO interactions. As mentioned before, a newly identified climate mode, corresponding to the second principal component of an EOF decomposition of western Pacific winds, has been shown to have energy at the $\omega_a - \omega_e$ combination tone frequency (Stuecker et al., 2013). The spatial pattern of the mode captures the development of the Philippine Sea anticyclone (Wang et al., 1999), as well as the southward shift of westerly wind anomalies in the western Pacific (McGregor et al., 2012) during El Niño events. These two features have been proposed as possible mechanisms for ENSO phase transition via the modulation of the atmospheric response to SST anomalies and thereby ENSO's growth rate, captured heuristically in the PRO model via the modulation of λ. In turn, the modulation of the growth rate (λ) in the PRO model results directly in energy at combination tone frequencies (4.8) due to the nonlinear interaction of ENSO and the annual cycle. It is important to note that the combination tone is proposed to be due to the interaction of El Niño events with the annual cycle, so there is an apparent asymmetry in the observed system not accounted for in the PRO model.

The combination of the analytical PRO model results and the observation of the combination climate mode suggests that the most important ENSO - annual cycle interaction occurs in the atmosphere over the western Pacific, which helps to narrow down the myriad possible physical interactions that could result in the modulation of ENSO's growth rate by the annual cycle (see Chapter 1). This idea could be tested by examining characteristics of the various CMIP5 CGCM simulations of the western Pacific and relating them systematically to the strength of the synchronization of ENSO to the annual cycle within each model (Figure 2.6). The analysis of the CMIP5 output suggest that there is a universal scaling of the models according to the strength of ENSO synchronization that might be related to e.g. biases the location and strength of western Pacific atmospheric convection, SST, surface winds, et cetera. If such a connection were made, it would useful as a way to evaluate and improve coupled general circulation models and provide insight into the physics of ENSO - annual cycle interaction.

Though the PRO model appears to capture the salient features of ENSO synchronization as presented here, and is further supported by the observed ENSO - annual cycle combination climate mode, the model has essential limitations that should be discussed. Throughout this work we have considered only the two leading theories for ENSO synchronization to the annual cycle, that the synchronization results from the seasonal modulation of ENSO's growth rate or from frequency locking of ENSO to the periodic forcing by the annual cycle. These two theories correspond to limiting cases of the following model:

$$\frac{dT}{dt} = \lambda(t)T + \omega_e H - cT^3 + F\sin(\omega_a t) + \xi(t) \tag{7.1}$$

$$\frac{dH}{dt} = -\omega_e T, \tag{7.2}$$

which includes the seasonal variation of ENSO's growth rate, nonlinear saturation, periodic forcing by the annual cycle, and stochastic atmospheric forcing at fast time scales. The effect of the seasonal modulation of ENSO's growth rate was represented by the parametric recharge oscillator (PRO) model of ENSO, which corresponds to the limiting cases of $c = F = 0$. Frequency locking of ENSO to the annual cycle was captured by the limiting case $\lambda(t) = \bar{\lambda} > 0$.

Besides these two limiting cases, there are other possible scenarios that are outside the scope of this study but which may warrant further investigation. For example, one could consider the interaction of the seasonally varying growth rate ($\lambda(t)$) and the nonlinear saturation term ($-cT^3$) in the system, or the effect of seasonally varying (Hendon et al., 2007) or state-dependent stochastic noise forcing (Kessler et al., 1995; Kessler and Kleeman, 2000; Jin et al., 2007; Levine and Jin, 2010). The importance of the various interactions within the full system (7.1,7.2) would be dependant on the balance between the mean damping/growth rate ($\bar{\lambda}$), the strength of the nonlinearity (c), the strength of the periodic forcing (F), and the variance of the stochastic forcing ($\xi(t)$). Clearly, the complexity increases rapidly even within the simplest model representation of ENSO, and the increased complexity must be justified by an increased understanding of ENSO or ability to explain features of ENSO beyond the stochastically forced model with seasonally varying growth rate. Of the possible avenues of investigation, the inclusion of state-dependent (mulitplicative) noise forcing (Levine and Jin, 2010) in the system seems the most fruitful, as it can reproduce ENSO skewness (Burgers and Stephenson, 1999; An and Jin, 2004), a feature that is not present in the symmetric models presented here.

More generally, the oscillator models used in this study only consider the unidirectional effect of the annual cycle on ENSO dynamics. The simple models thus neglect the modulation of the annual cycle as well as the possible interaction of three or more coupled modes (Penland and Sardeshmukh, 1995), though the comparison of the results based on the CEOF technique and on the Nino3.4 index suggests the modulation of the annual cycle may not be important for ENSO synchronization. The models also assume that ENSO is indeed an oscillation, rather than a series of events with no system memory carried over from one event to the next (Kessler, 2002). The latter view of ENSO is not entirely inconsistent with the damped, forced case of the PRO model, depending upon the mean damping rate of the model. With the damping rate of ENSO based on the OFES hindcast, the e-folding timescale of the model is ≈ 2.5 years, so anomalies would be $> 90\%$ damped out over six years without continuous forcing. Thus, model events separated by six years or longer can be considered essentially independent. However, the observed tendency for the amplitude of the system to persist over El Niño events but not La Niña events (Kessler, 2002), suggest a shorter timescale of ≈ 18 months, as well as an asymmetry in the system. The phase transition in the PRO model is necessary for ENSO synchronization with the annual cycle, as is apparent when considering the first order autoregessive (AR1) model of ENSO,

$$\frac{dT}{dt} = -\lambda(t)T + \xi(t), \tag{7.3}$$

where $\lambda(t) = \overline{\lambda} + \epsilon \cos(\omega_a t)$, with the mean damping rate set to $\overline{\lambda} = 0.4$ years^{-1} and Gaussian stochastic noise with a variance of $0.04°C$. The AR1 model was thus obtained by removing the H time series from the damped, forced PRO model and retaining the damping parameter and stochastic forcing. An ensemble run of the AR1 model, performed in the same way as for the damped PRO model (Figure 5.2), shows no synchronization with the annual cycle despite the modulation of the damping rate (Figure 7.1). The implication is that the phase transition which results from the subsurface ocean "memory" is essential to the synchronization of ENSO with the annual cycle. In the observations, this phase transition may be asymmetric, with La Niña events having a stronger tendency to follow El Niño events than vice versa. It may be possible to capture this feature within the recharge oscillator model if the growth rate were both time and state dependent, i.e. $\lambda = \lambda(T, t)$. This would also have the effect of introducing and quadratic nonlinearity into the system, which could potentially enhance the 2:1 synchronization with the annual cycle. Overall, it appears that the most important feature of ENSO not captured by the PRO model is the asymmetry between El Niño and La Niña events, a shortcoming that could be addressed in future studies.

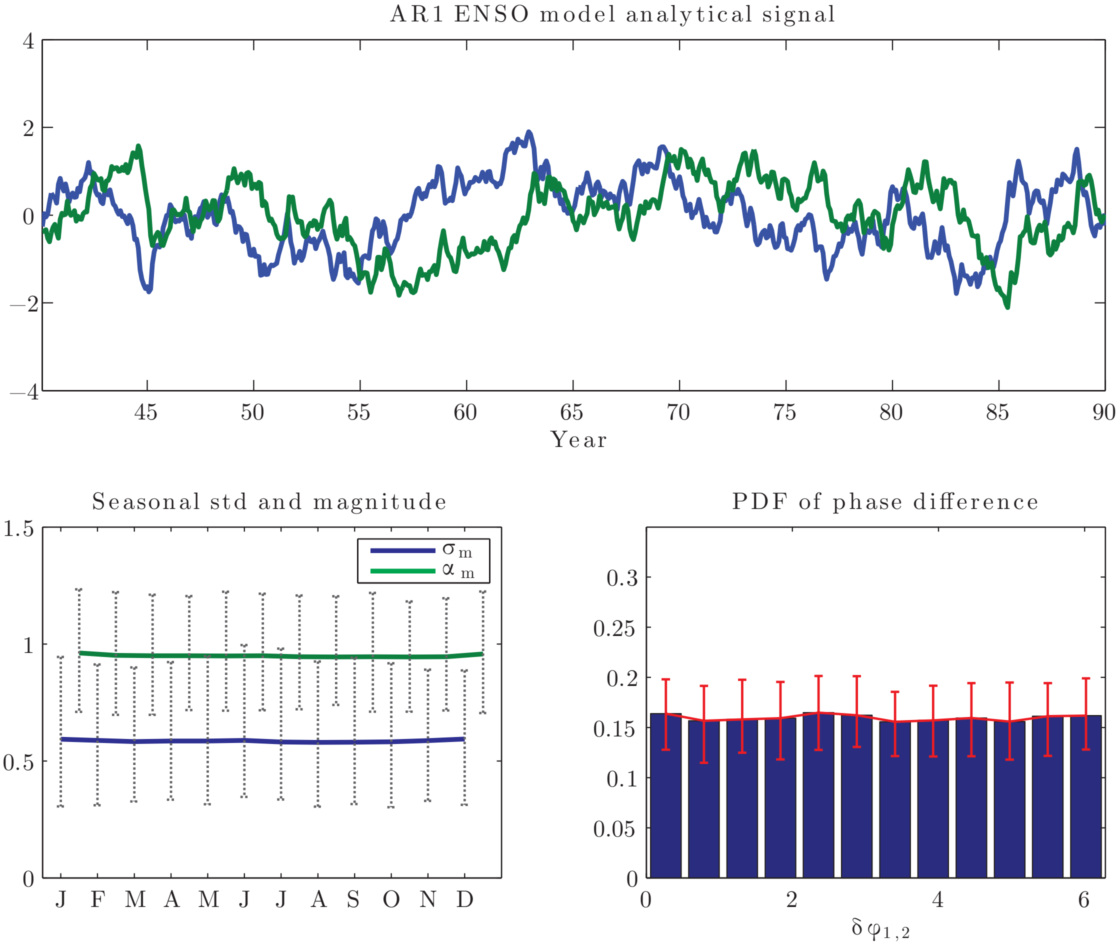

Figure 7.1: (Top) An example of the T time series and the Hilbert transform of the time series, from a single member of an ensemble of integrations of the a first order autoregressive model of ENSO (7.3). (Bottom left) The ensemble mean monthly variance of the T time series and the ensemble mean monthly amplitude of the analytical signal of the time series. (Bottom right) A PDF of the $\delta\phi_{2,1}$ phase difference of ENSO with the annual cycle. 90% confidence intervals for the seasonal variance, amplitude modulation, and PDF of the phase difference, based on the 100 member ensemble, are shown.

Chapter 8

Summary and Conclusions

The two leading theories of ENSO seasonal synchronization are that ENSO is frequency locked to periodic forcing by the annual cycle (Jin et al., 1994; Tziperman et al., 1994) or that the seasonal modulation of ENSO's growth rate leads to the synchronization of ENSO events (Philander et al., 1984; Hirst, 1986). These two theories were tested here within the a consistent model framework baed on the recharge osicllator model of ENSO (Jin, 1997). The observed ENSO synchronization, as well as the synchronization simulated by state of the art CGCMs, was described in terms of ENSO's seasonal variance, amplitude modulation, phase synchronization, and secondary peaks in the spectra at "combination tones" with the annual cycle. These synchronization metrics were then compared to those of the parametric recharge oscillator (PRO) model of ENSO, which captures in the simplest form the seasonal modulation of ENSO's growth by the annual cycle. Analytical results of the neutral, unforced case of the PRO model show that the annual modulation of the growth rate parameter results directly in all of the synchronization features, and the strength of each of the synchronization features agree well with those of the observations. The analytical solutions were shown to be very good approximations of the behaviour of PRO model numerical simulations for both the neutral case, and for the long-term behaviour of the damped PRO model excited by stochastic forcing. Further, analytical and numerical results from the PRO model explain the relationship between synchronization features across the range of the CGCMs. The results are further supported by the recent identification of a climate mode with energy at the combination tone frequency that results from the nonlinear interaction of ENSO and the annual cycle (Stuecker et al., 2013).

Next, the scenario that ENSO synchronization results from a manifestation of subharmonic frequency locking to the annual cycle was examined within the same recharge oscillator model framework. To do so, the behavior of the oscillator model was examined with the inclusion of periodic forcing by the annual cycle and a cubic damping term representing the nonlinear saturation of SST anomalies. The system was shown to be equivalent to the periodically forced van der Pol oscillator (van der Pol, 1927), which has similar global behavior to the ENSO models on which the frequency locking scenario is based, and which allows the same suite of model solutions: quasiperiodic, frequency locked, and chaotic oscillations. The characteristics of each type of solution were then compared to the observed ENSO. Chaotic oscillations were not found within the parameter space of the van der Pol oscillator relevant to the observed ENSO, and occur only rarely in the parameter space of other ENSO models (Jin et al., 1996), so it is unlikely that the observed ENSO characteristics are due to chaotic interaction with the annual cycle. Moreover, chaotic solutions retain the subharmonic peaks associated with frequency locked solutions (Jin et al., 1996), so the chaotic case can be considered along with the frequency locked case. Quasiperiodic oscillations will only coincidentally produce synchronization will the annual cycle, and so are unlikely to account for the observed ENSO characteristics as well. Frequency locked solutions could account for the observed ENSO synchronization, but are far more regular than the observed ENSO, so a stochastically perturbed frequency locked oscillation remains the only realistic model solution. In such a system, the frequency locking will be accompanied by phase synchronization at the same rational multiple of the annual cycle. In the observations, the only evidence of frequency locking occurs at a ratio of 2 : 1, but this phase synchronization is not associated with a peak in the spectrum at the biennial frequency. The results indicate that the annual modulation of the coupled stability of the equatorial Pacific ocean-atmosphere system is by far the more likely mechanism generating the synchronization of ENSO events to the annual cycle.

Appendix A

Supplementary figures

The spatial patterns of first two modes of the CEOF decomposition of equatorial SST (20°S - 20°N, 110 – 290°E) GCM output from CMIP5 historical runs (1901 - 2000) are included here, to display the representations of the annual cycle and ENSO within each of the models. Each figure shows contours of the phase spatial pattern of the first two modes (r_1,r_2), along with shading related to the value of the spatial amplitude (q_1,q_2). The darker shading indicates larger values of the spatial amplitude, and vice versa. The models produce a variety of simulated annual cycles and ENSOs, and qualitatively speaking, the models that produce more realistic simulations of ENSO and the annual cycle tend to have values of ENSO synchronization indices near the observations (Figure 3.6). However, no systematic relationship was found between the verisimilitude of the spatial patterns and the values of the synchronization indices.

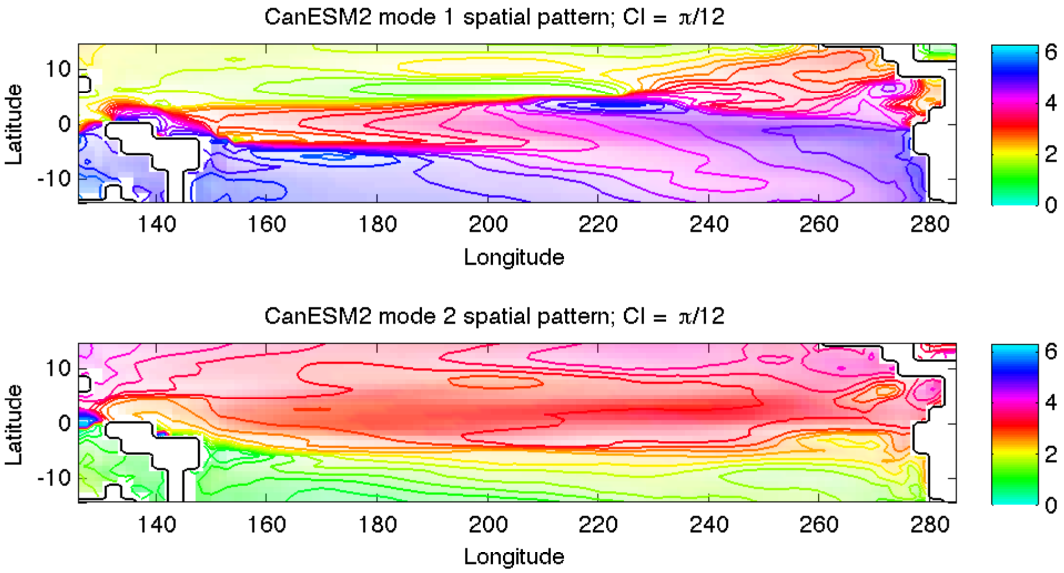

Figure A.1: Contours of the phase spatial pattern (r_n) of the first mode (annual cycle, top) and second mode (ENSO, bottom) of the CEOF decomposition of equatorial SST output from a historical run (1901-2000) of the Canadian Earth System Model. The shading indicates the value of the amplitude spatial pattern (q_n), where darker shading indicates larger amplitude.

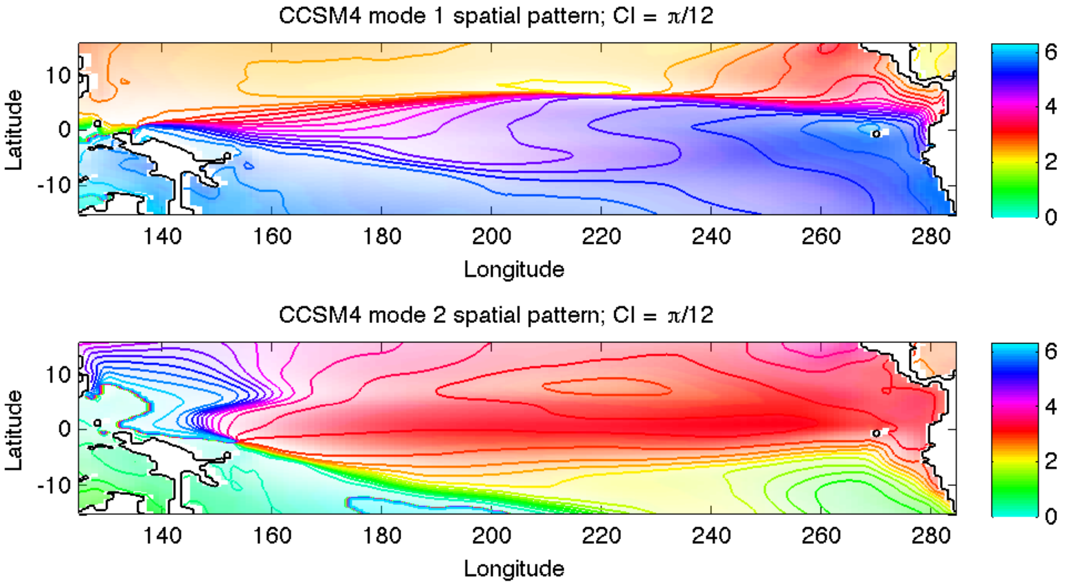
CCSM4 mode 1 spatial pattern; CI = π/12
Latitude
10
0
-10
140
160
180
200
220
240
260
280
Longitude
6
4
2
0
CCSM4 mode 2 spatial pattern; CI = π/12
Latitude
10
0
-10
140
160
180
200
220
240
260
280
Longitude
6
4
2
0

Figure A.2: Contours of the phase spatial pattern (r_n) of the first mode (annual cycle, top) and second mode (ENSO, bottom) of the CEOF decomposition of equatorial SST output from a historical run (1901-2000) of the Community Climate System Model. The shading indicates the value of the amplitude spatial pattern (q_n), where darker shading indicates larger amplitude.

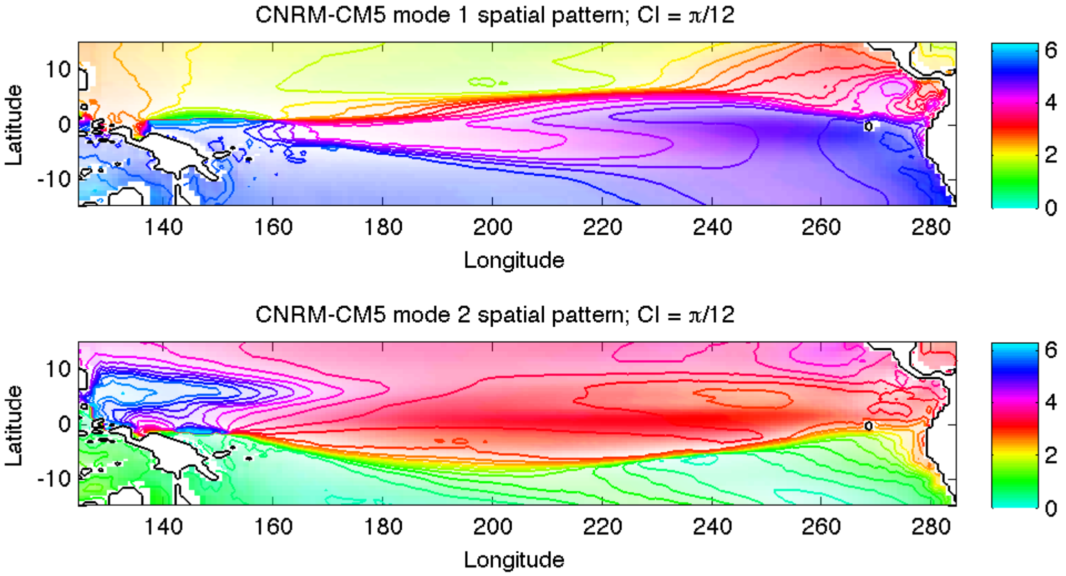
CNRM-CM5 mode 1 spatial pattern; CI = π/12

CNRM-CM5 mode 2 spatial pattern; CI = π/12

Latitude
10
0
-10
Longitude
140
160
180
200
220
240
260
280
6
4
2
0

Figure A.3: Contours of the phase spatial pattern (r_n) of the first mode (annual cycle, top) and second mode (ENSO, bottom) of the CEOF decomposition of equatorial SST output from a historical run (1901-2000) of the National Centre for Meteorological Research Climate Model. The shading indicates the value of the amplitude spatial pattern (q_n), where darker shading indicates larger amplitude.

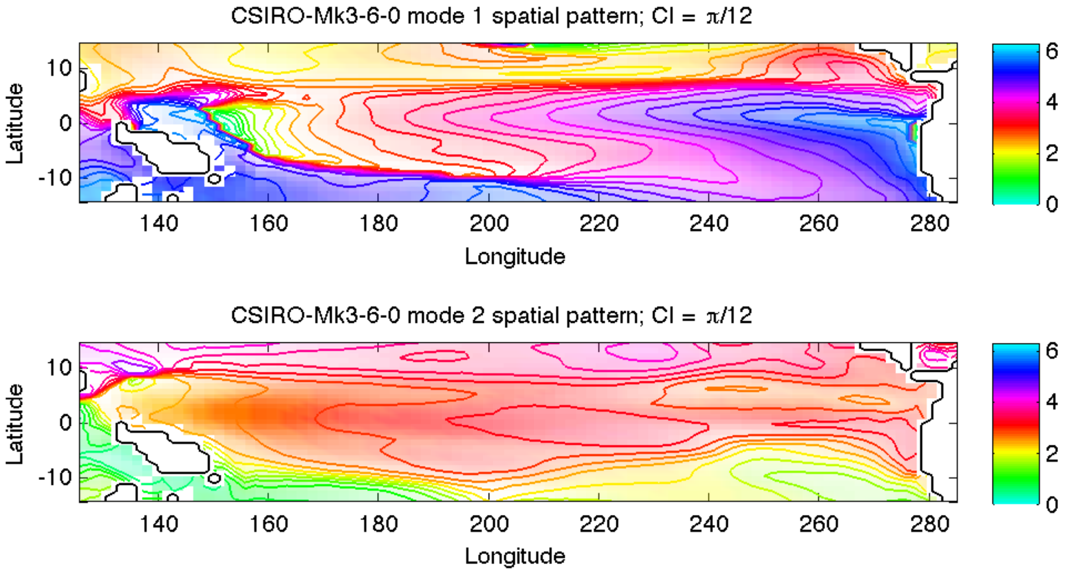

Figure A.4: Contours of the phase spatial pattern (r_n) of the first mode (annual cycle, top) and second mode (ENSO, bottom) of the CEOF decomposition of equatorial SST output from a historical run (1901-2000) of the Commonwealth Scientific and Industrial Research Organisation Global Climate Model. The shading indicates the value of the amplitude spatial pattern (q_n), where darker shading indicates larger amplitude.

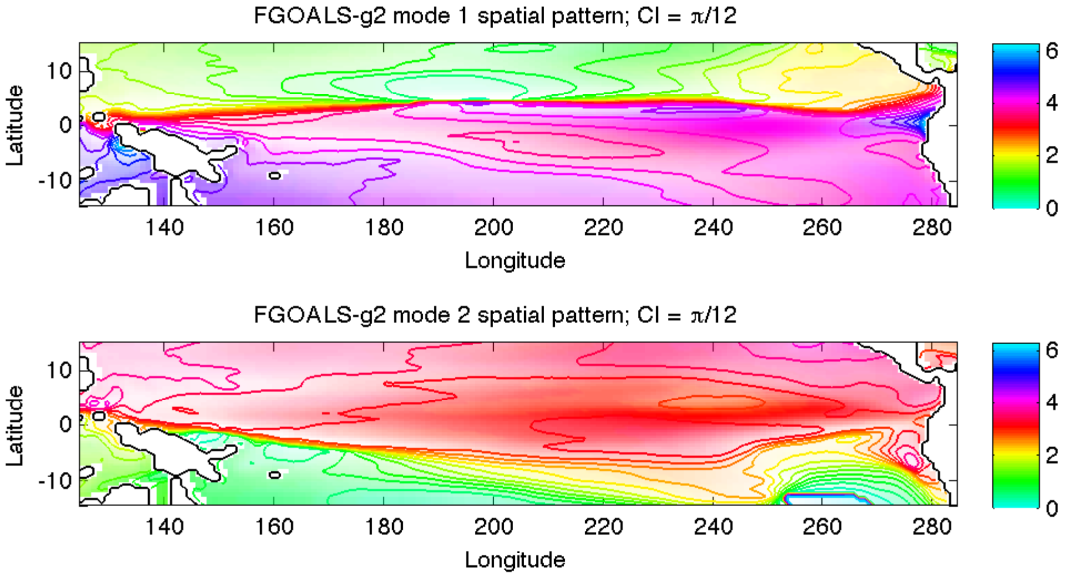

Figure A.5: Contours of the phase spatial pattern (r_n) of the first mode (annual cycle, top) and second mode (ENSO, bottom) of the CEOF decomposition of equatorial SST output from a historical run (1901-2000) of the Flexible Global Ocean-Atmosphere-Land System Model. The shading indicates the value of the amplitude spatial pattern (q_n), where darker shading indicates larger amplitude.

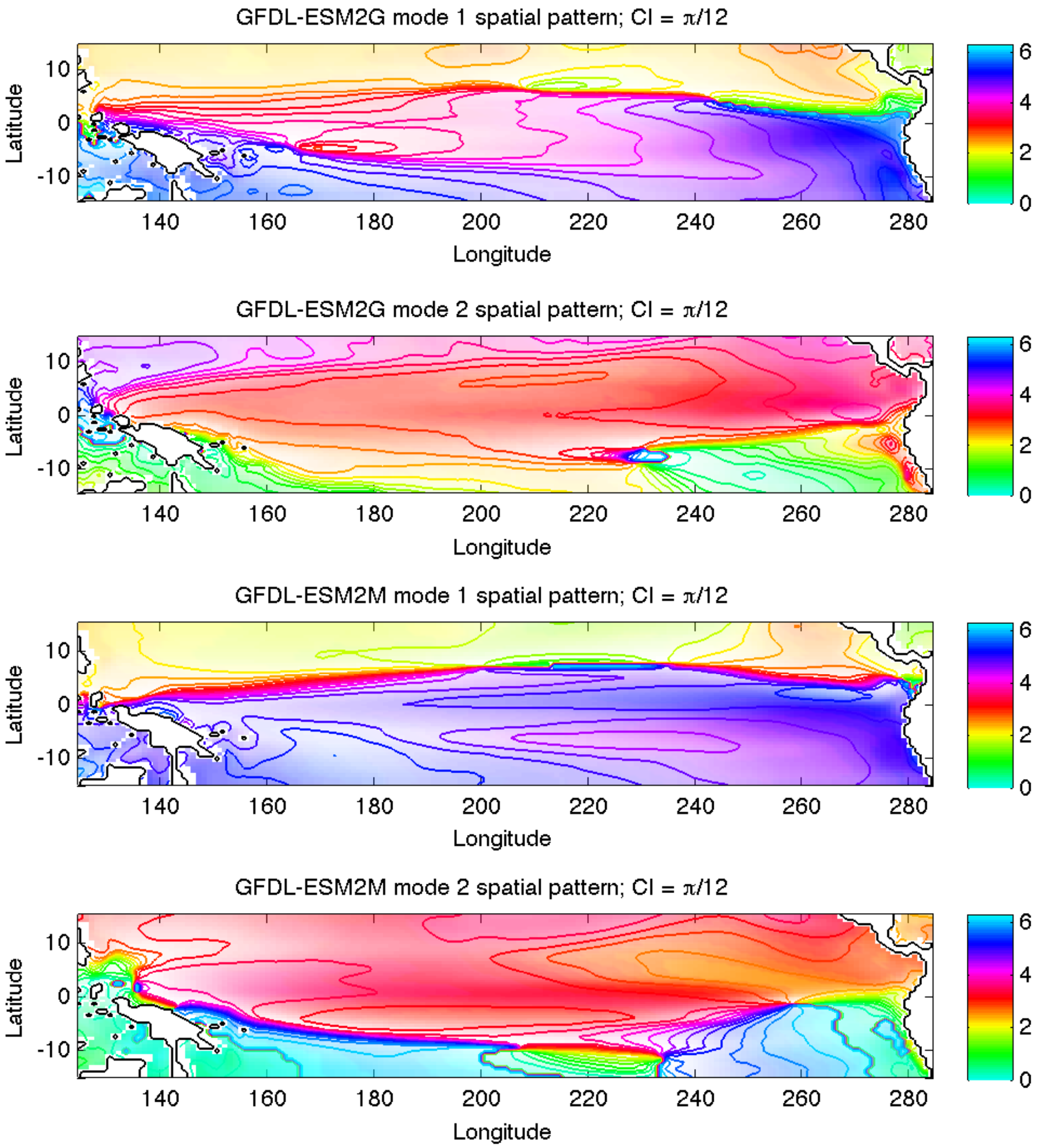

GFDL-ESM2G mode 1 spatial pattern; CI = $\pi/12$

GFDL-ESM2G mode 2 spatial pattern; CI = $\pi/12$

GFDL-ESM2M mode 1 spatial pattern; CI = $\pi/12$

GFDL-ESM2M mode 2 spatial pattern; CI = $\pi/12$

Figure A.6: Contours of the phase spatial pattern (r_n) of the first mode (annual cycle, top) and second mode (ENSO, bottom) of the CEOF decomposition of equatorial SST output from a historical run (1901-2000) of two configurations of the Geophysical Fluid Dynamics Laboratory Earth System Model. The shading indicates the value of the amplitude spatial pattern (q_n), where darker shading indicates larger amplitude.

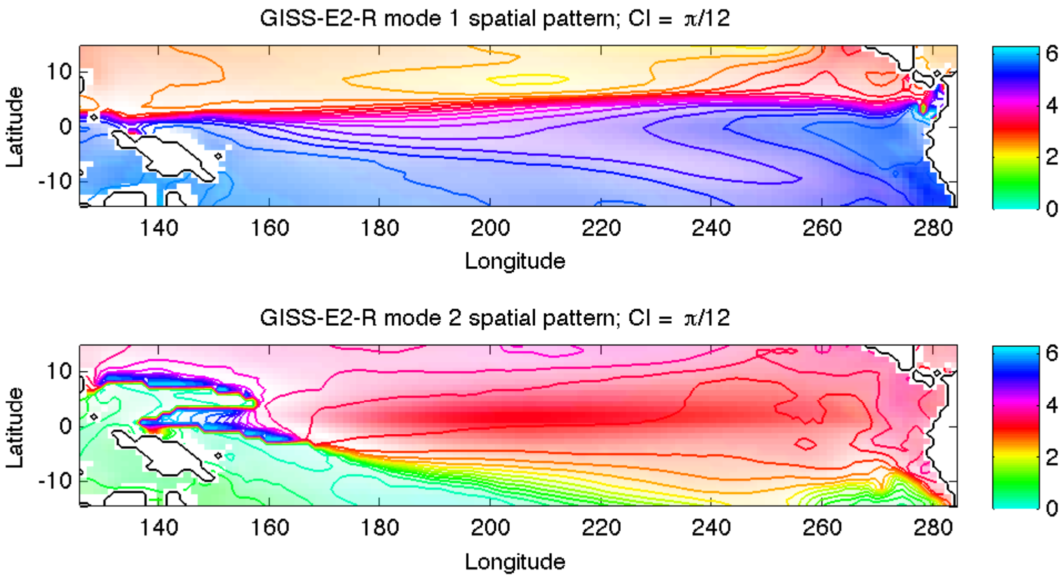

Figure A.7: Contours of the phase spatial pattern (r_n) of the first mode (annual cycle, top) and second mode (ENSO, bottom) of the CEOF decomposition of equatorial SST output from a historical run (1901-2000) of the NASA Goddard Institute for Space Studies Model E. The shading indicates the value of the amplitude spatial pattern (q_n), where darker shading indicates larger amplitude.

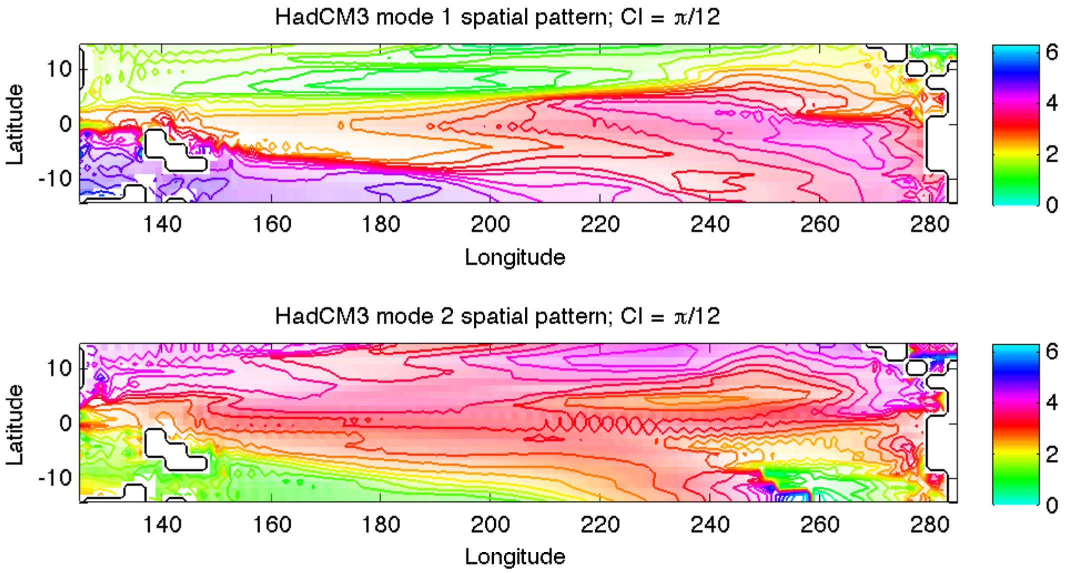

Figure A.8: Contours of the phase spatial pattern (r_n) of the first mode (annual cycle, top) and second mode (ENSO, bottom) of the CEOF decomposition of equatorial SST output from a historical run (1901-2000) of the Met Office Hadley Centre Climate prediction Model. The shading indicates the value of the amplitude spatial pattern (q_n), where darker shading indicates larger amplitude.

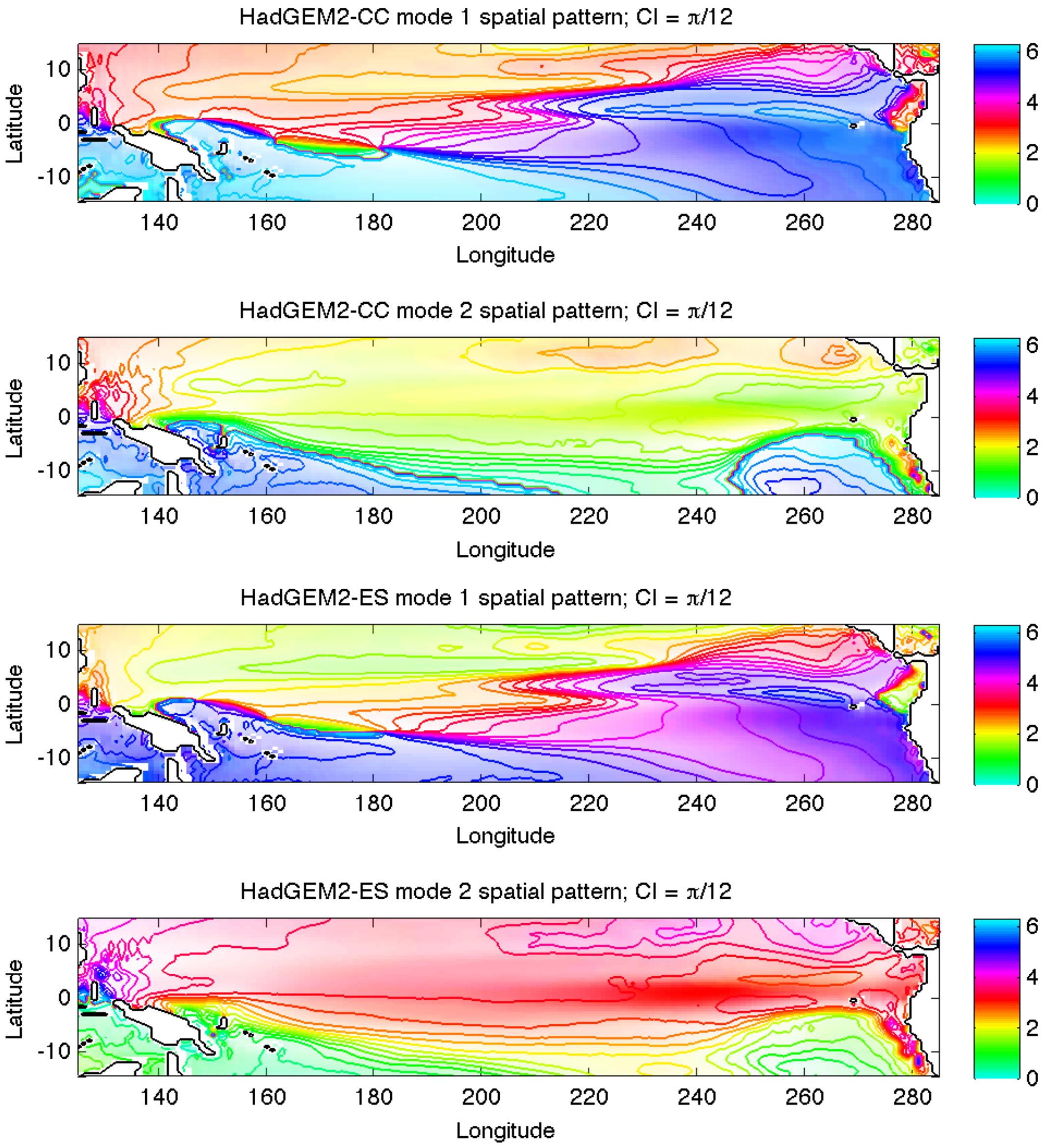
HadGEM2-CC mode 1 spatial pattern; CI = π/12

HadGEM2-CC mode 2 spatial pattern; CI = π/12

HadGEM2-ES mode 1 spatial pattern; CI = π/12

HadGEM2-ES mode 2 spatial pattern; CI = π/12

Latitude
10
0
-10
140
160
180
200
220
240
260
280
Longitude
6
4
2
0

Figure A.9: Contours of the phase spatial pattern (r_n) of the first mode (annual cycle, top) and second mode (ENSO, bottom) of the CEOF decomposition of equatorial SST output from a historical run (1901-2000) of the Met Office Hadley Centre Global Environmental Model. The shading indicates the value of the amplitude spatial pattern (q_n), where darker shading indicates larger amplitude.

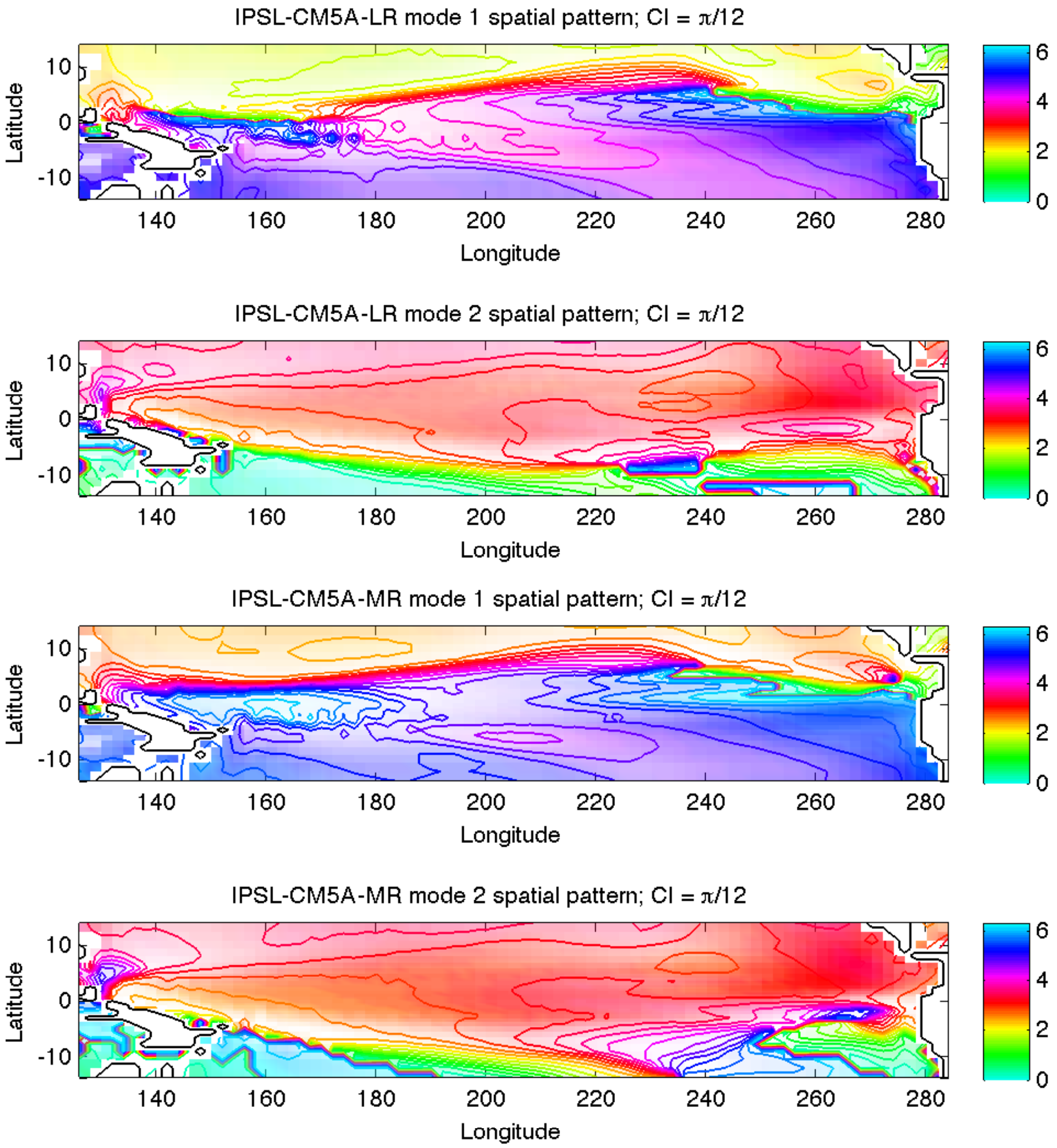
IPSL-CM5A-LR mode 1 spatial pattern; CI = $\pi/12$

IPSL-CM5A-LR mode 2 spatial pattern; CI = $\pi/12$

IPSL-CM5A-MR mode 1 spatial pattern; CI = $\pi/12$

IPSL-CM5A-MR mode 2 spatial pattern; CI = $\pi/12$

Figure A.10: Contours of the phase spatial pattern (r_n) of the first mode (annual cycle, top) and second mode (ENSO, bottom) of the CEOF decomposition of equatorial SST output from a historical run (1901-2000) of the Institut Pierre Simon Laplace Climate Model. The shading indicates the value of the amplitude spatial pattern (q_n), where darker shading indicates larger amplitude.

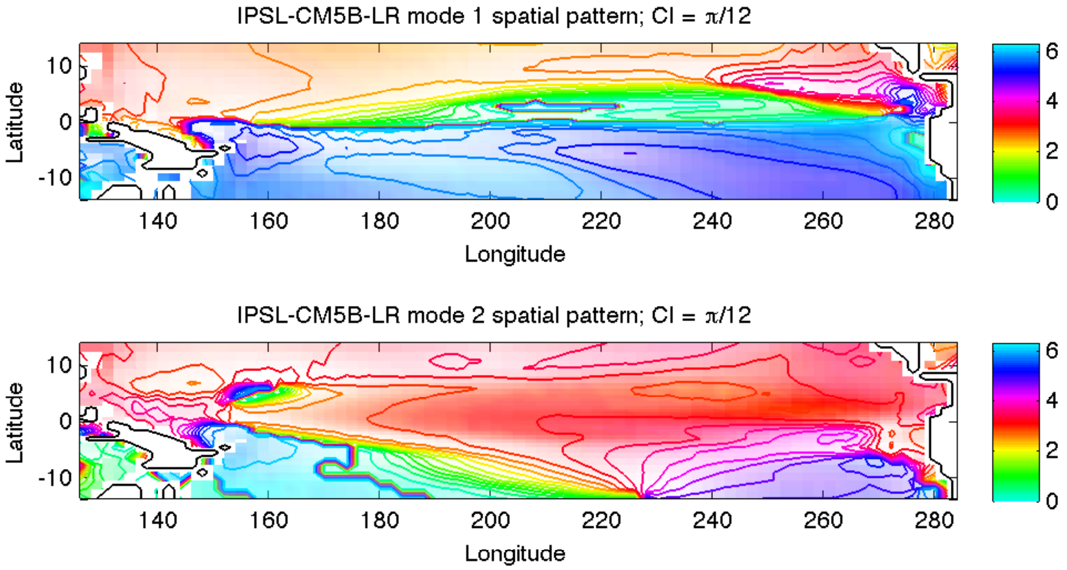
IPSL-CM5B-LR mode 1 spatial pattern; CI = $\pi/12$

IPSL-CM5B-LR mode 2 spatial pattern; CI = $\pi/12$

Latitude
10
0
-10
140
160
180
200
220
240
260
280
Longitude
6
4
2
0

Figure A.11: Contours of the phase spatial pattern (r_n) of the first mode (annual cycle, top) and second mode (ENSO, bottom) of the CEOF decomposition of equatorial SST output from a historical run (1901-2000) of the Institut Pierre Simon Laplace Climate Model. The shading indicates the value of the amplitude spatial pattern (q_n), where darker shading indicates larger amplitude.

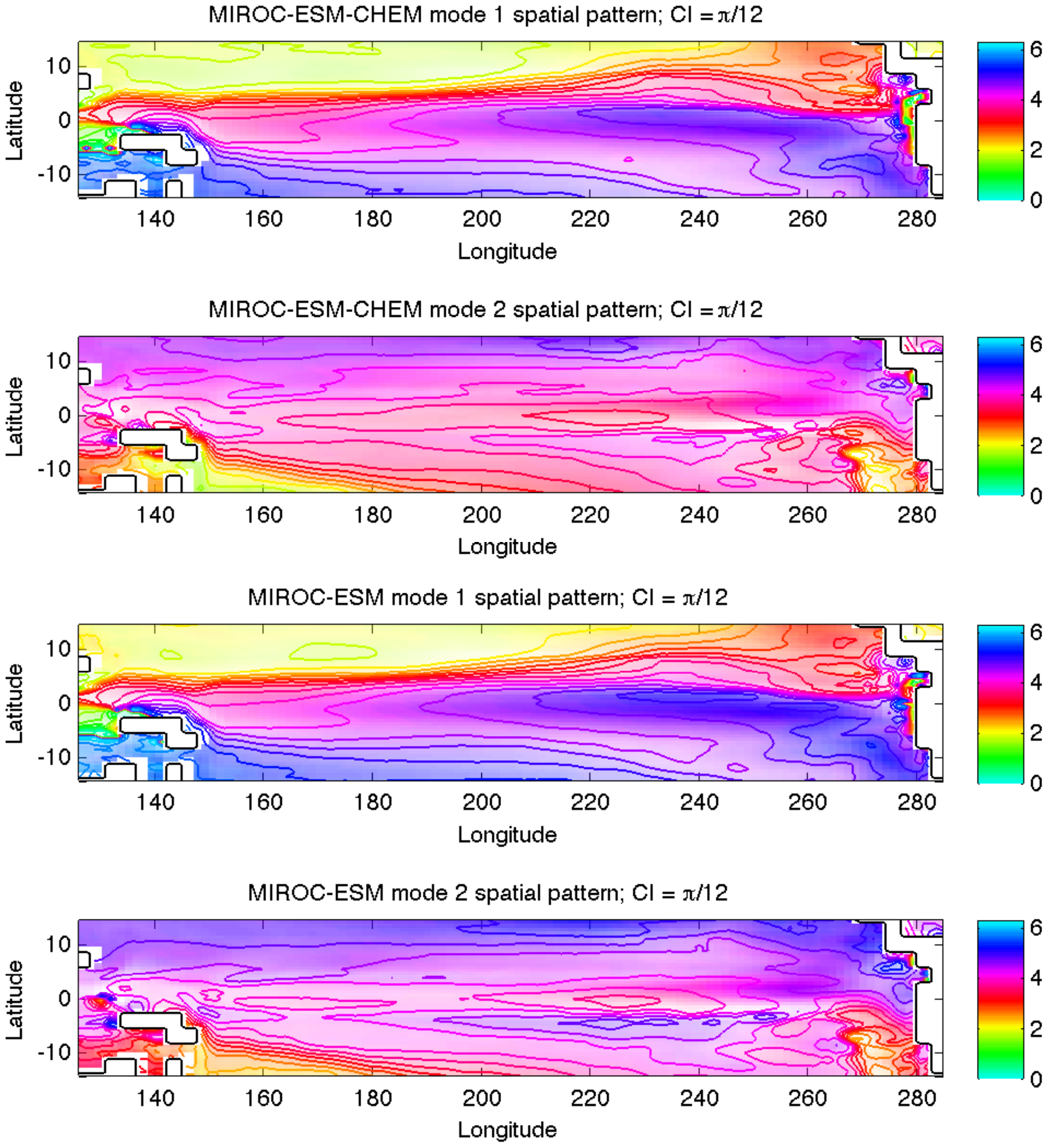
MIROC-ESM-CHEM mode 1 spatial pattern; CI = π/12

MIROC-ESM-CHEM mode 2 spatial pattern; CI = π/12

MIROC-ESM mode 1 spatial pattern; CI = π/12

MIROC-ESM mode 2 spatial pattern; CI = π/12

Figure A.12: Contours of the phase spatial pattern (r_n) of the first mode (annual cycle, top) and second mode (ENSO, bottom) of the CEOF decomposition of equatorial SST output from a historical run (1901-2000) of two configurations of the The Japan Agency for Marine-Earth Science and Technology Earth System Model. The shading indicates the value of the amplitude spatial pattern (q_n), where darker shading indicates larger amplitude.

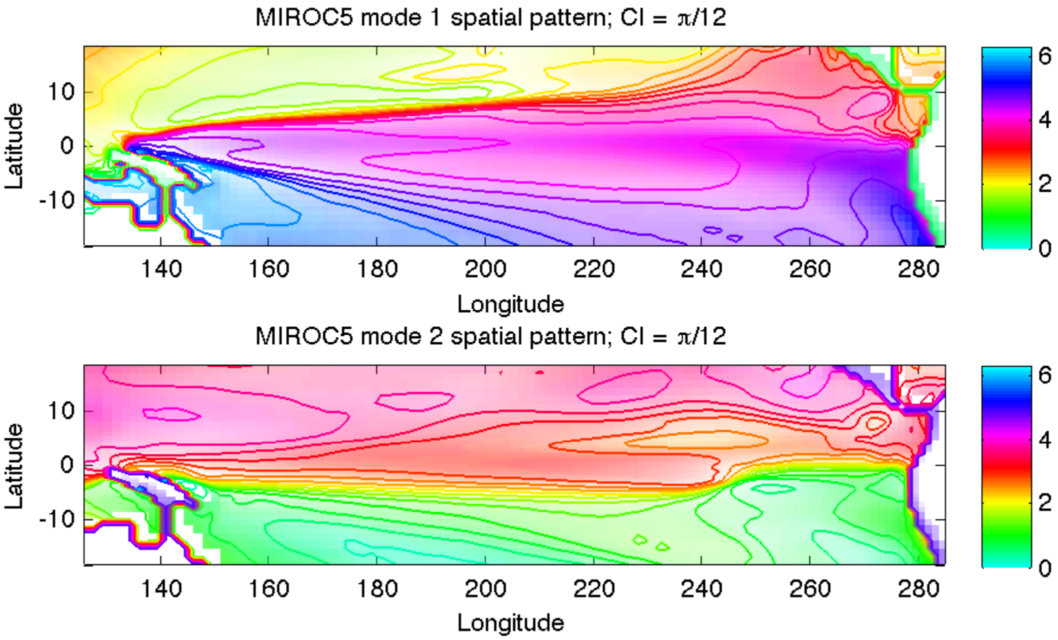

Figure A.13: Contours of the phase spatial pattern (r_n) of the first mode (annual cycle, top) and second mode (ENSO, bottom) of the CEOF decomposition of equatorial SST output from a historical run (1901-2000) of two configurations of the The Japan Agency for Marine-Earth Science and Technology Model for Interdisciplinary Research On Climate. The shading indicates the value of the amplitude spatial pattern (q_n), where darker shading indicates larger amplitude.

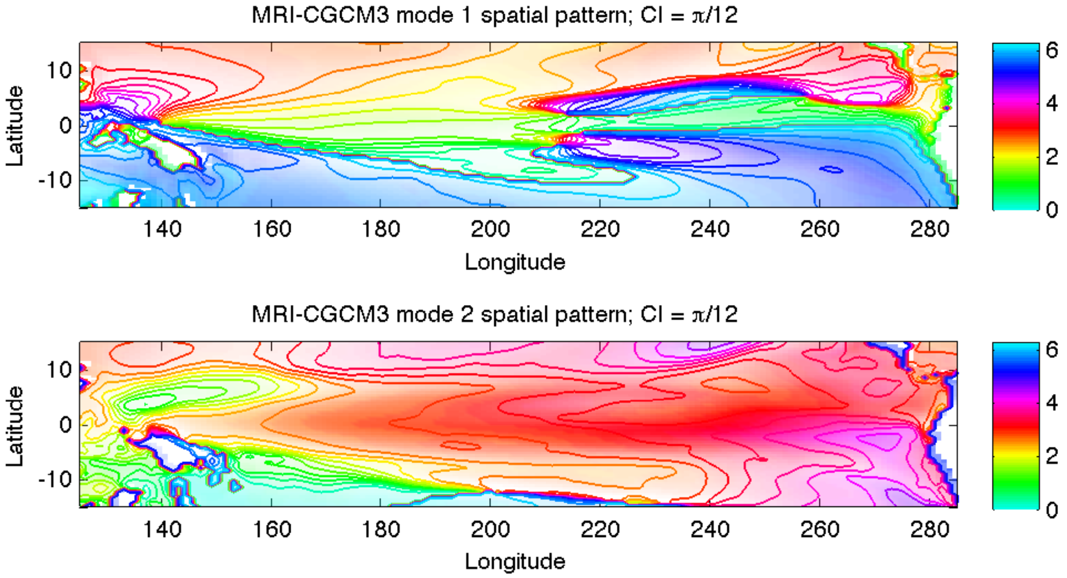

Figure A.14: Contours of the phase spatial pattern (r_n) of the first mode (annual cycle, top) and second mode (ENSO, bottom) of the CEOF decomposition of equatorial SST output from a historical run (1901-2000) of the Meteorological Research Institute Coupled Global Climate Model. The shading indicates the value of the amplitude spatial pattern (q_n), where darker shading indicates larger amplitude.

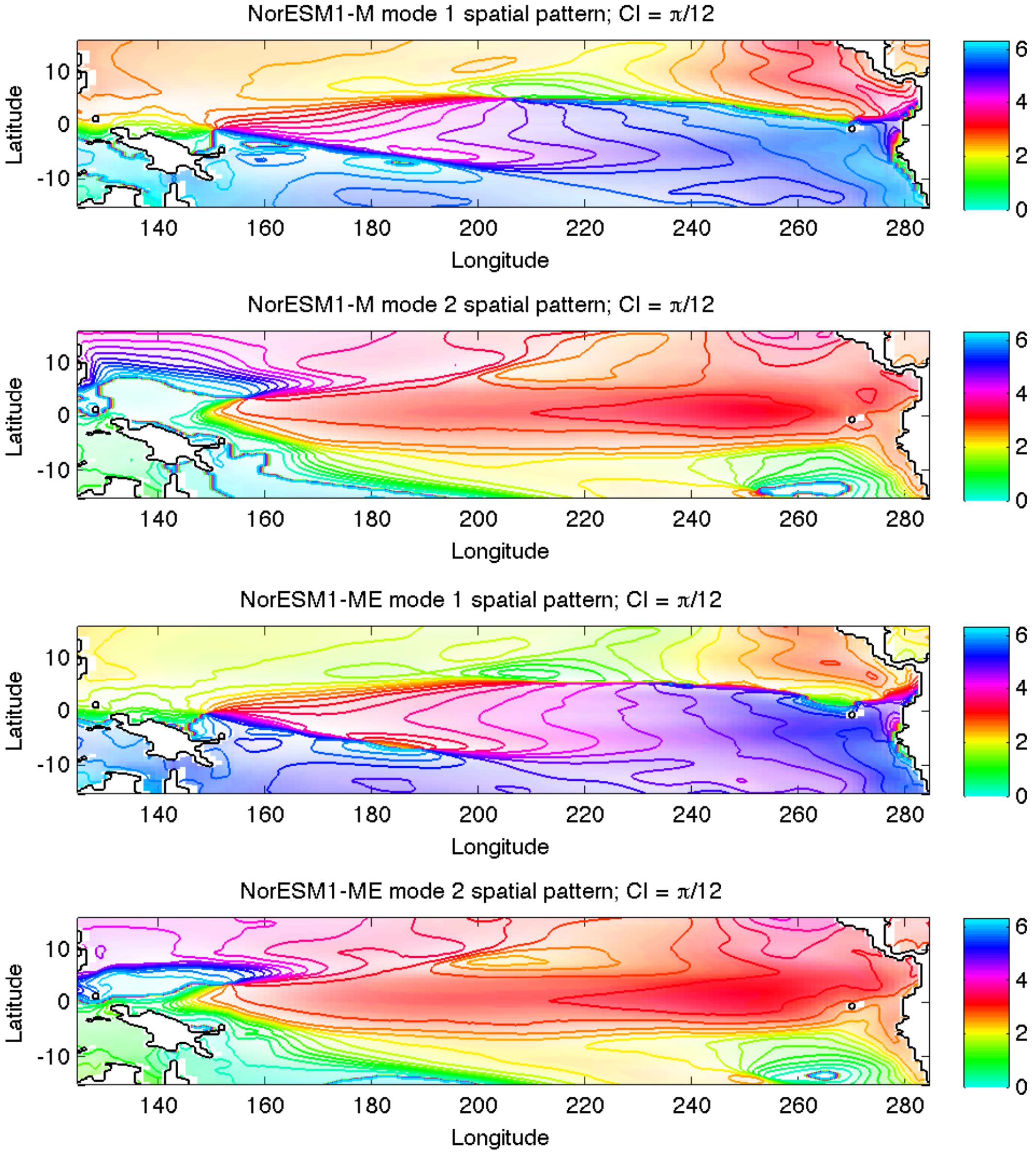

Figure A.15: Contours of the phase spatial pattern (r_n) of the first mode (annual cycle, top) and second mode (ENSO, bottom) of the CEOF decomposition of equatorial SST output from a historical run (1901-2000) of two configurations of the Norwegian Earth System Model. The shading indicates the value of the amplitude spatial pattern (q_n), where darker shading indicates larger amplitude.

Bibliography

An, S. and F. Jin, 2004: "Nonlinearity and asymmetry of ENSO". *Journal of Climate*, **17**, 2399–2412.

An, S. and F. Jin, 2011: "Linear solutions for the frequency and amplitude modulation of ENSO by the annual cycle". *Tellus A*, **63A**, 238–243.

Arnold, V. I., M. Levi, and J. Szucs, 1983: *"Geometrical methods in the theory of ordinary differential equations"*. Springer-Verlag.

Balmaseda, M., A. Vidard, and D. Anderson, 2008: "The ECMWF Ocean Analysis System: ORA-S3". *Monthly Weather Review*, **136 (4)**, 3018–3034.

Balmaseda, M. A., M. K. Davey, and D. L. Anderson, 1995: "Decadal and seasonal dependence of ENSO prediction skill". *Journal of Climate*, **8 (11)**, 2705–2715.

Barnett, T. P., 1983: "Interaction of the Monsoon and Pacific Trade Wind System at Interannual Time Scales Part I: The Equatorial Zone". *Monthly Weather Review*, **111 (4)**, 756–773.

Burgers, G. and D. Stephenson, 1999: "The Normality of El Niño". *Geophysical Research Letters*, **26 (8)**, 1027–1030.

Chang, P., B. Wang, T. Li, and L. Ji, 1994: "Interactions between the seasonal cycle and the southern oscillation - frequency entrainment and chaos in a coupled ocean-atmosphere model". *Geophysical Research Letters*, **21 (25)**, 2817–2820.

Gabor, D., 1946: “Theory of Information”. *J. IEEE*, **93**, 429–457.

Galanti, E., E. Tziperman, M. Harrison, A. Rosati, R. Giering, and Z. Sirkes, 2002: “The Equatorial Thermocline Outcropping – A Seasonal Control on the Tropical Pacic Ocean – Atmosphere Instability Strength”. *Journal of Climate*, **15**, 2721–2739.

Harrison, D. and G. Vecchi, 1999: “On the termination of El Niño”. *Geophysical Research Letters*, **26**, 1593–1596.

Hasselmann, K., 1976: “Stochastic Climate Models”. *Tellus*, **28**, 474–485.

Hendon, H. H., M. C. Wheeler, and C. Zhang, 2007: “Seasonal dependence of the MJO-ENSO relationship”. *Journal of Climate*, **20**, 531–543.

Hirst, A., 1986: “Unstable and Damped Equatorial Modes in Simple Coupled Ocean-Atmosphere Models”. *Journal of the Atmospheric Sciences*, **34**, 606–632.

Horel, J., 1982: “The Annual Cycle in the Tropical Pacic Atmosphere and Ocean”. *Monthly Weather Review*, **110**, 1863–1878.

Jin, F., 1997: “An Equatorial Ocean Recharge Paradigm for ENSO. Part I: Conceptual Model”. *Journal of the Atmospheric Sciences*, **54**, 811–829.

Jin, F., S. Kim, and L. Bejarano, 2006: “A coupled-stability index for ENSO”. *Geophysical Research Letters*, **33**, L23 708.

Jin, F., L. Lin, A. Timmmerman, and J. Zhao, 2007: “Ensemble-mean dynamics of the ENSO recharge oscillator under state-dependent stochastic forcing”. *Geophysical Research Letters*, **34 (3)**.

Jin, F., J. Neelin, and M. Ghil, 1994: “El Niño on the Devil’s Staircase: Annual Subharmonic Steps to Chaos”. *Science*, **264**, 70–72.

Jin, F., J. Neelin, and M. Ghil, 1996: “El Niño/Southern Oscillation and the annual cycle: subharmonic frequency locking and aperiodicity”. *Physica D*, **98**, 442–465.

Johnson, S., D. Battisti, and E. Sarachik, 2000: "Empirically Derived Markov Models and Prediction of Tropical Pacific Sea Surface Temperature Anomalies". *Journal of Climate*, **34**, 3–17.

Kallummal, R. and B. Kirtman, 2008: "Validity of a Linear Stochastic View of ENSO in an ACGCM". *Journal of the Atmospheric Sciences*, **65**, 3860–3879.

Kessler, W., 2002: "Is ENSO a cycle or a series of events?". *Geophysical Research Letters*, **29 (23)**, 2125.

Kessler, W. and R. Kleeman, 2000: "Rectification of the Madden-Julian Oscillation into the ENSO cycle". *Journal of Climate*, **13**, 3560–3575.

Kessler, W., M. McPhaden, and K. Weickmann, 1995: "Forcing of the intraseasonal Kelvin waves in the equatorial Pacific". *Journal of Geophysical Research*, **100**, 10,613–10,631.

Kralemann, B., L. Cimponeriu, M. Rosenblum, A. Pikovsky, and R. Mrowka, 2008: "Phase dynamics of coupled oscillators reconstructed from data". *Physical Review E*, **77**, 066 205.

Larkin, N. K. and D. E. Harrison, 2002: "ENSO warm (El Niño) and cold (La Ni na) event life cycles: Ocean surface anomaly pat- terns, their symmetries, asymmetries, and implications". *Journal of Climate*, **15**, 1118–1140.

Lengaigne, M., J. P. Boulanger, C. Menkes, and H. Spencer, 2006: "Influence of the seasonal cycle on the termination of El Niño events in a coupled general circulation model". *Journal of Climate*, **19**, 1850–1868.

Levine, A. F. and F. F. Jin, 2010: "Noise-Induced Instability in the ENSO Recharge Oscillator". **67**, 529–542.

Liu, Z., 2001: "A Simple Model Study of ENSO Suppression by External Periodic Forcing". *Journal of Climate*, **15**, 1088–1098.

Masumoto, Y., et al., 2004: “A Fifty-Year Eddy-Resolving Simulation of the World Ocean Preliminary Outcomes of OFES (OGCM for the Earth Simulator)”. *Journal of the Earth Simulator*, **1**.

McGregor, S., A. Timmermann, N. Schneider, M. Stuecker, and M. England, 2012: “The Effect of the South Pacific Convergence Zone on the Termination of El Niño Events and the Meridional Asymmetry of ENSO”. *Journal of Climate*, **25**, 5566–5586.

McPhaden, M. J., S. E. Zebiak, and M. H. Glantz, 2006: “ENSO as an Integrating Concept in Earth Science”. *Science*, **314 (5806)**, 1740–1745.

Mettin, R., U. Parlitz, and W. Lauterborn, 1993: “Bifurcation structure of the driven van der Pol oscillator”. *International Journal of Bifurcation and Chaos*, **3**, 1529–1555.

Neelin, J., D. Battisti, A. Hirst, F. Jin, Y. Wakata, T. Yamagata, and S. Zebiak, 1998: “ENSO theory”. *Journal of Geophysical Research*, **103**, 14,261–14,290.

Neelin, J. and F. F. Jin, 1993a: “Modes of interannual tropical ocean-atmosphere interaction-a unified view. Part I: Numerical results”. **50**, 3477–3503.

Neelin, J. and F. F. Jin, 1993b: “Modes of interannual tropical ocean-atmosphere interaction-a unified view. Part III: Analytical results in fully coupled cases”. **50**, 3523–3540.

Pan, A., Q. Liu, and Z. Liu, 2005: “Periodic Forcing and ENSO Suppression in the Cane - Zebiak Model”. *Journal of Oceanography*, **61**, 109–113.

Pasmanter, R. and A. Timmermann, 2003: “Cyclic Markov Chains with an Application to an Intermediate ENSO Model”. *Nonlinear Processes in Geophysics*, **10**, 197–210.

Penland, C. and P. Sardeshmukh, 1995: “The Optimal Growth of Tropical Sea Surface Temperature Anomalies”. *Journal of Climate*, **8**, 1999–2024.

Philander, S., 1983: “El Niño Southern Oscillation phenomena”. *Nature*, **302**, 295–301.

Philander, S., T. Yamagata, and R. Pacanowski, 1984: “Unstable Air-Sea Interactions in the Tropics”. *Journal of the Atmospheric Sciences*, **41**, 604–613.

Pikovksy, A., M. Rosenblum, and J. Kurths, 2000: “Phase Synchronization in Regular and Chaotic Systems”. *International Journal of Bifurcation and Chaos*, **10**, 2291–2305.

Preisendorfer, R. W., 1988: *“Principal Component Analysis in Meteorology and Oceanography”*, Developments in Atmospheric Science, Vol. 17. Elsevier Science Publishers B.V.

Rasmusson, E. and T. Carpenter, 1982: “Variations in Tropical Sea Surface Temperature and Surface Wind Fields Associated with the Southern Oscillation/El Niño”. *Monthly Weather Review*, **110**, 354–384.

Rayner, N. A., D. E. Parker, E. B. Horton, C. K. Folland, L. V. Alexander, D. P. Rowell, E. C. Kent, and A. Kaplan, 2003: “Global analyses of sea surface temperature, sea ice, and night marine air temperature since the late nineteenth century”. *Journal of Geophysical Research*, **108**, 4407.

Smith, T., R. Reynolds, T. Peterson, and J. Lawrimore, 2008: “Improvements to NOAAs Historical Merged LandOcean Surface Temperature Analysis (18802006)”. *Journal of Climate*, **21**, 2283–2296.

Stein, K., N. Schneider, and A. Timmermann, 2011: “Phase Synchronization of the El Niño-Southern Oscillation with the Annual Cycle”. *Physical Review Letters*, **107**, 128 501.

Stein, K., N. Schneider, A. Timmermann, and F. Jin, 2010: “Seasonal Synchronization of ENSO Events in a Linear Stochastic Model”. *Journal of Climate*, **23**, 5629–5643.

Stuecker, M. F., A. Timmermann, F.-F. Jin, S. McGregor, and H.-L. Ren, 2013: “A Combination Mode of Annual Cycle and the El Niño-Southern Oscillation”. *Nature Geoscience*, **in press**.

Suarez, M. J. and P. Schopf, 1988: "A delayed action oscillator for ENSO". *Journal of the Atmospheric Sciences*, **45**, 32833287.

Taylor, K. E., R. Stouffer, and G. Meehl, 2012: "An overview of CMIP5 and the experiment design". *Bulletin of the American Meteorological Society*, **93**, 485–498.

Thompson, C. and D. Battisti, 2000: "A Linear Stochastic Dynamical Model of ENSO. Part I: Model Development". *Journal of Climate*, **13**, 2818–2832.

Torrence, C. and P. J. Webster, 1998: "The annual cycle of persistence in the El Niño/Southern Oscillation". *Quarterly Journal of the Royal Meteorological Society*, **124**, 1985–2004.

Trenberth, K. E., G. W. Branstator, D. Karoly, A. Kumar, N. C. Lau, and C. Ropelewski, 1998: "Progress during TOGA in understanding and modeling global teleconnections associated with tropical sea surface temperatures". *Journal of Geophysical Research*, **103**, 14 291–14 324.

Tziperman, E., E. Stone, M. Cane, and H. Jarosh, 1994: "El Niño chaos: overlapping of resonances between the seasonal cycle and the Pacific ocean-atmosphere oscillator". *Science*, **264**, 72–74.

Tziperman, E., S. Zebiak, and M. Cane, 1995: "Irregularity and Locking to the Seasonal Cycle in an ENSO Prediction Model as Explained by the Quasi-Periodicity Route to Chaos". *Journal of the Atmospheric Sciences*, **52**, 293–306.

Tziperman, E., S. Zebiak, and M. Cane, 1997: "Mechanisms of Seasonal - ENSO Interaction". *Journal of the Atmospheric Sciences*, **54**, 61–71.

van der Pol, B., 1927: "Forced oscillations in a circuit with non-linear resistance (reception with reactive triode)". *The London, Edingburg and Dublin Philosophical Magazine*, **3 (65–80)**.

Wang, B. and Z. Fang, 1996: "Chaotic Oscillations of Tropical Climate: A Dynamic System Theory for ENSO". **53**, 2786–2802.

Wang, B., R. Wu, R. Lukas, and S. An, 1999: “A possible mechanism for ENSO turnabouts”. *Journal of Climate*, **11**, 2191–2199.

Xie, S., 1994: “On the genesis of the equatorial annual cycle”. *Journal of Climate*, **7**, 2008–2013.

Xue, Y., M. Cane, and S. Zebiak, 1997: “Predictability of a Coupled Model of ENSO Using Singular Vector Analysis. Part I: Optimal Growth in Seasonal Background and ENSO Cycles”. *Monthly Weather Review*, **125**, 2043–2056.

Yan, B. and R. Wu, 2007: “Relative roles of different components of the basic state in the phase locking of El Niño mature phases”. *Journal of Climate*, **20**, 4267–4277.

Zebiak, S. and M. Cane, 1987: “A model ENSO”. *Monthly Weather Review*, **115**, 2262–2278.